

© Copyright by Zhuo Chen 2012
All Rights Reserved

**Plasma Enhanced Layer-by-layer Deposition and Nano-crystallization
of Si:H films**

A Dissertation

Presented to the Faculty of

Department of Chemical & Biomolecular Engineering

University of Houston

In Partial Fulfillment

of the Requirements for the Degree

Doctor of Philosophy

in

Chemical Engineering

by

Zhuo (Carol) Chen

December 2012

**Plasma Enhanced Layer-by-layer Deposition and Nano-crystallization
of Si:H films**

Zhuo (Carol) Chen

Approved:

Co-Chair of the Committee
Dr. Vincent M. Donnelly, Professor,
Chemical & Biomolecular Engineering

Co-Chair of the Committee
Dr. Demetre J. Economou, Professor,
Chemical & Biomolecular Engineering

Committee Members:

Dr. Gila Stein, Assistant Professor,
Chemical & Biomolecular Engineering

Dr. Shin-Shem Steven Pei, Professor,
Electrical and Computer Engineering

Dr. Paul Ruchhoeft, Associate Professor,
Electrical and Computer Engineering

Dr. Suresh K. Khator, Associate Dean,
Cullen College of Engineering

Dr. Ramanan Krishnamoorti, Professor,
Department Chairman,
Chemical & Biomolecular Engineering

Dedicated to my husband Lei Wang

and our parents

Qingzhen Yang, Zhenshu Chen

Jinxian Bian, Changgui Wang

Acknowledgements

First of all, I am so grateful that I have Prof. Vincent M. Donnelly and Prof. Demetre J. Economou as my Ph.D. research advisors. Both have amazing experience and vision, as well as personality. Their passion and attitude towards science and engineering have been inspiring me ever since the beginning of my research. The experience of working with them not only equipped me with solid background knowledge in plasma processing, but also gave me promising directions for future work.

It is my great honor to have Prof. Gila Stein, Prof. Shin-Shem (Steven) Pei and Prof. Paul Ruchhoeft as committee members of my Ph.D. dissertation. I appreciate all their time and effort spent on my dissertation and defense.

I would like to thank the University of Houston GEAR program, the National Science Foundation, and the Department of Energy for funding this project. I would also like to express my deep thanks to Dr. Hong Shih and Dr. Lin Xu from Lam Research Corp. for support with TEM measurements.

I am so thankful to Prof. Yi-kang Pu of Tsinghua University, who introduced me to the terrific world of plasma and the semiconductor industry. I was positively influenced by his scientific logic and critical thinking during his visit of our laboratory.

I would like to express my sincere appreciation to Dr. Jay A. Mucha. Without his dedicated help in film characterization with spectroscopic ellipsometry, this research would not have been as deep and interesting. I would also like to convey my deep thanks to Dr. Milko N. Iliev, who provided great support with Raman spectroscopy.

I'm grateful to the excellent machinist, Mr. John Costales, who did a great job in helping me with my experimental hardware. Without his talent and valuable suggestions, I would not have been able to achieve our goals. I would also like to thank the staff of the Department of Chemical and Biomolecular Engineering for their kind assistance.

I would like to thank my previous colleagues in industry, Dr. Jian Ding and Dr. Ito Masao for their great support. Without their encouragement, I might not have had the determination as well as the opportunity to work on my Ph.D. in the United States. At the same time, my sincere appreciation goes to my colleagues during my summer 2011 internship at Lam Research, Dr. Joydeep Guha, Dr. Butsurin Jinan, Dr. Lin Xu and Dr. Sang Ki Nam. It was great fun to work with all of them, and it was truly one of the most unforgettable periods of my life.

It has been a fantastic experience to have the following former and current group members in our lab: Dr. Zhiying Chen, Dr. Sergey Belostotskiy, Dr. Sung Jung Kang, David Kelly, Dr. Rohit Khare, Dr. Hyungjoo Shin, Dr. Paola Diomedea, Weiye Zhu, Yoshio Susa, Ashutosh Srivastava, Dr. Erdinc Karakas, Dr. Se Youn Moon, Siyuan Tian, Lei Liu, and Shyam Sridhar. All of your kind help is highly appreciated. Special thanks go to Dr. Zhiying Chen and Dr. Paola Diomedea who have given me a lot of encouragement to overcome difficulties. We have spent a lot of wonderful time together in both life and work. Again, thank you all very much for making the lab warm and sweet.

Last but not least, I would like to express my deepest appreciation to my husband Lei Wang and our parents. I am so blessed to have all of you with me every step of the way, giving me incredible courage and strength to continue my journey in life.

**Plasma Enhanced Layer-by-layer Deposition and Nano-crystallization
of Si:H films**

An Abstract

of a

Dissertation

Presented to the Faculty of

Department of Chemical & Biomolecular Engineering

University of Houston

In Partial Fulfillment

of the Requirements for the Degree

Doctor of Philosophy

in

Chemical Engineering

by

Zhuo (Carol) Chen

December 2012

Abstract

Nano-crystalline Si (nc-Si) is a promising candidate for photovoltaic applications due to its better stability compared to amorphous Si, and relatively easy to manufacture at low cost, by plasma enhanced chemical vapor deposition (PECVD), compared to single crystal Si. The crystalline volume fraction of nc-Si films needs to be well controlled to prevent light-induced degradation of the otherwise amorphous hydrogenated Si (a-Si:H).

A layer-by-layer technique using two separate plasma sources for a-Si:H deposition and nano-crystallization was developed. A capacitively-coupled plasma (CCP) with SiH₄/He feed gas was used to deposit thin a-Si:H layers that were subsequently exposed to a H₂ or D₂ inductively-coupled plasma (ICP) to induce crystallization in the films. Deposition and nano-crystallization were performed sequentially and periodically to grow thin films. Raman spectroscopy was used to characterize the films and determine the fraction of crystalline. The crystalline volume fraction obtained in this work ranged from 0% to 72%. Many short exposures (20 s or 5 s) to the plasmas were more effective in producing nano-crystalline Si compared to one long exposure (40 min. or 4 min.). In addition, the fraction of nano-crystalline Si increased with increasing H₂ ICP-to-SiH₄/He CCP exposure time ratio (from 1/4 to 3/2). The crystallites had columnar structure along the film growth direction based on transmission electron microscopy (TEM).

Etching of films by the D₂ plasma was monitored by mass spectrometry. At 250 °C, the amorphous Si etching rate (0.25 nm/min) was much lower than the deposition rate (1.4 nm/min), and that etching did not occur exclusively on the surface or the near surface region. The blueshift (by about 1 eV) of the dielectric constants peak, found by

spectroscopic ellipsometry (SE), suggested the formation of nano-crystallites in the bulk of the films.

It is proposed that by tailoring the CCP deposition time as well as the H₂ ICP exposure time per cycle, the crystalline fraction and crystallite size of the resulting films can be controlled for more stable solar cell materials. Further, by spatially separating film deposition and nano-crystallization, each of these processes can be individually optimized, providing flexibility in controlling film nanostructure and properties.

Table of Contents

Acknowledgements.....	vi
Abstract.....	ix
Table of Contents.....	xi
List of Figures.....	xiv
List of Tables.....	xxii
Chapter 1. Introduction.....	1
1.1. Introduction to Solar Cell Development.....	1
1.2. nc-Si:H Manufacturing Methods and Characterization.....	3
1.3. Objective of This Research.....	6
1.4. Organization of This Dissertation.....	7
Chapter 2. Literature Review.....	9
2.1. Nature of a-Si:H.....	9
2.2. Methods for a-Si:H Deposition.....	12
2.2.1. PECVD of a-Si:H.....	12
2.2.2. VHF and MW PECVD of a-Si:H.....	15
2.2.3. HW CVD of a-Si:H.....	18
2.3. Light-induced Degradation of a-Si:H.....	20
2.4. Nature and Benefits of nc-Si:H.....	24
2.5. Models of the Kinetics of nc-Si:H Growth.....	30

2.6. Film Characterization.....	32
2.6.1. Raman Scattering Spectroscopy	32
2.6.2. Transmission Electron Microscopy	40
2.6.3. Infrared Absorption Analysis	43
2.6.4. Spectroscopic Ellipsometry	45
2.7. Spatially Separated Deposition	49
Chapter 3. Experimental Apparatus	52
3.1. Capacitively Coupled Plasma (CCP) Reactor Design.....	53
3.2. Inductively Coupled Plasma (ICP) Reactor Design.....	57
3.3. Heaters and Susceptor	59
3.4. Ar Curtain.....	64
3.5. Mass Spectrometer Setup.....	65
3.6. Optical Emission Spectroscopy (OES)	66
Chapter 4. Raman Spectroscopy of Layer-by-Layer Processed Films	68
4.1. Layer-by-Layer Cyclic Process Design.....	68
4.2. Raman Spectroscopy Results	71
Chapter 5. Infrared Absorption of Layer-by-Layer Processed Films	86
5.1. IR Analysis of Films after Hydrogen nano-crystallization	86
5.2. IR Analysis of Films after Deuterium Exposure	89

Chapter 6. Mass Spectrometry during ICP Exposure	93
Chapter 7. Spectroscopic Ellipsometry (SE) of Layer-by-Layer Processed Films.....	106
7.1. SE Model and Procedures	106
7.2. SE Analysis Results	113
Chapter 8. TEM Characterization of Layer-by-Layer Processed Films	130
Chapter 9. Conclusions and Recommendations for Future Work	139
9.1. Conclusions	139
9.2. Recommendations for Future Work.....	142
References.....	144
Appendices.....	160

List of Figures

Figure 1.1 First silicon solar cell using p-n junctions formed by impurity segregation in high purity silicon melts, and with flat contact [6].	1
Figure 2.1 Schematic of atom pair distribution function for crystalline solid, amorphous solid and gas. R is the pair separation distance, and R_{av} is the average separation of the nearest neighbor atoms.	10
Figure 2.2 The optical absorption coefficient as a function of incident light wavelength for a-Si:H (dashed curve) and crystalline silicon (solid line) [11].	11
Figure 2.3 a-Si:H film deposition rate as a function of RF frequency at constant power [8].	16
Figure 2.4 X-ray diffraction intensity with normalized magnetic field (NMF) at three scattering angles of crystallite orientation [47]. In this study a microwave plasma system was equipped with a DC magnetic field B along the longitudinal axis of the waveguide. By decreasing B, a transition from amorphous Si to nc-Si:H occurred.	18
Figure 2.5 The conversion efficiency of a-Si:H-based solar cell modules after the first couple of thousand hours of illumination drops by 30% of its initial efficiency for single-junction cells, and by 15% for triple-junction cells. The dashed line shows the initial power output for each module [8].	20
Figure 2.6 Decrease of conductivity and dark conductivity for undoped a-Si:H films (a), and PH ₃ doped a-Si:H films (b), during 200 mW/cm ² illumination. The starting thermal equilibrium state is marked as A. Solid curves shows conductivity and dashed curves show dark conductivity [56].	21
Figure 2.7 Comparison of the optical absorption coefficient of μ c-Si, a-Si, c-Si, and calculated μ c-Si comprised of 10% a-Si and 90% c-Si [12].	24
Figure 2.8 Dark conductivity change with time at 30°C, with the accelerated light-soaking tests at 80°C and 350 mW/cm ² filtered light. pm-Si has an intermediate ordered structure between amorphous and μ c-Si. Two pm-Si films are deposited at different pressure. Four μ c-Si films have different crystalline fractions of 67%, 31%, 79% and 96% from top to bottom on the right side of the insert label [66].	25
Figure 2.9 The defect-related absorption coefficient at 0.8 eV in the initial state and after 1000 h of light-soaking as a function of crystalline volume fraction for nc-Si:H single junction solar cells [15].	27

Figure 2.10 Schematic of an amorphous phase surrounded by crystalline phases forming two back-to-back diodes [17].....	29
Figure 2.11 Comparison of the Raman spectrum for sample #76 with different excitation laser sources.....	33
Figure 2.12 Integrated intensity ratio between 517 cm^{-1} peak and peak around 509 cm^{-1} as a function of crystallite size [81].....	37
Figure 2.13 Plot of Raman peak frequency against crystallite size, which is measured by x-ray diffraction. (a) peak location (near to 520 cm^{-1}) with crystallite size for unannealed (open circles) and annealed (filled circles) samples of $\mu\text{c-Si:H}$; the other dotted curves and solid curve are from simulation results; (b) peak location (near to 480 cm^{-1}) as a function of crystallite size [89].	38
Figure 2.14 Plot of the crystalline peak location as a function of crystallite size; Δ is the experimental results and the dashed curve is from the model [78].....	40
Figure 2.15 (a) Diffraction patterns from cross-sectional TEM samples. The Raman spectra for samples a to e are shown in (b). The samples are deposited with different silane concentrations in hydrogen (from 2% to 6.2% silane by volume) [70].	41
Figure 2.16 Cross-sectional dark-field TEM images of nc-Si:H, (a) strong columnar growth under the high hydrogen dilution deposition condition, 2% silane in H_2 , (b) 4% silane in H_2 , (c) 5.7% silane in H_2 , (d) 5.9% silane in H_2 . The bright regions correspond to the crystalline grains with the same orientation according to the incident electron beam [70].....	42
Figure 2.17 High resolution TEM image of the cross-sectional sample with high crystalline volume fraction. The arrow points out a narrow grain boundary [70].....	43
Figure 2.18 (a) five different layers for the nc-Si:H film, including the surface layer with silicon dioxide and voids used to represent the roughness, interface layer consisting of c-Si, a-Si and silicon dioxide, the main film layer including c-Si, a-Si and voids, the interface between the deposited film and substrate and the silicon substrate layer. (b) Based on the model in (a) good fitting of $\tan \Psi$ and $\cos \Delta$ is obtained between the measured data (solid curves) and the calculated data (dashed curves) [96].	47
Figure 2.19 Real ϵ_1 and imaginary ϵ_2 dielectric function for crystal Si (marked as c Si), polycrystalline silicon doped with As (p Si:As), undoped nc-Si (p Si:ud) and amorphous silicon (a Si) as a function of incident light energy and the optical absorption coefficient for these four silicon film structures [97].	48
Figure 2.20 (a) Schematic of two plasma sources (#13a and 13b) enclosed in a single vacuum chamber (#10) with rotating substrates (#14). (b) Top view for the wafer holder with six substrates [105].	50

Figure 2.21 Schematic of spatial ALD with gas channels arranged sequentially, and the substrate moving with constant speed underneath the gas channels [103].	50
Figure 3.1 Schematic of the dual plasma source with rotating susceptor.	52
Figure 3.2 Schematic of the CCP source	53
Figure 3.3 Top view of the ceramic plate with holes for gas line, RF feed line, two water lines and supports.	54
Figure 3.4 Schematic for CCP π -type matching network.	55
Figure 3.5 Schematic of the showerhead RF powered electrode. (a) Top view of the showerhead, and (b) Side view of the showerhead. The width and height of the hollow space behind the holes were designed to make gas flowthrough the showerhead uniform.	55
Figure 3.6 Magnetic multi-pole confinement of the plasma.	56
Figure 3.7 (a) Strong parasitic plasma behind the showerhead in-between metal parts. (b) Uniform plasma could be obtained under pressure of 400~1600 mTorr and input power of 5~30 W.	57
Figure 3.8 Schematic of the ICP reactor.	58
Figure 3.9 Schematic of gas inlet.	59
Figure 3.10 Top view of the heater covers and the top flange.	60
Figure 3.11 Schematic of a heater.	61
Figure 3.12 Top view of the susceptor and design of the edge of the well where the substrate rests.	62
Figure 3.13 Stepping motor control interface.	63
Figure 3.14 The schematic of the Ar curtain (a) top view and (b) side view.	64
Figure 3.15 Schematic of the mass spectrometer setup.	66
Figure 3.16 Schematic for OES set up to monitor ICP source.	67
Figure 3.17 Main components of intensified charge coupled device (ICCD).	67
Figure 4.1 Raman spectrum of a glass cover slip substrate.	69

Figure 4.2 Raman spectrum of sample s55 subjected only to CCP a-Si:H deposition. The spectrum was deconvoluted into one Gaussian peak at 479 cm^{-1} with 69 cm^{-1} FWHM. The Raman spectrum from single crystalline Si is also shown for reference (peak at 520 cm^{-1} with 7 cm^{-1} FWHM). 71

Figure 4.3 Raman spectrum of sample s69 subjected to 40 min. CCP a-Si:H deposition and then 60 min. ICP nano-crystallization (one cycle). The spectrum was deconvoluted into three Gaussian peaks at 480 cm^{-1} (64 cm^{-1} FWHM), 503 cm^{-1} (42 cm^{-1} FWHM) and 520 cm^{-1} (10 cm^{-1} FWHM). 72

Figure 4.4 Raman spectra of films deposited at a substrate temperature of 250°C with the same *total* deposition time of 40 min., and variable ratio of deposition time to nano-crystallization time t_1/t_2 , as well as variable number of cycles, $n_c = 1$ in (a), $n_c = 10$ in (b) and $n_c = 120$ in (c). 74

Figure 4.5 Raman spectrum for sample s76, along with the fit (red line) obtained from a Gaussian three-peak deconvolution. 75

Figure 4.6 Crystalline volume fraction as a function of the ratio of H_2 ICP nano-crystallization time to CCP deposition time and number of process cycles, (a) using the three-peak method $\frac{I_{510} + I_{520}}{I_{480} + I_{510} + I_{520}}$, and (b) using the two-peak method $\frac{I_{520}}{I_{480} + I_{510} + I_{520}}$ 77

Figure 4.7 The $\sim 480\text{ cm}^{-1}$ Raman peak position as a function of ICP exposure time and number of cycles. 78

Figure 4.8 Nano-crystallite size with different ICP/CCP process time ratios for 12 samples from s56 to s76. Crystallite size increases with ICP process time and cycle number. With 120 cycles and ICP/CCP process time ratio 1.5 the largest crystallites (6.7 nm) were found in s76. 79

Figure 4.9 Stacked Raman spectra for samples with various ICP/CCP process time ratios, each subjected to 120 cycles. 80

Figure 4.10 Crystalline volume fraction for different CCP deposition times t_1 (0.08 min., 0.3 min., 4 min. and 40 min.) and t_2/t_1 (0, 0.25, 0.5, 0.75, 1, 1.5 and 4). 82

Figure 4.11 Raman spectra of a layer-by-layer processed sample (s95, $t_1:t_2 = 5\text{s}/5\text{s}$, 480 cycles) and a sample (s93) processed by continuous rotation of the susceptor. 83

Figure 4.12 Schematic of the geometry of the substrate and the two heaters. During continuous rotation, the substrate was underneath the heaters for $1080/2 + 720/23600 \times 2 = 50\%$ of the time. 84

Figure 4.13 Raman spectra of sample s76 and s97 in (a) with 120 cycles and $t_1/t_2=20$ s/30 s, the difference of crystalline fraction is within 8%; s69 and s86 in (b) with 1 cycle and $t_1/t_2=40$ min/60 min, the difference of crystalline fraction is within 8.3%; and s55 and s87 in (c) with only CCP deposition, they all show the amorphous-like Raman peak. 85

Figure 5.1 Infrared spectra of films with 40 min. total deposition time, and H₂ ICP process times of 0 s for 1 cycle (condition as for sample s55), 30 min. total for 120 cycles (s73), and 60 min. total for 120 cycles (s76). 86

Figure 5.2 Integrated FTIR intensity of the 2090-2100 cm⁻¹ peak (SiH) divided by the sum of integrated intensities of the 2090-2100 cm⁻¹ and 2000 cm⁻¹ (SiH₂) peaks vs. CCP/ICP exposure time ratio. The crystalline volume fraction in the films, as measured by Raman spectroscopy, is also shown. 87

Figure 5.3 Hydrogen content and % hydrogen concentration as a function of ICP exposure time t_2 . Other conditions were 120 cycles and a total deposition time of 40 min. Hydrogen concentration decreases from 13% to 10.5% with increasing t_2 89

Figure 5.4 Infrared spectra of films deposited in SiH₄ (1% diluted by He) for time t_1 and then exposed to a D₂ ICP for time t_2 . With 1 cycle and $t_1: t_2=4:3$, Si-H bonds were detected, while for 10 cycles and $t_1: t_2=4:3$, the Si-H intensity decreased and the Si-D intensity increased. With longer ICP time ($t_1: t_2=4:6$) the Si-D intensity increased further and the Si-H peak disappeared. 90

Figure 5.5 Infrared spectra of a sample with $t_1 / t_2 = 4:6$ and 10 process cycles of CCP deposition and ICP D₂ exposure. 92

Figure 6.1 (a) Reported cracking patterns of SiH₄ and SiD₄ [109] and (b) measured cracking pattern of SiH₄ in this work. 94

Figure 6.2 MS signal intensity in the range AMU 29 to 34 (after background correction) at the start of ICP exposure of an amorphous silicon film deposited in the CCP source for 4 min. 95

Figure 6.3 MS signal (AMU 29 to 34) decay vs. ICP exposure time. 96

Figure 6.4 Mass spectroscopic signal (AMU 34) variation with D₂ ICP exposure time of films grown in the CCP for different deposition times (and therefore different thicknesses). 97

Figure 6.5 Relation between deposited thickness and MS signal time for different CCP deposition times. 99

Figure 6.6 Etched thickness and etching rate in the D₂ ICP for films with different CCP deposition times. 100

Figure 6.7 MS signal at AMU 34 as a function of time for different ICP powers. All films were deposited under the same CCP conditions, resulting in constant film thickness before exposure to the ICP.....	101
Figure 6.8 Integral of the AMU = 34 signal vs. ICP exposure time for different D ₂ ICP powers.	102
Figure 6.9 MS signal at AMU 34 as a function of ICP exposure time for substrate temperatures of 150 °C and 250 °C. Both films were deposited at 250 °C and were ~56 Å thick.....	103
Figure 6.10 Integral of the AMU 34 peak as a function of D ₂ ICP process time at different substrate temperatures.	104
Figure 7.1 Schematic of the spectroscopic ellipsometer.	106
Figure 7.2 Model with five layers for SE data fitting.	107
Figure 7.3 Dielectric constants ϵ_1 and ϵ_2 of sample s55 obtained by SE fitting, compared to those from the Aspnes material in the Woollam material library.	111
Figure 7.4 MSE for all samples subjected to layer-by-layer processing. x-axis is the sample number, y-axis is MSE. Different patterns correspond to different AOI (red circle AOI=55°; black star AOI=62°; black circle=AOI 65°).	113
Figure 7.5 SE fitting data, including surface roughness layer thickness (a), film thickness (b), and void fraction (c) for samples with the same (40 min) total deposition time, but various H ₂ exposure times and different number of cycles. The sample subjected to continuous rotation is also included. Red and black symbols were measurements from samples at identical conditions processed on different days. Blue symbols in (a) and (b) were measurements from TEM images. The x-axis is the sample number #. The ratios under the symbols are the t_1/t_2 time ratios for each cycle.	115
Figure 7.6 Surface layer thickness (Å) as a function of number of cycles (the outlier sample s75 was excluded). The circles on the right are indicators of the distribution of the samples with the same number of cycles. The different symbols at the same number of cycles were measured under different AOI (55°, 62°, 65°). Different colors indicate different t_1/t_2 time ratios, with the same number of cycles (blue: $t_2=0$; green: $t_1/t_2=1/4$; black: $t_1/t_2=2/4$; purple: $t_1/t_2=3/4$; pink: $t_1/t_2=6/4$). The horizontal line of the green diamond for each group shows the mean value of the group (groups have the same number of cycles). The vertical span of the diamonds shows the 95% confidence interval of the mean value.	116
Figure 7.7 (a) Film thickness distribution with various t_1/t_2 as a function of number of cycles. (b) Range of film thicknesses as a function of number of cycles.	117

Figure 7.8 Void fraction as a function of number of cycles (left) and t_2/t_1 (right) for the layer-by-layer processed samples subjected to only CCP deposition, 1 cycle, 10 cycles and 120 cycles. The circles on the right are indicators of the distribution of the symbols under the same number of cycles. The different kinds of symbols at the same number of cycles were measured under different AOI (55° , 62° , 65°). Different colors correspond to different t_1/t_2 time ratios, under the same number of cycles (blue: $t_2=0$; green: $t_1/t_2=1/4$; black: $t_1/t_2=2/4$; purple: $t_1/t_2=3/4$; pink: $t_1/t_2=6/4$). The horizontal line of the green diamond for each group shows the mean value of the group (groups have the same number of cycles). The vertical span of the diamonds shows the 95% confidence interval of the mean value. 119

Figure 7.9 Crystalline fraction from SE analysis as a function of the number of cycles for the layer-by-layer processed samples subjected to only CCP deposition, 1 cycle, 10 cycles and 120 cycles. The circles on the right are indicators of the distribution of the symbols under the same number of cycles. The different symbols at the same number of cycles were measured under different AOI (55° , 62° , 65°). Different colors indicates different t_1/t_2 time ratios, under the same number of cycles (blue: $t_2=0$; green: $t_1/t_2=1/4$; black: $t_1/t_2=2/4$; purple: $t_1/t_2=3/4$; pink: $t_1/t_2=6/4$). The horizontal line of the green diamond for each group shows the mean value of the group (groups have the same number of cycles). The vertical span of the diamonds shows the 95% confidence interval of the mean value. 120

Figure 7.10 Crystalline silicon fraction from SE analysis as a function of t_1/t_2 . Black, red and blue symbols correspond to samples subjected to 1, 10 and 120 cycles, respectively. 121

Figure 7.11 Distribution of Cody-Lorentz oscillator bandgap energy E_g for all the layer-by-layer processed samples. The right side of the figure showed the statistics information for the distribution, i.e. the mean value of E_g and upper/lower 95% mean shown by the diamond, median value of E_g and upper/lower quartile of median shown by the box... 122

Figure 7.12 Dielectric constants ϵ_1 and ϵ_2 as a function of photon energy for crystalline silicon (black solid curve), Aspnes amorphous silicon (red solid curve), a-Si:H deposited with SiH_4 diluted in He (blue dashed curve) and sample s55 deposited with SiH_4 diluted in He and H_2 (purple dashed curve). 123

Figure 7.13 Dielectric constant ϵ_2 of layer-by-layer processed samples with various CCP deposition to H_2 ICP exposure time ratios. (a) samples subjected to 1 cycle, (b) 10 cycles, (c) 120 cycles and (d) 480 cycles. 124

Figure 7.14 Simulated ϵ_2 from EMA layer as a function of photon energy with various crystalline silicon volume fractions. 125

Figure 7.15 ϵ_2 of EMA layer for samples s55, s69 and s76. 126

Figure 7.16 Simulated ϵ_2 of EMA layer with various void fractions. 127

Figure 7.17 Absorption coefficient of the samples with zero crystalline volume fraction (a-Si:H and s55) and high nano-crystalline volume fraction (s76 and s95) compared to that of a-Si from the Aspnes material and c-Si in the Woollam material library.	128
Figure 8.1 Cross sectional dark-field TEM images of sample s58 at 100 nm resolution (a) and 50 nm resolution (b).	131
Figure 8.2 Cross sectional TEM dark field images of sample s55 (40 min. CCP deposition only) and sample s74_2 (120 cycles, $t_1/t_2=5$ s/20 s) at 100 nm resolution....	132
Figure 8.3 The example for the selection of the crystallites under 100 nm resolution of dark-field image (s74_2), the red circles were the regions of crystallites and red lines were used to separate the image into five equal regions.....	133
Figure 8.4 Crystalline volume fraction and average crystallite size from Raman spectra and TEM.	134
Figure 8.5 Cross sectional TEM bright-field images of samples with different X_c calculated by the three-peak method (two-peak method) from Raman spectra. In each image, the Au-Pd coating and SiO ₂ substrate are shown.....	135
Figure 8.6 High resolution cross sectional TEM bright-field images of different samples. Crystalline regions in samples s58, s73 and s74_2 are enclosed by red rectangles.....	137

List of Tables

Table 2.1 Si-H bonds type and vibration frequency.....	44
Table 3.1 Temperature calibration for Si and SiO ₂ substrates.	62
Table 4.1 CCP and ICP operating conditions.	68
Table 4.2 The 19 conditions with various CCP and ICP process times and cycle numbers used in the layer-by-layer cyclic process.	70
Table 5.1 Infrared peak assignment for SiH _x D _y (x=0, 1, 2, 3, y=0, 1, 2, 3, 4) on the surface and in the bulk of the film.	91
Table 6.1 CCP and ICP process conditions for the experiments in Figure 6.4.....	96
Table 7.1 Surface layer thickness, thickness of EMA layer, void fraction, crystalline volume fraction and MSE of sample #76 after each fitting step. The actual curve fits (x-axis is the photon energy (eV) and y-axis is Ψ) are also shown.	110
Table 7.2 Fits for sample s55 at three AOI. The MSE at AOI=55° was the lowest.....	112
Table 8.1 Average width and height of the crystallites, crystalline volume fraction, and the number of regions counted on dark-field TEM images of samples s55, s58 and s74_2.	133

Chapter 1. Introduction

1.1. Introduction to Solar Cell Development

Due to the great potential for harvesting available solar energy, photovoltaics (PV), although studied and utilized for more than thirty years [1, 2], continues to be an area of intense activity. The first functional photovoltaic device was fabricated by Fritts in 1883 with thin-film Se [3]. He incorporated Se into thin films on different metal substrates, such as iron, brass, copper, zinc and tin, and used Au-leaf film on the top as contact. He showed that this Se cell can make a practical working apparatus, providing current that can be stored if it is not used immediately. He predicted the application of the PV technology about one century ago. In 1941, the first semiconductor p-n junction solar cells were fabricated by Russel Ohl at Bell Laboratories [4]. The junction was formed by the solidification of fused silicon, comprising two zones, i.e., a p-type zone and n-type zone as in Figure 1.1. The efficiency of this device was assessed as less than 1% [5].

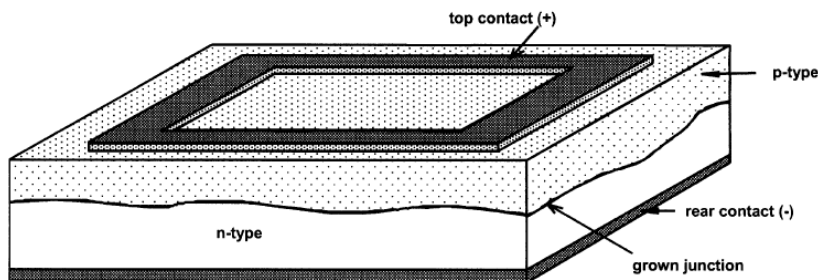


Figure 1.1 First silicon solar cell using p-n junctions formed by impurity segregation in high purity silicon melts, and with flat contact [6].

In 1954, researchers at Bell Laboratories produced Si p-n junction solar cell with 6% efficiency [7]. In part because of the well developed silicon integrated circuit

technology and refinements in substrate manufacturing and processing, the use of silicon for solar cells still predominates. Single crystal Si and poly-crystalline Si with high efficiency reaching 25% dominate the PV industry today [5]. To obtain high efficiency, the solar cells using these materials need to be thick [8]. Because of this, high chemical purity and structural perfection are required to avoid the loss of the electrons and holes that are created in the conduction and valence bands by photon absorption [8]. The manufacturing costs for silicon wafers that meet these requirements are high. To lower the cost, another significant development in solar cells is the application of Si thin films. Due to its lower cost and a wide range of substrate types that can be used, thin film technology has grown dramatically, from 5% of the global PV market share in 2003 to around 20% in 2010 [9]. It is predicted that thin film PV cells will account for 31% of the global PV market in 2013 [10].

In 1976, Carlson and Wronski used a glow discharge with silane gas to deposit hydrogenated amorphous silicon (a-Si:H) thin film and fabricated p-i-n three-layer structures comprised of n-type region, p-type region and intrinsic (undoped) region in-between. The solar conversion efficiency was 2.4% [11]. Since then, due to the low manufacturing cost of a-Si:H compared to crystalline silicon, and its high optical absorption [12], a-Si:H thin films have attracted wide interest. a-Si:H thin films can be deposited at low temperature on various substrates, such as glass, stainless steel and even plastics, using PECVD. These films can even be fabricated on flexible substrates by a “roll-to-roll” technique, whereby the substrates move through the plasma deposition region over rollers [8].

a-Si:H films contain 10% ~ 15% H atoms, which passivate a large fraction of defects resulting from the dangling bonds of Si atoms. This passivation helps decrease the carrier recombination rate, improving device characteristics. However, a-Si:H thin films suffer from stability issues, i.e., after the first few hundred hours of exposure to sunlight, the efficiency of the cell drops (this will be discussed in detail in Chapter 2). This problem can be minimized by inducing micro-crystalline Si ($\mu\text{c-Si}$) or nano-crystalline Si (nc-Si) in the a-Si:H thin film [1, 13-17]. By using a hydrogen-rich deposition process to grow a-Si:H, large quantities of atomic hydrogen arrive at the growing surface, and the deposited films have a fine grain nano-crystalline structure embedded in an amorphous matrix. The grain size in the nc-Si films is around 30-500 Å [18].

1.2. nc-Si:H Manufacturing Methods and Characterization

Matsuda and coworkers used a capacitively coupled plasma (CCP) with H_2/SiH_4 gas to study the growth of microcrystalline silicon under different plasma conditions [19]. They found that as the substrate temperature was increased, the crystalline volume fraction increased, went through a maximum of about 40% at around 400 °C, and then decreased when the temperature reached 500 °C. However, the size of the microcrystallites increased monotonically, while the H content of the films decreased monotonically with temperature. They ascribed the increase of the microcrystalline volume fraction with increasing temperature to thermally-activated surface diffusion of SiH_x adsorbates to stable sites for microcrystalline nuclei formation. At high temperatures, the H surface coverage decreased, and the surface became more reactive. This resulted in stronger binding between SiH_x and adsorption sites, causing the activation energy for surface diffusion to increase and the diffusivity to decrease. This in turn may result in

reduced conversion of amorphous to microcrystalline silicon at higher temperatures. In contract, the crystallite size increased with temperature, even at higher temperatures. They speculated that because of the reduced H-atom surface coverage at higher temperatures, coalescence of the microcrystalline nuclei was enhanced due to the elimination of hindrance by H.

Aydil and coworkers used molecular dynamics simulations [20] and attenuated total reflection Fourier Transform Infrared Spectroscopy (ATR-FTIR) to study the H-atom-induced formation of nc-Si in a-Si:H layers [21-23]. They found that when crystallization happened with dilution of SiH₄ in D₂ plasmas, the surface of the film was mostly covered with mono-hydrides and some tri-hydrides, while in the bulk, nc-Si contained SiH₂, SiH and also SiH₃ [23]. They monitored the IR absorption change of the surface and bulk mono-, di- and tri-hydrides when the a-Si:H film was exposed to a D₂ plasma at different temperatures. With long D₂ plasma exposure at low temperature (60 °C), the IR absorption by SiH₃ and SiH₄ trapped in the bulk increased due to insertion reactions. However, at the surface, an increase in the absorption of SiH₄ and SiH₃ was not found, because SiH₄ desorbed in the gas phase as soon as it was formed and SiH₃ was removed faster by abstraction reactions rather than insertion into Si-SiH₂ bonds. At higher temperature (200 °C), increased IR absorption by SiH₃ and SiH₄ in the bulk film was not observed, since H (D) abstraction was faster than the formation of insertion products. Furthermore, by decoupling the abstraction, insertion and etching processes from the analysis of IR data for different hydrides, they concluded that the abstraction reaction occurred through the Eley-Rideal (ER) mechanism with no activation energy barrier.

Parson and co-workers [24, 25] grew thin layers of a-Si:H in a SiH₄ capacitively coupled plasma (CCP) and then exposed the film to a D₂ plasma by switching gas from SiH₄ to D₂ in the same reactor. The time resolution was limited to 3 s by the gas residence time in the reactor. Using mass spectrometry, they observed that hydrogen was removed from a-Si:H in the D₂ plasma by D-atom abstraction to form HD, and to a lesser extent, through etching reactions that generated silane. After the loss of hydrogen, two adjacent silicon dangling bonds could react with each other to form more stable and strong crystal-like bonds, which enhanced the surface crystallization. The rate of crystallization was found to increase with increasing substrate temperature, but the abstraction rate was always fast and independent of temperature because of the small activation barrier [24]. The authors proposed that crystallization was limited by thermally activated diffusion of silicon on the surface to find favorable sites [14, 25].

Shimizu and co-workers used secondary ion mass spectrometry (SIMS) to evaluate the depth profiles of H or D in films grown with a layer-by-layer technique [26, 27]. They found that chemical annealing played an important role in the structural relaxation of the solid, during the transition from a-Si:H to nc-Si. They pointed out that at 300 °C, the H diffusion depth and chemical etching were important for the structural relaxation, while over 300 °C, as etching became negligibly small, surface H abstraction by H₂ or D₂ was dominant. In addition, by analyzing spectroscopic ellipsometry data, they found increased surface roughness and void fraction with increasing crystalline volume fraction. They inferred that at the initial stage of crystal growth, surface roughness contributed significantly to nucleation and crystalline phase formation [26].

Ves and Kircher confirmed this conclusion by measuring the % void fraction and surface roughness of nc-Si:H films with varying thickness [28].

Asano used two separate PECVD reactors in a vacuum chamber to deposit and crystallize growing films [29,30]. They stated that, at 250 °C, chemical etching was not significant, because the deposited layer thickness increased in proportion to the deposition time from 0 to 40 s, with 6 s or 48 s H₂ exposure time per cycle. SiH₂ increased with increasing H-atom flux. They proposed that in the H₂ plasma, H atoms chemisorb on the surface, decreasing the surface reactivity but increasing the diffusion length of the adsorbed deposition precursors. This led to the reconstruction of a quite dense Si-Si network and the formation of micro-crystalline Si [29].

1.3. Objective of This Research

nc-Si:H is one of the most promising materials for thin film solar cells because of its high optical absorption, high stability and low cost. The distribution of nano-crystallites in the film volume and crystalline volume fraction can influence the optical and electrical properties of the film. Therefore it is important to study the transition from a-Si:H to nc-Si:H. Using one deposition chamber and different gases for a-Si:H deposition followed by nano-crystallization, the gas residence time limits the cycle time. Therefore, it is hard to deposit very thin (down to monolayer) films, crystallize them, and then repeat this process many times to build up a sufficiently thick layer. Furthermore, if a relatively thick a-Si:H film is deposited in every cycle, nano-crystallization may not be uniform throughout the film.

In this research, a-Si:H deposition and crystallization were separated using two plasma sources within one vacuum chamber. Films were grown by PECVD in a SiH₄/He capacitively coupled plasma reactor, and then crystallized in a H₂ inductively coupled plasma, in a cyclic process. The number of growth/crystallization cycles was varied over a wide range, thus allowing one to explore deposition and crystallization of freshly deposited films with thickness ranging from 100s of Å to one monolayer. With thinner a-Si:H films deposited per cycle, more uniform nano-crystallite distribution through the film is expected. The transition from a-Si:H to nc-Si was studied by using these separate plasma sources for a-Si:H deposition and crystallization. Etching occurring in the H₂ plasma was studied by monitoring silane etching products, using mass spectrometry. Raman spectroscopy, spectroscopic ellipsometry, FTIR and TEM were used to characterize the films, and to help understand the transition from a-Si:H to nc-Si.

1.4. Organization of This Dissertation

Chapter 1 gives an introduction to solar cell thin film materials, and a discussion of nc-Si:H deposition. The objective of the research is also introduced.

Chapter 2 discusses the nature of a-Si:H, light-induced degradation of a-Si:H as a solar cell material, and the improvements afforded by introducing nano-crystallites in the a-Si:H film. Further, models of the kinetics of formation of nano-crystallites in these films are introduced, and film characterization methods are discussed.

Chapter 3 describes the experimental apparatus. The plasma reactors and the process monitoring apparatus are shown.

Chapter 4 presents results of nc-Si:H growth by a layer-by-layer cyclic process varying the number of cycles and the ratio of deposition time to nano-crystallization time. The Raman spectra used to determine the microstructure of the films are discussed in this chapter.

Chapter 5 provides IR analysis of films after nano-crystallization. To distinguish H from the film and from the plasma, deuterium (i.e., D₂) was used in ICP in place of H₂.

Chapter 6 presents the results of spectroscopic ellipsometry analysis. Film properties are discussed, including thickness, percentage of voids, surface roughness and the estimated crystalline volume fraction.

Chapter 7 presents the TEM results for film microstructure. The columnar structure of the crystallites growth is shown.

Chapter 8 discusses the etching process monitoring using a mass spectrometer during nano-crystallization. Etching rate was estimated under different substrate temperature.

Chapter 9 gives a summary and conclusions of the research. And some directions of the future research are discussed.

Chapter 2. Literature Review

2.1. Nature of a-Si:H

Hydrogenated amorphous silicon is usually fabricated using a glow discharge plasma with silane gas often diluted with H₂. Because of the large amount of hydrogen in the feed gas, a-Si:H films contain around 10% H, depending on the deposition conditions [31, 32]. Hydrogen atoms join with Si dangling bonds and form Si-H with an inhomogeneous spatial distribution in the film [33]. In the most recent literature, the term “hydrogenated” in front of the amorphous silicon film is omitted. However hydrogenation is quite essential for obtaining the desired optical and electronic properties, by reducing the native dangling bond defect concentration to about 10¹⁵ cm⁻³ [34].

In crystalline silicon, the atoms have near-perfect arrangement, i.e. each silicon atom forms four covalent bonds to neighboring atoms, arranged in tetrahedral configuration, except at defects. In amorphous silicon (without hydrogen), most Si atoms are also bonded to four Si atoms in a tetrahedral configuration, but there is no long-range order. In a-Si:H, some Si atoms are bonded to 3 Si atoms and 1 H atom, and again there is no long range order. This disorder can be described using the atom pair distribution function [34], shown in Figure 2.1.

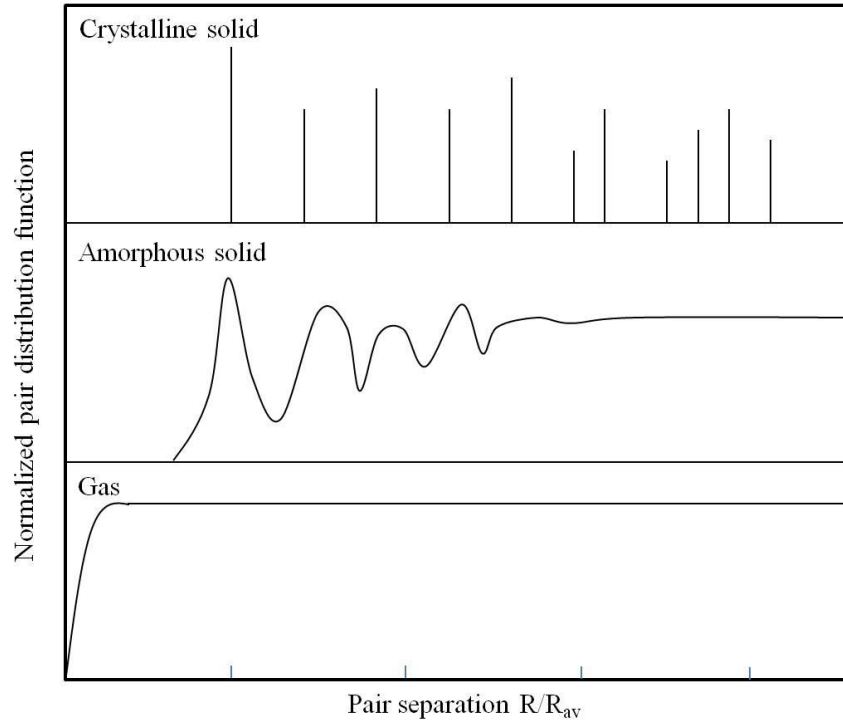


Figure 2.1 Schematic of atom pair distribution function for crystalline solid, amorphous solid and gas. R is the pair separation distance, and R_{av} is the average separation of the nearest neighbor atoms.

The atom pair distribution function is the probability of finding an atom at a distance R . In a gas, atoms are randomly distributed, and thus the distribution function is constant beyond a small distance. For a crystalline solid, due to the nearly perfect order of atom arrangement, the distribution consists of well-defined discrete locations as shown in Figure 2.1; while for the amorphous solid, the distribution function shows structure at short lengths, but after a few atomic distances, the ordered structure is lost. This lack of long range order for a-Si:H can be detected by Raman scattering spectroscopy, where a broad (40 cm^{-1} full width at half maximum, FWHM) peak appears at 480 cm^{-1} . By contrast, crystalline Si shows a sharp peak at 520 cm^{-1} with less than 10 cm^{-1} FWHM [24, 35], as further discussed in section 2.6.1. Though disordered, a-Si:H films have good

optical and electronic properties, and in some cases are even superior to crystalline silicon (e.g., absorption coefficient).

Figure 2.2 shows the light absorption coefficient as a function of wavelength for crystalline silicon and for a-Si:H [11]. The light absorption coefficient of a-Si:H is higher than that of crystalline silicon from 0.315 μm to 0.75 μm [11]. Therefore, the absorption efficiency for a-Si:H is higher than that of c-Si; thus, thinner a-Si:H films can be used. For example, a 500 nm-thick a-Si:H film can absorb 420 W/m^2 of solar radiation, while a crystalline Si film of the same thickness, can absorb only 200 W/m^2 [8].

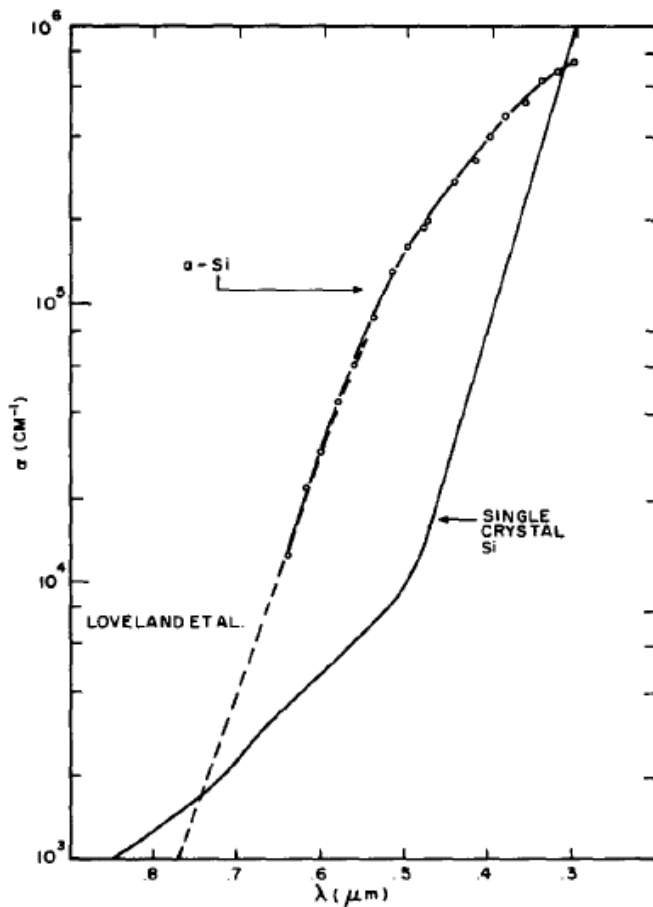


Figure 2.2 The optical absorption coefficient as a function of incident light wavelength for a-Si:H (dashed curve) and crystalline silicon (solid line) [11].

2.2. Methods for a-Si:H Deposition

Methods to grow a-Si:H include silane-based glow discharges, sputtering and thermal chemical vapor deposition CVD [8, 36]. The glow discharge technique, also known as plasma enhanced chemical vapor deposition (PECVD), is the most widely studied for a-Si:H-based device manufacturing. In this section, PECVD and the related methods of very high frequency (VHF) and microwave (MW) PECVD, as well as hot-wire (HW) CVD will be further discussed.

2.2.1. PECVD of a-Si:H

PECVD typically uses pure silane or silane dilution with H₂, Ar or He at pressures of 0.1-10 Torr with DC or 13.56 MHz RF excitation. The substrates are heated to 150-400 °C to optimize the film quality by enhancing the surface diffusion of adatoms during growth [8, 37] as well as their diffusion in the near subsurface region [24]. The substrate material can be silicon, glass, ceramic etc. with large area (e.g., 40 cm × 120 cm) for solar cells [38]. For large area substrates the deposited film uniformity is critical. To achieve uniform flux of ions and deposition precursors (such as SiH₃ and SiH₂), a parallel plate reactor (diode) design is favored [37].

A PECVD system consists of several core components [8].

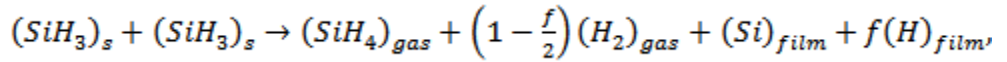
1. A gas delivery system designed to provide uniform gas flow inside the chamber, mass flow controllers to set the required gas flow rate, gas cylinders and regulators.
2. Plasma generation chamber. For capacitively-coupled systems, two parallel plate electrodes are installed with a typical separation gap between 10 to 50

mm. With a smaller gap, the deposited film can be more uniform, while with a larger gap, plasma is easier to maintain [8]. Usually one electrode is grounded and the other one is supplied with RF power between 10 mW/cm^2 to 100 mW/cm^2 . If the RF power is lower than 10 mW/cm^2 , it may be difficult to ignite and sustain the plasma. However, if too much power is used, fast gas-phase reactions result in the formation of silicon polyhydride powder, which could contaminate the film [8]. Such powder formation was also found in the present work, for power densities greater than 360 mW/cm^2 . Powder formation can be minimized or eliminated by using H_2 dilution. Further, to avoid possible contamination on the films by gas phase powders, the heated substrate is placed upside down so that gravity drives particles away from the growing surface. This configuration also suppresses natural convection as well as thermophoretic particle deposition since the gas temperature is highest near the substrate. The chamber base pressure is sufficiently low and the gas flow rates are sufficiently high to reduce incorporation of impurities during growth, which could result in defect formation in the film and decrease the diffusion length of the light-induced carries [36].

3. Pressure regulation and pumping system, which consists of gate valve, turbomolecular pump and the associated roughing pump for low base pressure and pressure control.

The PECVD chamber used in this project for a-Si:H deposition is discussed in detail in Chapter 3. a-Si:H film deposition by PECVD can be broken down in the following steps [38].

1. Many reactions take place in the gas phase, including electron-impact excitation, dissociation and ionization of SiH₄, neutral-neutral reactions, ion-neutral reactions and positive ion-negative ion recombination reactions [39]. Even though ions can play an important role in deposited film properties, prior work shows that most deposition occurs via neutral radical precursors [37, 40].
2. As reactive radicals diffuse through the gas and stick onto the surface of the growing film, surface reactions as well as surface and subsurface diffusion of radicals take place. For example, film growth by SiH₃ precursor can be described by reaction R2.1 [40],



R2.1,

where $(SiH_3)_s$ is an adsorbed species, and $f (\cong 0.1)$ is the fraction of the products.

3. H₂ is released from the surface, and annealing of the silicon matrix also takes place.

The SiH₃ radical is believed to be the major precursor for high-quality a-Si:H film growth [8, 40-42]. Based on the model by McCaughey and Kushner [41], adsorbed SiH₃ radicals diffuse on the surface of the film and can only insert into lattice sites with one dangling bond. SiH₃ has a low sticking coefficient of about 0.09 [43] and a relatively high surface mobility. This helps fill in surface roughness, preventing the formation of large voids, thus resulting in relatively smooth films of high quality. In contrast, adsorbed SiH₂ radicals can insert either at active (dangling bond) or passive (with all four bonds

satisfied) sites, and thus have a rather high sticking coefficient of ~ 0.8 [43]. This leads to low quality films when SiH_2 is a major precursor, and similar to physical vapor deposition, could create voids and undesired surface roughness and surface defects [37].

To increase deposition rate without sacrificing film quality, several other methods, such as very high frequency (VHF) PECVD and microwave (MW) PECVD, have been investigated.

2.2.2. VHF and MW PECVD of a-Si:H

Very high frequency ($\sim 20\text{-}150$ MHz) PECVD can provide good material properties with high deposition rates [8, 38, 44]. Figure 2.3 shows the deposition rate increases with RF frequency, which provides a method to a lower production cost of a-Si:H solar cells. Another benefit of VHF PECVD is that polyhydride powder does not form, unlike when increasing RF power with standard 13.56 MHz to increase the deposition rate [44].

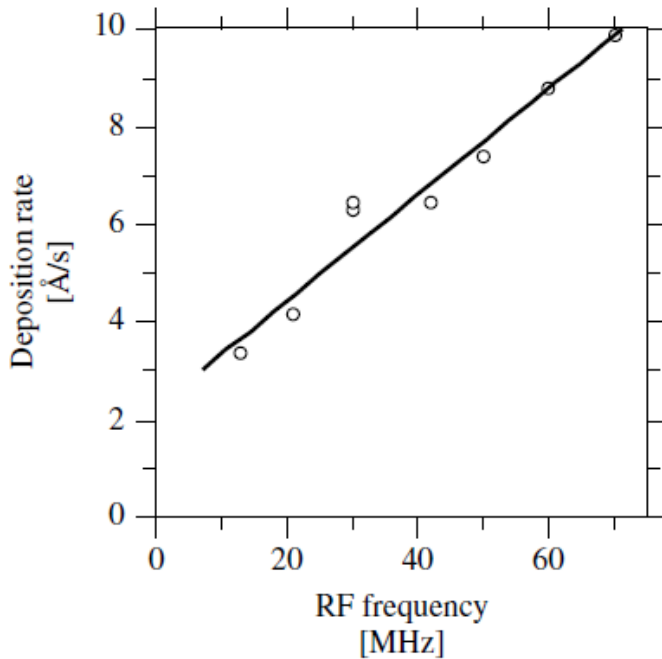


Figure 2.3 a-Si:H film deposition rate as a function of RF frequency at constant power [8].

With 70 MHz RF frequency, the deposition rate is 10 \AA/s , which is 17 times that with standard 13.56 MHz RF frequency at the same RF power [8]. At the same time, light-induced degradation drops from 14% to 10%.

The reasons for higher deposition rate as well as improved film quality at very high frequencies are still under scrutiny. Chatham and coworkers [44] suggested that as frequency increases, the operating pressure can be decreased from 0.39 Torr at 13.56 MHz to 0.05~0.08 Torr at 110 MHz, and the fraction of electrons in the high-energy tail of the electron energy distribution function is enhanced. Therefore, silane gas dissociation and, in turn, the radical density both increase, leading to higher deposition rates. Another important effect realized at high frequency is a decrease of the plasma

potential. As a result, the energy of ions bombarding the growing film surface is in a range which favors high quality film growth. Indeed, Veprek and coworkers showed that such ion bombardment led to the abstraction of hydrogen from the subsurface and further enhanced the bonding of “beneficial” radicals such as SiH₃ to the growing surface [45].

Recently, VHF PECVD has also been used to deposit microcrystalline silicon (μ -Si) films, due to its high efficiency for generating H atoms in the plasma that are important for the formation of nc-Si [46]. However, an important issue with VHF PECVD is the film uniformity on large area substrates. At the conventional 13.56 MHz, the wavelength of the RF wave is 22 m, which is much larger than the size of the substrate. But if a higher frequency is used, such as 70 MHz, the wavelength decreases to 4 m. A standing wave is formed at $\lambda/4$ (i.e., 1 m), which is comparable with the size of the substrate. Therefore, if the electrode has one RF feed at one side, a standing wave may develop causing non-uniform film deposition [38]. To solve this issue, the design for the electrode and location of the RF feed points are important.

MW PECVD uses 2.45 GHz frequency to excite the plasma. With the increase of frequency, the deposition rate is further increased. High quality film deposition takes place either in the afterglow, or with the substrate in a remote location out of direct contact with plasma [8, 38]. A plasma in a carrier gas (such as He, Ar or H₂) is excited by microwaves in a remote chamber, and flows downstream over the substrate. SiH₄ gas is fed just above the substrate, and is decomposed by the excited carrier gas, leading to a-Si:H film growth on the substrate. Due to the high microwave power transferred into the carrier gas at low pressure, a high density plasma is generated with low ion energy. This causes a high degree of dissociation of the SiH₄ feed gas, generating a high density of

SiH_n radicals, hence the deposition rate is high. Microwave plasmas have also been used for nc-Si film growth as shown by the narrow width of peaks in the x-ray diffraction spectrum at low magnetic fields (Figure 2.4) [47].

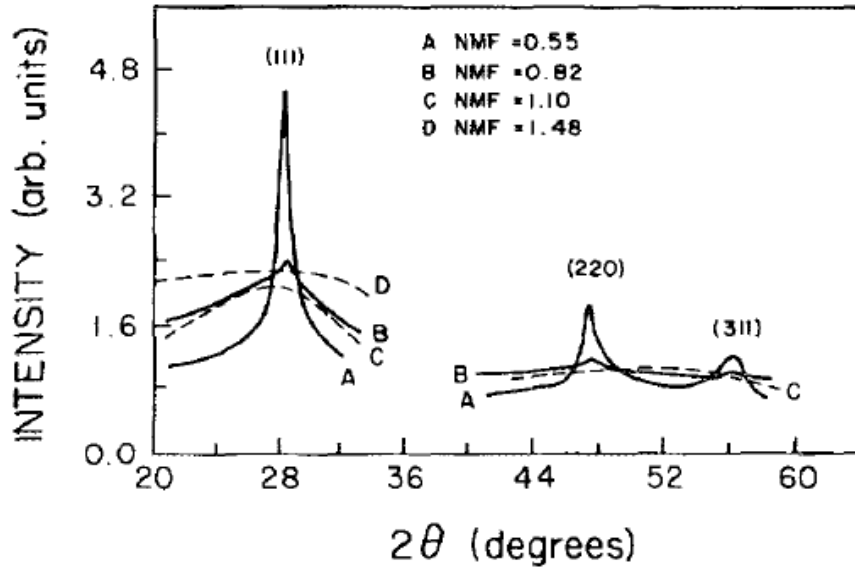


Figure 2.4 X-ray diffraction intensity with normalized magnetic field (NMF) at three scattering angles of crystallite orientation [47]. In this study a microwave plasma system was equipped with a DC magnetic field B along the longitudinal axis of the waveguide. By decreasing B , a transition from amorphous Si to nc-Si:H occurred.

2.2.3. HW CVD of a-Si:H

HW CVD uses thermal excitation of the feed gas on a heated wire (as opposed to electron impact dissociation in a plasma), to generate reactive film precursors. Tungsten or tantalum wires are heated to between 1750 to 1950 °C [38]. Pure SiH₄ gas or SiH₄ mixed with H₂ flows over the wires, and decomposes into radicals through reaction R2.1,



The radicals diffuse in the chamber and deposit on the substrate, which is placed several centimeters away from the wires. The substrate is usually heated to 150-450 °C, to control the film microstructure [8]. Since the energy is not high enough to ionize the gas and generate plasma, the density of ions is almost zero, which is favored for producing good quality films [48]. Gas phase reaction R2.2 between radicals can also assist in the formation of the deposition precursor SiH₃ for high quality films [38],



As early as 1979, when a-Si:H was deposited by the decomposition of silane gas on a carbon or tungsten foil which was heated to 1400-1600 °C [49], pyrolytic methods such as HW CVD produced solar cell materials. With efficient decomposition of the silane gas, the deposition rate is about one order of magnitude higher than conventional PECVD. At the same time the efficiency of solar cells using this technique is 9.8% [50], about the same as for PECVD. Mahan and coworkers also stated that lower H atom content was found in the a-Si:H films grown by HW CVD, which decreased the light-induced degradation compared to films deposited by RF PECVD [51].

Recently, HW CVD was used to deposit nc-Si and polycrystalline silicon films [52, 53]. The crystalline fraction in the material could be fairly high [38]. The drawback of HW CVD is that uniform growth is very difficult to achieve over large areas. The spatial arrangement of the wire is very important for film thickness uniformity [54].

2.3. Light-induced Degradation of a-Si:H

Even though a-Si:H solar cells are low cost, degradation of their performance is a major drawback for their use in practical PVs. Specifically, after the first few hundred hours of light illumination, the cell conversion efficiency falls by about 30% for single-junction cells, and 15% for triple-junction modules [8], as shown in Figure 2.5.

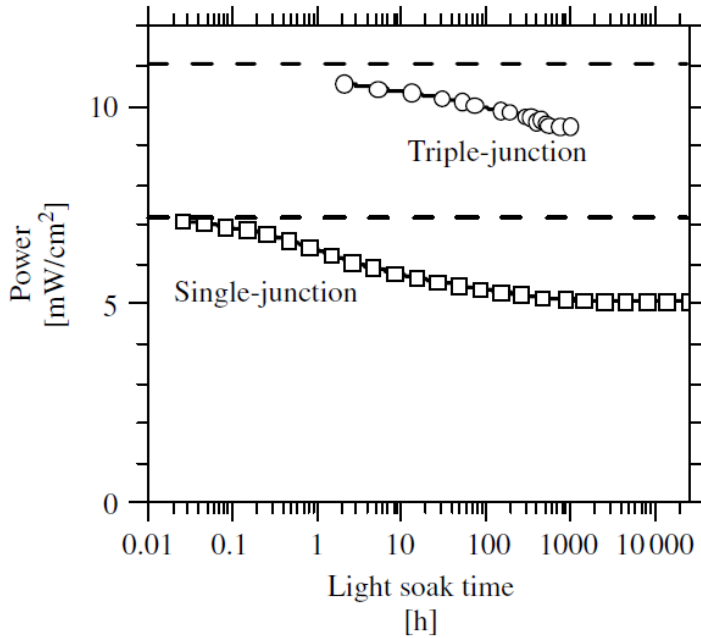


Figure 2.5 The conversion efficiency of a-Si:H-based solar cell modules after the first couple of thousand hours of illumination drops by 30% of its initial efficiency for single-junction cells, and by 15% for triple-junction cells. The dashed line shows the initial power output for each module [8].

This light-induced metastability of the conversion efficiency of a-Si:H was first described by Staebler and Wronski in 1977 [55], and was later called the Staebler-Wronski effect (SWE) [38]. a-Si:H films deposited with silane in a glow discharge experience degradation of efficiency with long durations of light exposure. Changes include the decline of photoconductivity and dark conductivity. However, the optical

properties are not affected [55, 56], as shown in Figure 2.6. Degradation can be reversed by annealing above 150°C in the dark.

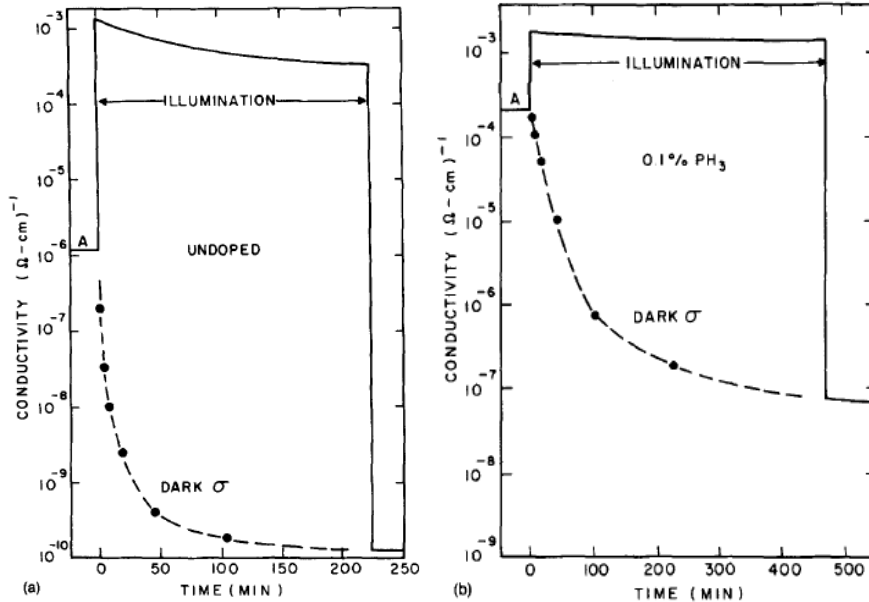


Figure 2.6 Decrease of conductivity and dark conductivity for undoped a-Si:H films (a), and PH₃ doped a-Si:H films (b), during 200 mW/cm² illumination. The starting thermal equilibrium state is marked as A. Solid curves shows conductivity and dashed curves show dark conductivity [56].

The light induced conductivity decreases gradually after the start of illumination. The decrease is more noticeable in undoped a-Si:H films, when compared to that in doped films. By studying the kinetics of this light-induced metastability of a-Si:H, Staebler and Wronski pointed out that the SWE takes place in the bulk of the film rather than its surface [56]. They also stated that degradation is not because of photochemical effects, since the optical properties remain unchanged. Further, they suggested that a possible reason for the decrease of photoconductivity is that light increases the density of recombination centers from 10^{15} cm^{-1} to 10^{17} cm^{-1} [34, 55], which could be defects

introduced by dangling bonds in the material. The decrease of dark conductivity is also consistent with this reasoning in that the Fermi level decreases towards the middle of the gap and thus the activation energy increases, which could be due to the increase of defects in the film [56]. Many subsequent studies of the SWE showed that this effect is related to the increase of the density of silicon dangling bonds in the a-Si:H film, which create recombination centers annihilating the charge carriers created by light absorption.

Two early models to explain the SWE indicate that this effect is intrinsic to amorphous silicon and it is of a localized nature. One model suggests that, during light illumination, photoexcited electrons and holes recombine, thereby releasing energy. The energy is sufficient to break a weak local Si-Si bond, creating two nearby Si dangling bonds. Then, a hydrogen atom in a neighboring SiH moiety reacts with one of the Si dangling bonds, but leaves behind a new Si dangling bond. The remaining two dangling bonds are some distance apart. Similar hydrogen exchange processes can take place in a chain reaction during prolonged light illumination, distributing dangling bonds (thus creating metastable defects) over large distances [31]. Another model proposes that already existing positively and negatively charged dangling bonds create neutral dangling bonds by trapping photoexcited carriers, resulting in midgap states [57, 58]. However, recent evidence does not support either of these models. The latter model was ruled out by the fact that no large concentration of charged defects was found [32]. Further, experiments by Crandall and coworkers focusing on the impurities in a-Si:H films show that increased impurity (e.g., carbon) concentration enhances SWE. This suggests that the SWE is not intrinsic to a-Si:H but is related to the presence of impurities [59].

Branz explained the SWE by a hydrogen collision model [60]. This model proposes that the recombination of photoexcited electrons and holes excites mobile H out of Si-H bonds, and this can be modeled as a mobile Si-H with a mobile dangling bond (Si-H/DB). Diffusion is stimulated by the recombination of e-h pairs with a transport barrier of about 0.3 eV [13]. The barrier for trap-controlled diffusion, to excite mobile H out of Si-H bonds, is about 1.4 eV [14]. Therefore, the mobile Si-H/DB “species” can diffuse extremely fast through the material. The mobile Si-H/DB is destroyed by two possible mechanisms. One is that Si-H/DB meets a fixed dangling bond, forming normal Si-H. Alternatively, when two Si-H/DB meet, their two dangling bonds disappeared by forming a Si-Si bond. With this process, two dangling bonds are formed in regions where two mobile H atoms are excited. The two dangling bonds are spatially isolated from H and also from each other, which can explain the lack of spatial correlation between H and dangling bonds.

More recently, research has focused on solving the SWE problem by creating a more stable structure in a-Si:H films. The approach is to deposit films with small grain structure, which includes microcrystalline ($\mu\text{c-Si:H}$, grain size $\sim 1 \mu\text{m}$) [54] and nanocrystalline silicon (nc-Si:H, grain size $< 20 \text{ nm}$) [38, 54]. Microcrystalline and nanocrystalline silicon films consist of crystalline grains embedded in an amorphous matrix. Recent research has shifted from $\mu\text{c-Si:H}$ to nc-Si:H film growth [15, 61, 62].

2.4. Nature and Benefits of nc-Si:H

nc-Si:H is an inhomogeneous material, consisting of an amorphous phase, crystalline grains and grain boundaries [38]. Due to the ordered structure of nc-Si:H, the optical properties of this material are closer to those in crystalline silicon, rather than amorphous silicon. The optical absorption coefficient of crystalline, amorphous and nc-Si:H is shown in Figure 2.7. Between 1.2 eV and 1.4 eV, the optical absorption coefficients of nc-Si:H and c-Si are nearly the same [12, 63]. The slightly higher absorption coefficient of nc-Si:H at higher energy is due to its amorphous phase [12]. nc-Si:H has an indirect band gap of 1.1 eV similar to c-Si, while amorphous silicon has a direct band gap of 1.7 eV [15].

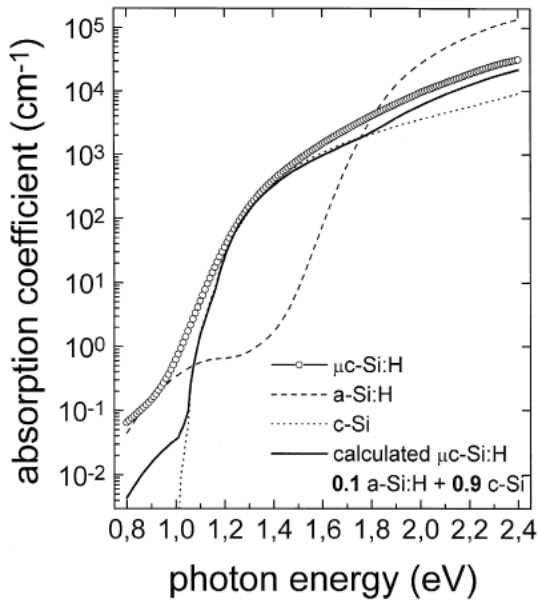


Figure 2.7 Comparison of the optical absorption coefficient of $\mu\text{c-Si}$, a-Si, c-Si, and calculated $\mu\text{c-Si}$ comprised of 10% a-Si and 90% c-Si [12].

From Figure 2.7, nc-Si:H shows a weaker absorption at high photon energy, i.e., in the short wavelength region, compared to amorphous silicon, while in the near infrared, the absorption of nc-Si:H is higher than a-Si. Therefore, nc-Si:H and a-Si:H can be used to form a tandem cell with a-Si as the top component cell and nc-Si:H as the bottom. Such tandem cells were introduced by Meier and coworkers and were termed micromorph devices [64, 65].

Moreover, the most important benefit of nc-Si:H is that the light-induced degradation effect is apparently reduced or even eliminated [32]. Cabarrocas and coworkers studied the SWE for a-Si:H and nc-Si:H with different crystalline fraction [66]. Figure 2.8 shows the dark conductivity change during light soaking.

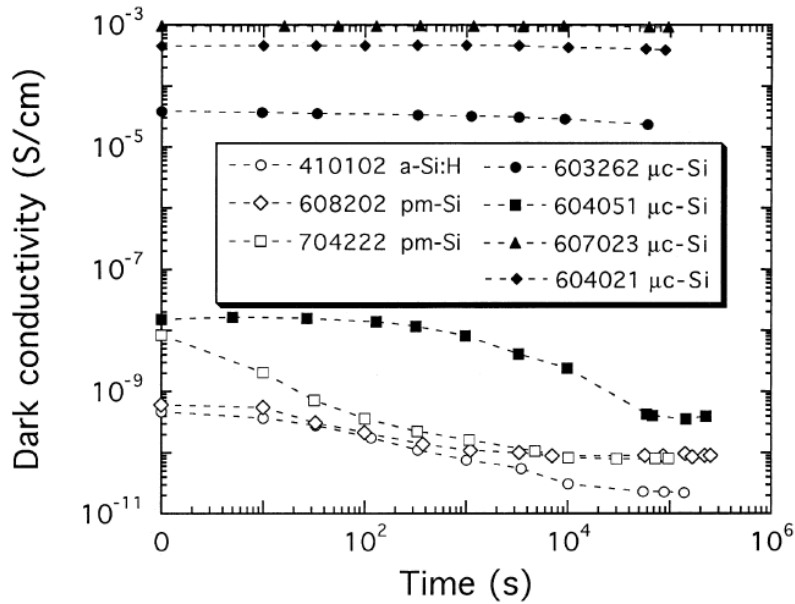


Figure 2.8 Dark conductivity change with time at 30°C, with the accelerated light-soaking tests at 80°C and 350 mW/cm² filtered light. pm-Si has an intermediate ordered structure between amorphous and μc-Si. Two pm-Si films are deposited at different pressure. Four μc-Si films have different crystalline fractions of 67%, 31%, 79% and 96% from top to bottom on the right side of the insert label [66].

For an a-Si film, after 10^5 s light exposure, the dark conductivity decreased to about 1/30 of the initial value, while for a μ c-Si film with 31% crystalline fraction, the dark conductivity fell to about 1/12 of the initial value. Further, the dark conductivity decreases only slightly for a film with 67% crystalline volume fraction, and remains unchanged above 67% crystalline fraction. Quantum efficiency, mobility of carriers and their lifetime also show similar trends, which means that the μ c-Si films can be very stable. Polymorphous silicon films (pm-Si), having an intermediate order structure between a-Si and μ c-Si, were found to be better than a-Si but not as stable as μ c-Si films. These results make it clear that film microstructure plays an important role in stability of several important film properties.

The optical absorption coefficient α (measured at 0.8 eV) corresponds to the defect-related subgap absorption [15, 16], and can be used to evaluate the density of the recombination centers formed during light-soaking. The initial value of α and that after 1000 h of light-soaking are plotted as the function of crystalline volume fraction in Figure 2.9.

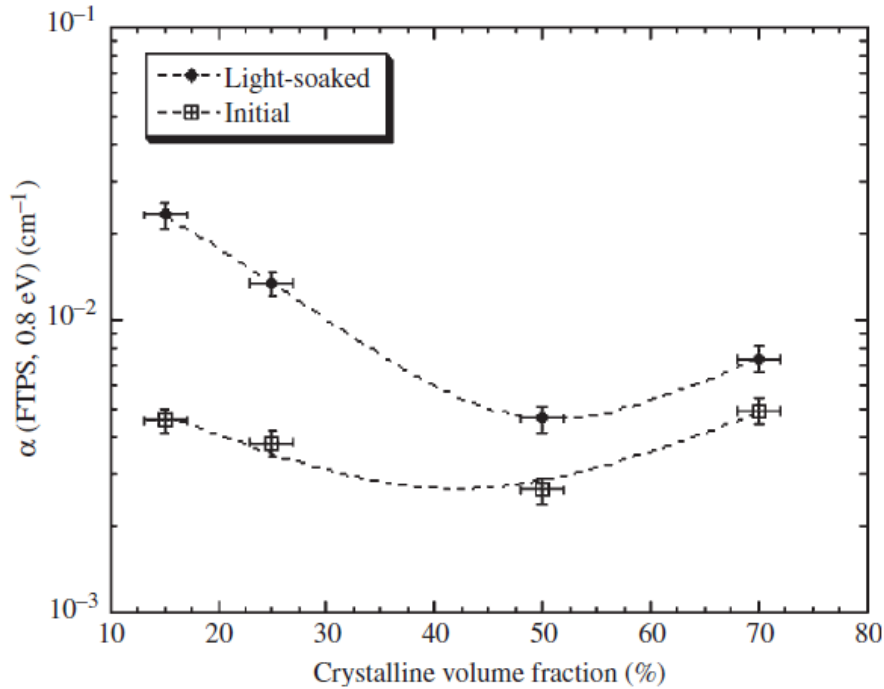


Figure 2.9 The defect-related absorption coefficient at 0.8 eV in the initial state and after 1000 h of light-soaking as a function of crystalline volume fraction for nc-Si:H single junction solar cells [15].

Figure 2.9 shows that in the medium range of crystalline volume fraction X_c (40% ~ 60% estimated from Raman spectra) the defect-related absorption coefficient has a minimum both for the initial value and the post light-soaked state. Further, under high crystalline volume fraction (i.e., >70%), the absorption coefficient α (at 0.8 eV) difference between initial and 1000 h light-soaked states is the smallest. For nc-Si:H with medium crystalline volume fraction, light-induced degradation is still detected, even though it is much smaller than that in a-Si:H [17]. The generally accepted explanation for the SWE in a-Si:H is that defects are generated during light-soaking due to hydrogen diffusion induced by the non-radiative recombination of photo-excited carriers [13, 14,

17]. However, in the nc-Si:H, the small grains, grain boundaries, and the intermediate range order make this mechanism more complicated.

Experiments using light sources with different wavelength show that when nc-Si:H is exposed to longer wavelengths (>665 nm), there is no light-induced degradation; while at shorter wavelengths (<665 nm) or with white light, there is some light-induced degradation [67]. Due to the high bandgap for a-Si:H (1.87 eV), relative to nc-Si:H (1.1 eV) [15], only a small amount of photons with wavelengths >665 nm can be absorbed in the amorphous phase. However, with shorter wavelength light, a large fraction of photons is absorbed in the amorphous phase, which can generate defects and induce degradation. Therefore, degradation is mainly due to the amorphous phase [67] in nc-Si:H.

Later studies of nc-Si:H solar cells with different crystalline volume fraction X_c showed that the degradation does not depend directly on X_c [68]. The experiments were done with different % of hydrogen dilution and showed by using constant hydrogen dilution, X_c (estimated by Raman spectrum using 532 nm laser excitation source) is higher than that for the cells deposited using step hydrogen dilution profiling (i.e., a decrease of hydrogen dilution in discrete steps during deposition) [69]. However, the light-induced degradation is larger when deposition is carried out with constant hydrogen dilution compared to deposition with step hydrogen dilution [68]. Therefore, light-induced degradation is not directly related to the value of X_c . Later, a “back-to-back” model was proposed to explain the effect of grain boundaries on SWE in nc-Si:H [17]. In medium crystalline volume fraction nc-Si:H, the crystal grains are embedding in the amorphous matrix. Crystalline grains with low band gap surround amorphous regions, forming crystalline-phase to amorphous-phase to crystalline phase regions. The

crystalline phase can be assumed to act as n-type compared to the amorphous phase, so this structure forms two microscopic diodes arranged back-to-back (Figure 2.10).

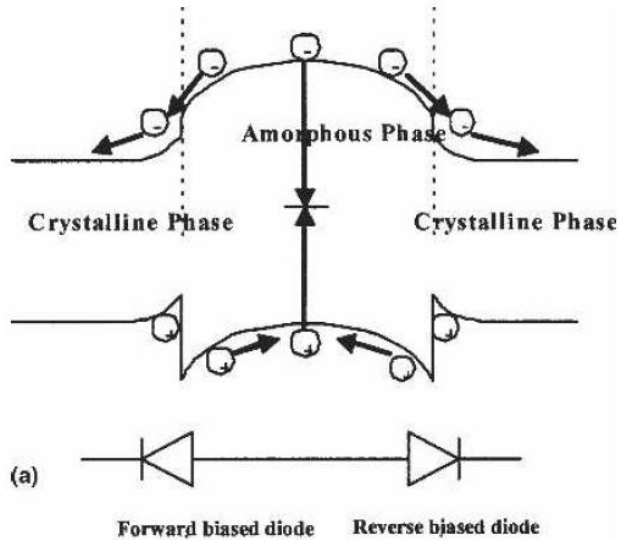


Figure 2.10 Schematic of an amorphous phase surrounded by crystalline phases forming two back-to-back diodes [17].

Electrons flow from the crystalline phase to the amorphous phase and leave holes in the crystalline phase around the boundary. So an internal electrical field is set up, which is from crystalline phase to amorphous phase. During light exposure, the excess electrons which are generated in the amorphous region move to the crystalline region. Electrons recombine with holes in the grain boundary regions and not only in the amorphous phase. Thus, not only does the amorphous component fraction influence the light-induced degradation, but the structure of the grain boundary is also responsible for degradation. This can explain why films with similar crystalline volume fractions have different light-soaking degradation behavior.

2.5. Models of the Kinetics of nc-Si:H Growth

The formation of nc-Si:H has been actively studied. Three main mechanisms for the transition from a-Si:H to nc-Si have been proposed:

(i) *Preferential etching of a-Si:H to leave nc-Si in the film* [27, 28, 70-72]. This mechanism can also explain the decrease in deposition rate by adding increasing amounts of H₂ to the SiH₄ precursor gas. H-atoms formed in the plasma break weak Si-Si bonds and form Si-H bonds with the Si atom having one broken bond, eventually resulting in SiH₄, which desorbs from the surface. The remaining dangling Si bonds either join with other Si dangling bonds or “trap” SiH₃ adsorbates to form stronger bonds. Under favorable conditions, long distance order is established by the emergence of nano-crystalline or micro-crystalline silicon. However because of preferential etching, the deposition rate decreases [72].

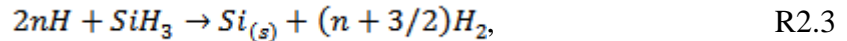
(ii) *Enhanced diffusion of SiH_x* [29]. The thermally activated surface diffusion coefficient D_s is given by Eq. 2.1 [19, 73],

$$D_s \propto a^2 \exp(-E_s/kT), \quad (2.1)$$

where, a is the jump distance between adsorption sites and E_s is the activation energy for a surface-diffusion jump. When an a-Si:H film is exposed to hydrogen atoms, hydrogen atoms “passivate” the surface, reducing the reactivity of the film. As a result, the binding energy between SiH_x and adsorbing sites becomes weaker and E_s decreases. Therefore the mobility and diffusion length of the deposition precursor both increase. Thus the adsorbed precursor can diffuse a longer distance across the surface before finding an

energetically favorable site [72]. As a result the amorphous to crystalline Si transition is favored [73].

(iii) *Chemical annealing model.* This model was introduced by Shimizu and coworkers in 1991 [26]. They modulated the gas feed to first deposit an amorphous silicon film, and then expose that film to H/D atoms. They found that the H concentration in the films decreased by 1% or less after exposure to a hydrogen plasma. They proposed a chemical reaction for the promotion of structural relaxation of the solid, with the aid of atomic hydrogen, which also explained the formation of voids in the bulk of the film. They found that the activation energy for structural relaxation (which was estimated from the change of hydrogen concentration with hydrogen plasma exposure time), was consistent with the activation energy for atomic hydrogen diffusion through the amorphous silicon network [74]. In this model, H diffusion occurs not only along the film surface, but also some hundreds of Å into the subsurface [75]. H-atoms insert into Si-H bonds to relieve strain, and cause Si-Si bonds to relax toward the equilibrium angle and length of crystalline Si [46, 20-23, 76]. The overall reaction is given by R2.3. And the energy released by R2.3 is given in Eq. 2.2 [77],



$$\Delta H = \Delta H_f(SiH_3) + nD(H-H) \approx 2 + n4.5eV. \quad (2.2)$$

The released energy increases the local effective temperature, which promotes the transition from a-Si:H to nc-Si. The silicon network rearrangement enhances the crystalline volume fraction but also results in the formation of free volume in the bulk of the film, which leads to cracks and spherical voids [73]. Drevillon and Solomon used real

time spectroscopic ellipsometry to study layer-by-layer deposition and H exposure [75]. They explained the observed crystallization on the surface as well as in the bulk of the film by using the latter two mechanisms discussed above. They proposed that H exposure caused a porous a-Si:H phase to form through chemical annealing, which was a necessary condition for nucleation of crystallites. After a nucleation layer was formed, selective etching contributed to the crystallization of the surface layer, and H diffusion into the bulk contributed to rearrangement of Si-Si bonds and enhanced the transition to nc-Si.

2.6. Film Characterization

2.6.1. Raman Scattering Spectroscopy

Film structure can be evaluated by Raman scattering spectroscopy. In Raman scattering, a small fraction of laser light incident on the substrate induces vibrational excitation (phonons) similar to infrared absorption and the scattered light shifts to lower frequency. From the magnitude of the frequency shift, the nature of the material and structure can be characterized.

The Raman spectra in this work are measured in a backward scattering configuration using a T64000 (Horiba Jobin-Yvon) spectrometer equipped with a microscope (100X or 50X objective) and liquid-nitrogen-cooled CCD detector. The spectra obtained with 488 nm, 515 nm Ar⁺ and 633 nm He-Ne red laser excitation were practically identical, shown in Figure 2.11.

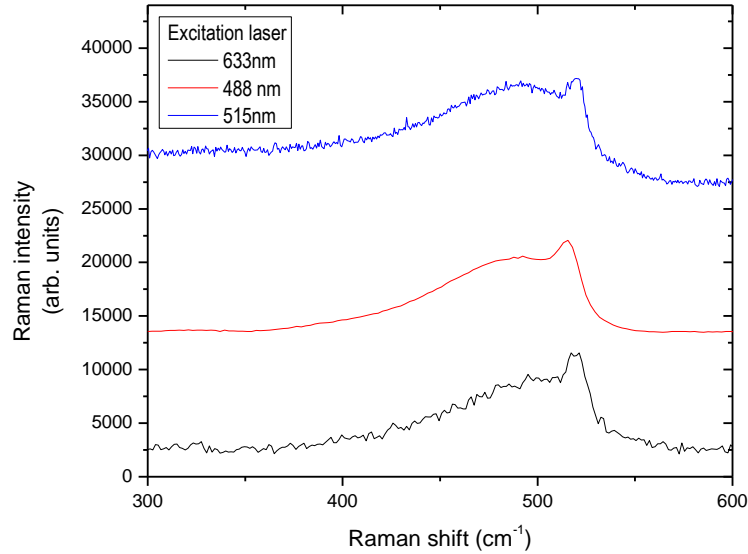


Figure 2.11 Comparison of the Raman spectrum for sample #76 with different excitation laser sources.

The laser power was kept below 5 mW to avoid local heating. The film is composed of both amorphous and crystalline phases. In the amorphous phase, because of the dangling and strained bonds, long range order is lacking, so the transversal optical (TO) mode Raman peak at 480 cm^{-1} is broad (FWHM about 65 cm^{-1}). However, for the crystalline phase, the TO Raman peak at 520 cm^{-1} is comparatively sharp (FWHM less than 10 cm^{-1}) [16, 24, 35].

The resolvable TO peaks provide a qualitative and convenient method for estimating the crystalline volume fraction in the film. There are two ways to determine the crystalline volume fraction [62]: the two-peak method and the three-peak method.

In the two-peak method, the spectrum is deconvoluted into two peaks, one near 480 cm^{-1} for the amorphous structure and the other at 520 cm^{-1} for the crystalline component. The crystalline volume fraction X_c is given by Eq. 2.3,

$$X_c = \frac{I_{520}}{I_{480} + I_{520}}, \quad (2.3)$$

where, I_{480} and I_{520} are the integrated areas of the two individual Gaussian peaks at around 480 cm^{-1} and 520 cm^{-1} .

In addition, the size of crystallites in the film can be estimated by the TO shift of the amorphous peak, relative to the crystal peak by the following equation [78-80],

$$L = \sqrt{\frac{88.43}{\omega_{TO} - \omega_0}}, \quad (2.4)$$

where, ω_0 (cm^{-1}) is the TO-phonon peak of the single crystal, ω_{TO} (cm^{-1}) is the position of the amorphous-like TO mode and L is the averaged diameter of the ordered structure.

In the three-peak method, the Raman spectrum is deconvoluted into three peaks: 480 cm^{-1} for the amorphous component, 520 cm^{-1} for the crystalline component, and a third intermediate component at 500 cm^{-1} to 510 cm^{-1} , which is attributed to small crystallites [70, 80-82]. The crystalline volume fraction X_c can be estimated from the deconvoluted spectra using the following equation:

$$X_c = \frac{I_{510} + I_{520}}{I_{480} + I_{510} + I_{520}}, \quad (2.5)$$

where, I_{480} , I_{510} and I_{520} are the integrated areas of the three individual Gaussian peaks at 480 cm^{-1} , 510 cm^{-1} and 520 cm^{-1} , respectively. In the analysis of Raman spectra given below, a comparison for these two methods will be presented.

The crystalline volume fraction X_c estimated by Raman scattering is the lower limit for the actual crystalline fraction in the film [70]. There are three reasons for that: (i) The assignment of the 480 cm^{-1} peak to only amorphous Si can be an overestimation, because this feature could also result from grain boundaries in nc-Si, as well as atoms bonded on the surface of the crystallites [83, 84]. (ii) Raman cross section for nano-crystals with grain size larger than 30 \AA is weaker than the cross section for amorphous silicon for the 514.5 nm excitation laser [85]. (iii) the optical absorption coefficient of amorphous silicon is larger than that of nano-crystalline silicon [70, 83]. At a wavelength of 496.5 nm , the absorption coefficients are $1.34 \times 10^5\text{ cm}^{-1}$ and $1.68 \times 10^5\text{ cm}^{-1}$ for the microcrystalline silicon and amorphous silicon respectively. Tsu and coworkers proposed to use a correction factor y to compensate the above effects on the crystalline volume fraction by the equation below,

$$X_c = \frac{I_c}{I_c + yI_a}, \quad (2.6)$$

where I_c and I_a are the integrated intensity of the crystalline peak and amorphous peak. The factor y varies with the crystallite size. Bustarret et al. showed that $y=1$ when the crystallite is smaller than 30 \AA , decaying exponentially to $y=0.1$ when the crystallite size is large. The pertinent equation is [85],

$$y(l) = 0.1 + \exp\left(-\frac{l}{250}\right), \quad (2.7)$$

where l is the diameter of the crystallite in \AA . Based on the TEM images and the estimation of the crystallite size from the Raman peak shift, the crystallite size in the present work is up to around 67\AA and the corresponding $y = 0.88$. As the crystallite size increases, y decreases and, without correction, the crystalline volume fraction will be smaller than the actual value, especially for sample with large crystallites.

It has been shown that when the crystallite size is between 2.2 nm to 5.3 nm, it is hard to obtain a good fit using the two-peak method [81, 86]. Feng and Jackson's group used a strong phonon confinement (SPC) model to estimate the size of crystallites from the Raman spectrum. When they fit the Raman spectrum with the two-peak method, the crystallite size obtained from the SPC model strongly disagreed with the size from X-ray diffraction in this region. However, adding the two peaks around $505\sim 509 \text{ cm}^{-1}$ and another around at $512\sim 517 \text{ cm}^{-1}$ in addition to the amorphous peak, a much better fit and identical crystallite size were obtained. They suggested that the component of $505\sim 509 \text{ cm}^{-1}$ is from the near-surface region over the crystallite core which has different vibrational frequencies than crystallites with large sizes [81]. They also found the crystallite size in this region to be proportional to the ratio of the integrated area under the $\sim 517 \text{ cm}^{-1}$ to that of the $\sim 509 \text{ cm}^{-1}$ peak, as shown in Figure 2.12.

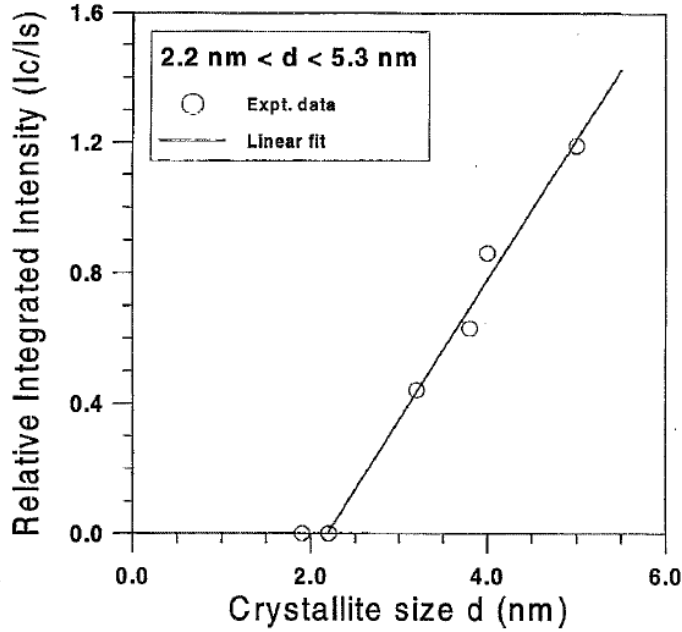


Figure 2.12 Integrated intensity ratio between 517 cm^{-1} peak and peak around 509 cm^{-1} as a function of crystallite size [81].

The crystallite size can be estimated by the shift of the amorphous peak and the crystalline component peak [87-89]. Both the amorphous and crystalline peaks shift towards higher frequency when the crystallite size increases, as shown in Figure 2.13. A simple simulation was performed and the results, shown in Figure 2.13 (a) as crosses, agree with the experiments results. In the simulation, a lower limit for the phonon vector k_0 was assumed. k_0 is determined by Eq. 2.8,

$$k_0 = \pi/\lambda_0 = \pi/a, \quad (2.8)$$

where a is the finite crystallite size and λ_0 is the excitation laser wavelength. The selection rule $k \approx 0$ is modified to be $k_0 \approx \pi/a$ for Raman scattering of a finite lattice of $\mu\text{c-Si:H}$ [89].

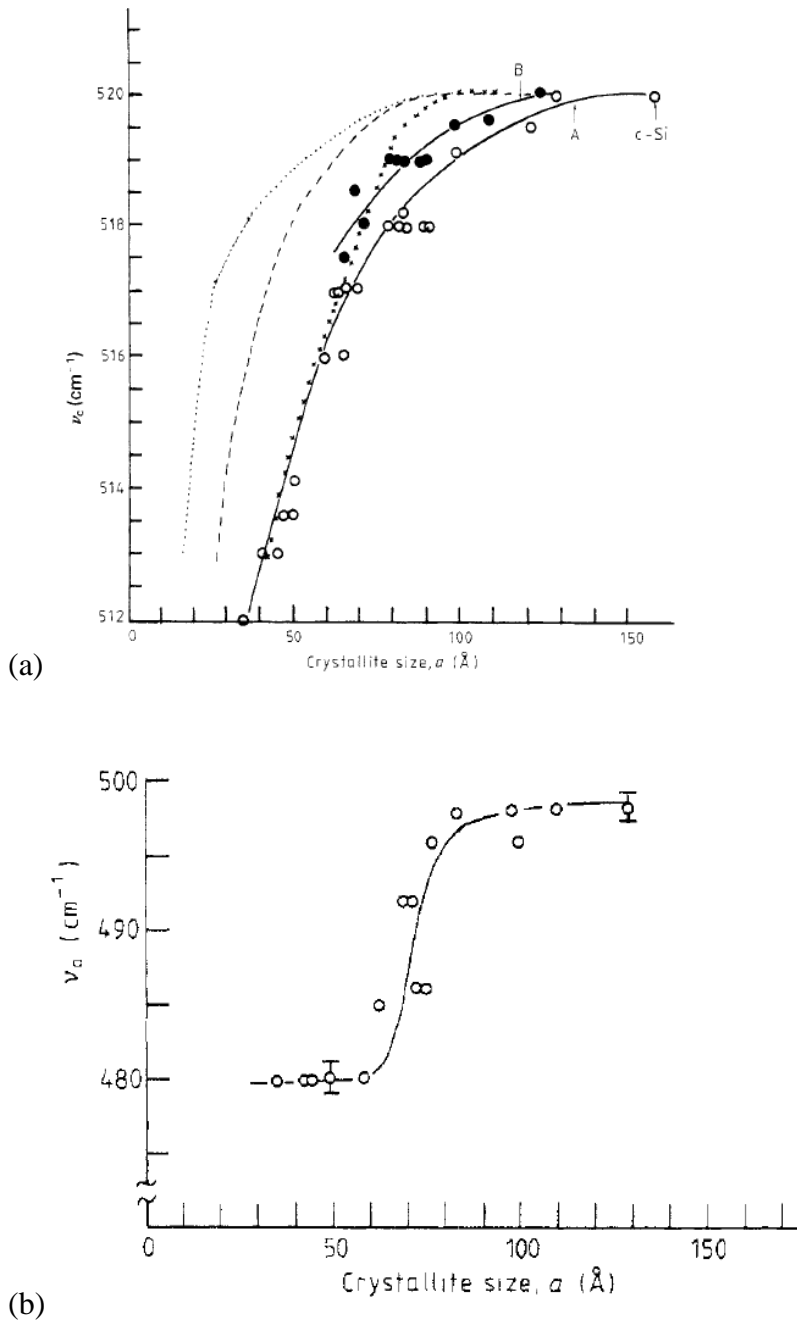


Figure 2.13 Plot of Raman peak frequency against crystallite size, which is measured by x-ray diffraction. (a) peak location (near to 520 cm^{-1}) with crystallite size for unannealed (open circles) and annealed (filled circles) samples of $\mu\text{c-Si:H}$; the other dotted curves and solid curve are from simulation results; (b) peak location (near to 480 cm^{-1}) as a function of crystallite size [89].

Moreover, the crystallite size can also be evaluated by the broadening of the crystalline peak [78, 79]. The TO mode peak of nc-Si:H shifts towards shorter wavenumbers compared to that in single crystal Si. The additional disorder-induced broadening ΔW_R of the crystalline peak in the nc-Si:H film with respect to the TO-phonon peak of single crystal Si (FWHM $\sim 4 \text{ cm}^{-1}$ from our Raman spectrum for single crystal Si) is determined by Eq. 2.9 [78],

$$\Delta W_R = -B(k_0)^2 \text{ cm}^{-1}, \quad (2.9)$$

where constant B is around $224 \text{ cm}^{-1} (10^{-1} \text{ nm})^2$ for nc-Si:H, and k_0 is the phonon wave vector which can be obtained by Eq. 2.8. Therefore, the crystallite size a in Eq. 2.8 can be determined by Eq. 2.10,

$$a = 2\pi(B/\Delta W_R)^{1/2} 10^{-1} \text{ nm}. \quad (2.10)$$

The crystallite size a calculated by the crystalline peak broadening is quite consistent with the x-ray diffraction measurements as shown in Figure 2.14.

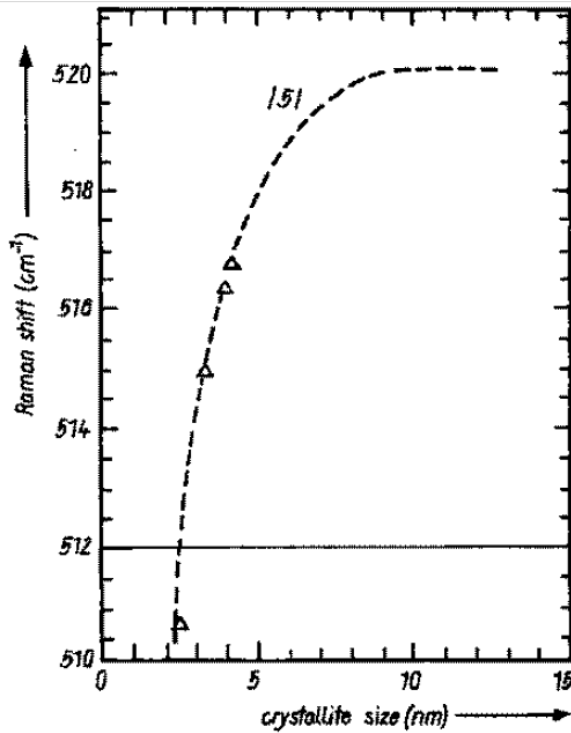


Figure 2.14 Plot of the crystalline peak location as a function of crystallite size; Δ is the experimental results and the dashed curve is from the model [78].

2.6.2. Transmission Electron Microscopy

Raman spectroscopy gives a quantitative measure of the crystalline volume fraction of nc-Si:H. Transmission electron microscopy (TEM) can be used to investigate the detailed film microstructure. Figure 2.15 (a) shows electron diffraction patterns reported by L. Houben, et al. [70], obtained from cross sectional TEM samples. The corresponding Raman spectra are shown in Figure 2.15 (b). The bright spot at the center originates from the Si (001) substrate. The prominent dots in the three inner rings are the spotty Debye-Scherrer rings. The radii are the reciprocal distances of the {111}, {220} and {311} lattice planes of crystalline silicon [70]. The relatively apparent spotty Debye-Scherrer rings can be found in images (a) to (c), for a film deposited with less than 5.7%

by volume silane in hydrogen. For the films deposited with high fraction of silane in H_2 , sample (e), the Raman spectrum shows that the film structure is more amorphous-like. The diffraction pattern also shows scattering from amorphous film.

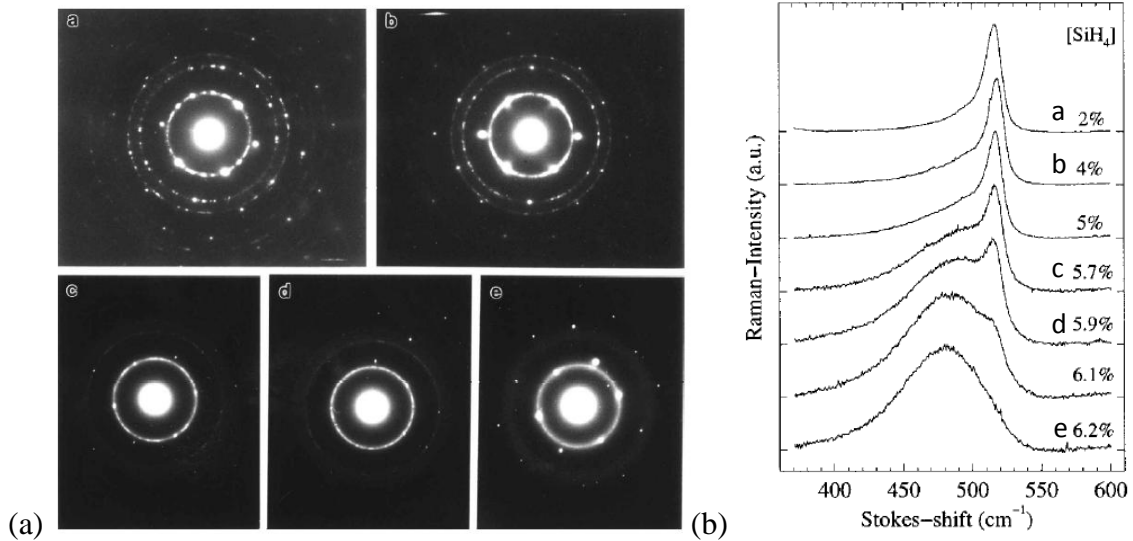


Figure 2.15 (a) Diffraction patterns from cross-sectional TEM samples. The Raman spectra for samples **a** to **e** are shown in (b). The samples are deposited with different silane concentrations in hydrogen (from 2% to 6.2% silane by volume) [70].

Dark-field TEM images obtained in that study [70] show the crystallites and their growth orientation. With high dilution of silane in hydrogen, high crystalline volume fraction as well as strong columnar growth is found, as shown in Figure 2.16 (a). The Raman spectrum for the sample in Figure 2.16 is given in Figure 2.15 (b). With decreasing crystalline volume fraction from Figure 2.16 (a) to (d), the crystallite size decreases and the crystalline column is shorter, but the column is always aligned parallel to the growth direction. For the low crystalline volume fraction sample, TEM image (d) shows small crystallites embedded in an amorphous phase.

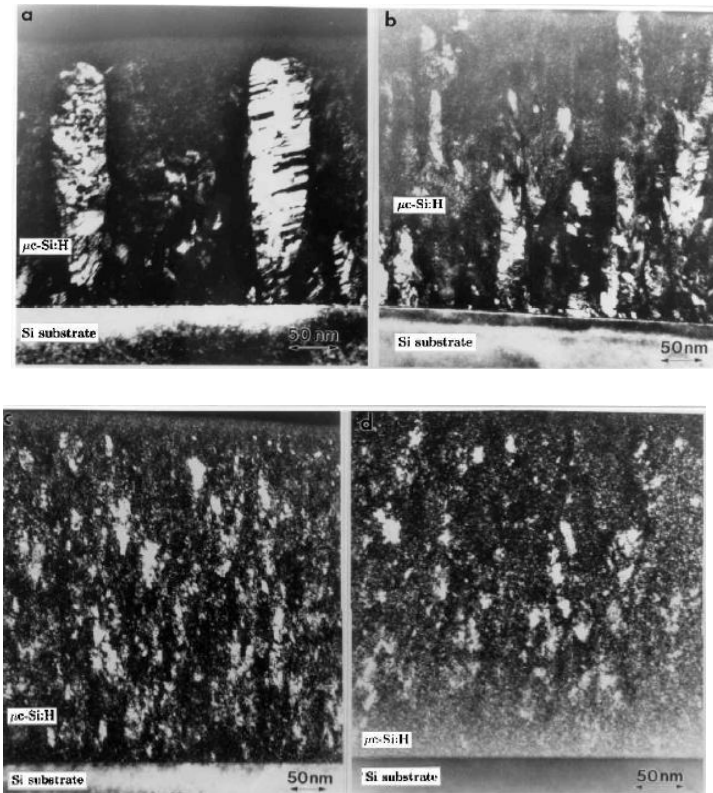


Figure 2.16 Cross-sectional dark-field TEM images of nc-Si:H, (a) strong columnar growth under the high hydrogen dilution deposition condition, 2% silane in H₂, (b) 4% silane in H₂, (c) 5.7% silane in H₂, (d) 5.9% silane in H₂. The bright regions correspond to the crystalline grains with the same orientation according to the incident electron beam [70].

A high resolution bright-field lattice image of a crystal grain is shown in Figure 2.17. There is almost no amorphous phase around the grain. The orientation of the grain can be identified by the {111} lattice fringes.

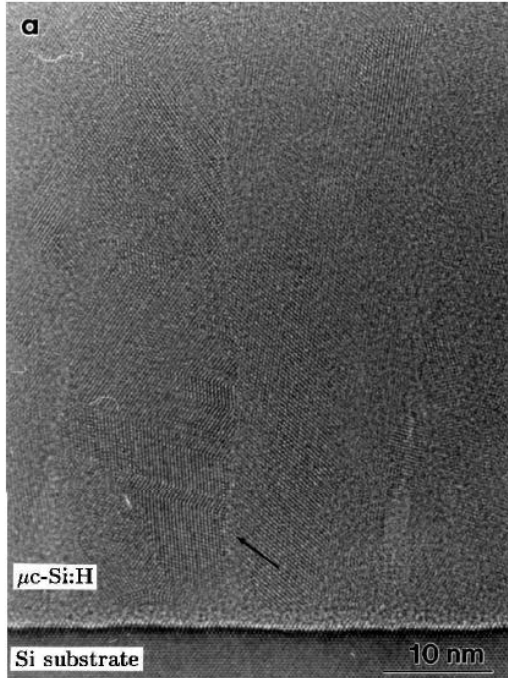
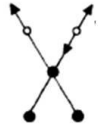
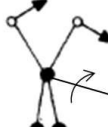


Figure 2.17 High resolution TEM image of the cross-sectional sample with high crystalline volume fraction. The arrow points out a narrow grain boundary [70].

2.6.3. Infrared Absorption Analysis

Infrared absorption is used to measure the amount of hydrogen in the film as well as the type of bonding between Si and hydrogen atoms. Usually, three spectral ranges are analyzed: the stretching ($1850 \text{ cm}^{-1} \leq \omega \leq 2250 \text{ cm}^{-1}$), bending ($800 \text{ cm}^{-1} \leq \omega \leq 1000 \text{ cm}^{-1}$) and wagging or rocking vibrational modes ($550 \text{ cm}^{-1} \leq \omega \leq 800 \text{ cm}^{-1}$) [38, 90, 91]. The types and vibration frequencies of Si-H bonds are shown in Table 2.1 [8, 90, 91].

Table 2.1 Si-H bonds type and vibration frequency.

Type of bonds	Stretching	Bending	Wagging/Rocking
SiH	 2000 cm ⁻¹		 630~640 cm ⁻¹
Isolated SiH ₂	 2090 cm ⁻¹	 880 cm ⁻¹	 630~640 cm ⁻¹
Clustered (SiH ₂) _n	 2090~2100 cm ⁻¹	 890 cm ⁻¹	 845 cm ⁻¹ 630~640 cm ⁻¹

The absorption feature at 630~640 cm⁻¹ is due to the wagging/rocking mode of the bonded hydrogen in species like SiH, SiH₂ and clustered (SiH₂)_n, and SiH₃ [8, 38, 91]. Therefore, the integrated intensity at 630~640 cm⁻¹, after deconvolution of the infrared absorption spectrum can be used to evaluate the hydrogen content using Eq. 2.11 and Eq. 2.12,

$$I_{640} = \int_{-\infty}^{+\infty} \alpha_{640}(\omega) d\omega/\omega, \quad (2.11)$$

$$[H] = A_{640} I_{640}, \quad (2.12)$$

where $\alpha_{640}(\omega)$ is the absorption coefficient, which is the sample transmittance over the substrate transmittance, ω is wave number, and A_{640} is a proportionality constant.

$A_{640} = 2.1 \times 10^{19} \text{ cm}^{-2}$ is widely used to obtain the hydrogen content from the wagging or rocking mode [38]. The hydrogen content in the bonds of SiH and SiH₂ can be

estimated using Eq. 2.13 [90]. From Table 2.1, the stretching mode frequencies for SiH and SiH₂ are around 2000 cm⁻¹ and 2100 cm⁻¹ respectively,

$$C_H(\text{SiH}) = A_{2000} I_{2000} / 5 \times 10^{22},$$

$$C_H(\text{SiH}_2) = A_{2100} I_{2100} / 5 \times 10^{22}, \quad (2.13)$$

where I_{2000} and I_{2100} are the integrated intensity at frequency 2000 cm⁻¹ and 2100 cm⁻¹. The proportionality constants A_{2000} and A_{2100} given by $A_{2000} = (7.4 \pm 1.0) \times 10^{19} \text{ cm}^{-2}$, $A_{2100} = (2.1 \pm 0.2) \times 10^{20} \text{ cm}^{-2}$, $5 \times 10^{22} \text{ cm}^{-2}$ is the atomic density of crystalline Si [90]. According to Table 2.1, the integrated intensities at 880 cm⁻¹ and 845 cm⁻¹ are used to estimate the density of isolated SiH₂ and near-neighbor pairs of SiH₂ groups [8, 90].

The ratio R in Eq. 2.14 is called “microstructure parameter” [38],

$$R = \frac{I_{2000}}{I_{2000} + I_{2060 \sim 2100}}. \quad (2.14)$$

Several studies show that the trend of I - R with changing process parameters is consistent with the change of crystalline volume fraction in nc-Si:H [24, 27, 92].

2.6.4. Spectroscopic Ellipsometry

As a nondestructive diagnostic method, spectroscopic ellipsometry (SE) is used to investigate thin film properties, such as thickness, surface roughness, voids content and optical properties [22, 93-95]. The optical properties depend on the microstructure of the film: a-Si:H, nc-Si:H and poly-Si have considerably different optical properties. The

different optical absorption coefficients for c-Si, a-Si and nc-Si:H have been shown in Figure 2.7.

In SE, two main experimentally measured quantities, the amplitude ratio upon reflection $\tan \Psi$, and phase shift $\cos \Delta$, are defined by Eq. 2.15 [95-97],

$$\tan \Psi e^{i\Delta} = \rho = r^p / r^s, \quad (2.15)$$

where, ρ is the Fresnel reflection coefficient ratio, and r^p and r^s are the Fresnel reflection coefficient for light polarized parallel and perpendicular to the plane of incidence, respectively. The film usually consists of several components, such as amorphous and crystalline phases. A model is built up to simulate the structure of the film. Then, the calculated Ψ and Δ based on the model are compared with experimental data. The difference between the two is evaluated by using the mean square error (MSE), given by Eq. 2.16 [95],

$$MSE = \frac{1}{N} \sum_{i=1}^N [(\tan \Psi_i^m - \tan \Psi_i^c)^2 + (\cos \Delta_i^m - \cos \Delta_i^c)^2], \quad (2.16)$$

where N is the number of measurements, and superscripts m and c stand for the measured and calculated values, respectively. MSE is minimized to obtain a “good” fit.

Due to the complex microstructure of nc-Si:H, the model is complicated especially for the near surface layer [95-97]. The model usually consists of several layers and each layer can be a composite mixture of amorphous silicon, crystalline Si and voids. The layers in nc-Si:H are often modeled using the Bruggeman effective medium approximation (B-EMA) [95, 96]. The requirement for using the B-EMA is that the crystallites are randomly distributed in the layers and the grain size is at least 10 times

smaller than the incident wavelength. However, the grain size must be large enough to have the dielectric response of bulk material [95]. A model using the B-EMA shows good fitting with measured data, and the grain size is about 10 nm based on TEM images [95]. The layers in the model, for 10 nm grain size nc-Si:H, and the fitting of $\tan \Psi$ and $\cos \Delta$ are shown in Figure 2.18 (a) and (b).

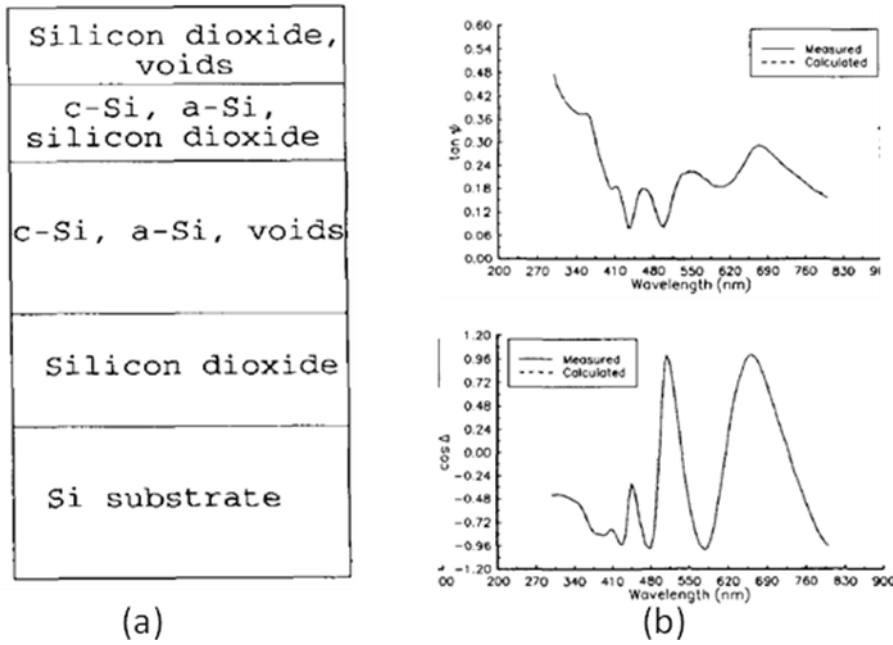


Figure 2.18 (a) five different layers for the nc-Si:H film, including the surface layer with silicon dioxide and voids used to represent the roughness, interface layer consisting of c-Si, a-Si and silicon dioxide, the main film layer including c-Si, a-Si and voids, the interface between the deposited film and substrate and the silicon substrate layer. (b) Based on the model in (a) good fitting of $\tan \Psi$ and $\cos \Delta$ is obtained between the measured data (solid curves) and the calculated data (dashed curves) [95].

Based on the measured $\tan \Psi$ and $\cos \Delta$, the pseudodielectric function $\langle \epsilon \rangle$ can be calculated from Eq. 2.17,

$$\langle \epsilon \rangle = \langle \epsilon_1 \rangle + i \langle \epsilon_2 \rangle = \sin^2 \theta \{ 1 + [(1 - \rho)/(1 + \rho)]^2 \tan^2 \theta \}, \quad (2.17)$$

where θ is the angle of incident light and ρ is the Fresnel reflection coefficient ratio in Eq. 2.15. Typical real and imaginary dielectric functions ϵ_1 and ϵ_2 for a-Si, nc-Si (undoped) and poly-Si (As doped) are shown in Figure 2.19.

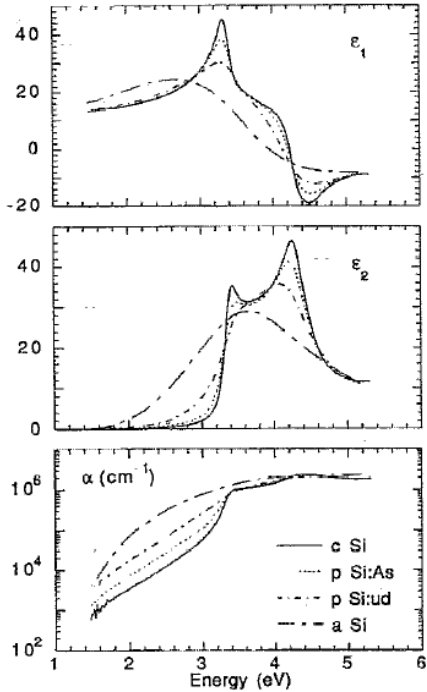


Figure 2.19 Real ϵ_1 and imaginary ϵ_2 dielectric function for crystal Si (marked as c Si), polycrystalline silicon doped with As (p Si:As), undoped nc-Si (p Si:ud) and amorphous silicon (a Si) as a function of incident light energy and the optical absorption coefficient for these four silicon film structures [96].

The apparent difference of the dielectric function ϵ_1 and ϵ_2 for c-Si, p-Si and nc-Si can be observed. There are mainly two peaks located at around 3.4 eV and 4.2 eV for c-Si as well as polycrystalline silicon. For nc-Si film, the two peaks at 3.4 eV and 4.2 eV can still be observed, despite the lower intensity compared to polycrystalline Si and c-Si due to the smaller grain size [93, 94, 96, 98]. However, for a-Si, the peak at 4.2 eV is not seen and the peak at around 3.4 eV shifts towards lower energy. Several groups have

used in-situ SE to monitor the film thickness and dielectric function changes during deposition and nano-crystallization [27, 94, 99].

2.7. Spatially Separated Deposition

In the present work, two separate plasma sources, with rotating substrates exposed to the sources sequentially, were used to spatially separate a-Si:H deposition from nano-crystallization. This kind of spatially separated processing has been reported in atomic layer deposition (ALD) [100-102], including surface reaction studies [103].

In ALD, different gases are used as deposition precursor and oxidizer. In conventional ALD, a single reactor is used, and the gases are introduced in the reactor sequentially. However, purging of the excess gas is required after each gas exposure step [101, 102], resulting in a relatively long cycle time. The deposition rate is limited by the gas residence time, and it is only of the order of 0.01 nm/s [101]. Spatially separated ALD was patented [104] in 1977 by Suntola and Antson (Figure 2.20). The substrates (#14) were rotated above two plasma sources (#13a and 13b) in a single vacuum chamber (#10). Inert gas was used between the two plasma sources to block gas intermixing. The design of the gas outlet could also play an important role in preventing gas crosswalk [101]. Using spatially separated sources, the deposition rate could reach 1.2 nm/s [101]. So-called spatial ALD with linear motion of the substrates has also been reported, as shown in Figure 2.21 [100, 102].

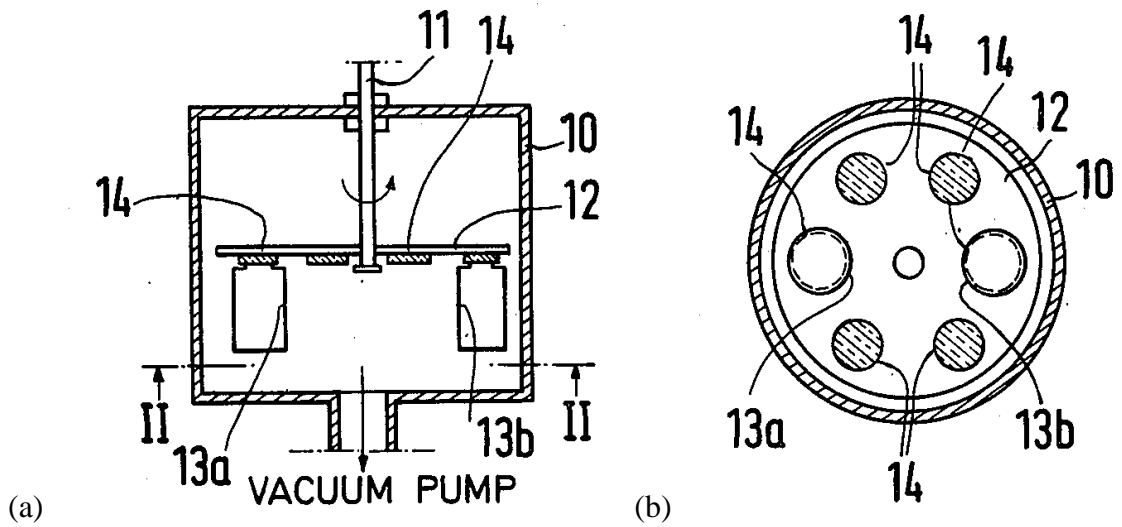


Figure 2.20 (a) Schematic of two plasma sources (#13a and 13b) enclosed in a single vacuum chamber (#10) with rotating substrates (#14). (b) Top view for the wafer holder with six substrates [104].

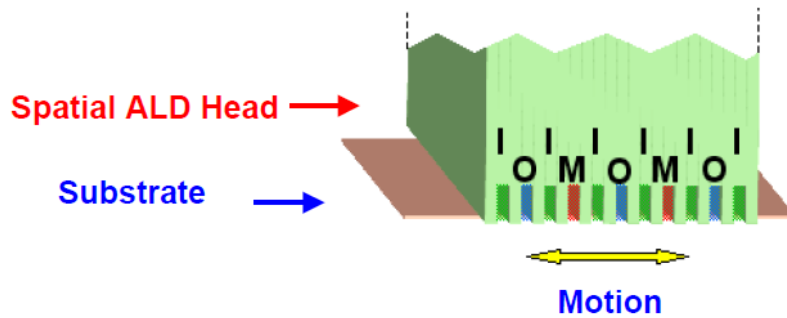


Figure 2.21 Schematic of spatial ALD with gas channels arranged sequentially, and the substrate moving with constant speed underneath the gas channels [102].

Reuter and coworkers [103] used two spatially separated microplasma jets and rotating substrates to study the kinetics of carbon impurity removal from SiO_2 films deposited using hexamethyldisiloxane (HMDSO) as the deposition precursor. SiO_2 with

significant carbon contamination was deposited when pure HMDSO was used in a single jet configuration. However, by adding O₂ into the gas, the carbon content was decreased. To study the mechanism of carbon removal, the process was separated into (a) deposition using a microplasma jet with HMDSO/He and (b) carbon gasification using a separate microplasma jet with an oxygen/helium mixture. The substrates were sequentially rotated under the two plasmas. Using a 5 Hz rotation frequency, the deposited film had similar properties (based on FTIR analysis) with that grown using HMDSO mixed with O₂ in a single jet configuration. They concluded that carbon is eliminated from the film via reaction of atomic oxygen with the surface [103].

Chapter 3. Experimental Apparatus

A novel dual-plasma source was designed and built for a-Si:H deposition and nano-crystallization. Figure 3.1 shows a schematic of the experimental apparatus. Inside a vacuum chamber, a capacitively coupled plasma (CCP) source is operated with SiH_4 diluted with He gas to grow a-Si:H layers. H_2 or D_2 gas is used in an inductively coupled plasma (ICP) source to crystallize the a-Si film. The CCP source provides radicals such as SiH_3 and SiH_2 , which were the dominant precursors for a-Si:H deposition in SiH_4 plasmas [26, 40]. The ICP source provides H or D atoms to induce nano-crystallization [105]. Substrates were placed in cut-out wells in a susceptor that was connected to a rotary feed-through and stepping motor. The substrates were mounted upside down facing the plasma, avoiding accumulation of dust particles during deposition. Home-made heaters were used to heat two of the substrates up to 300°C .

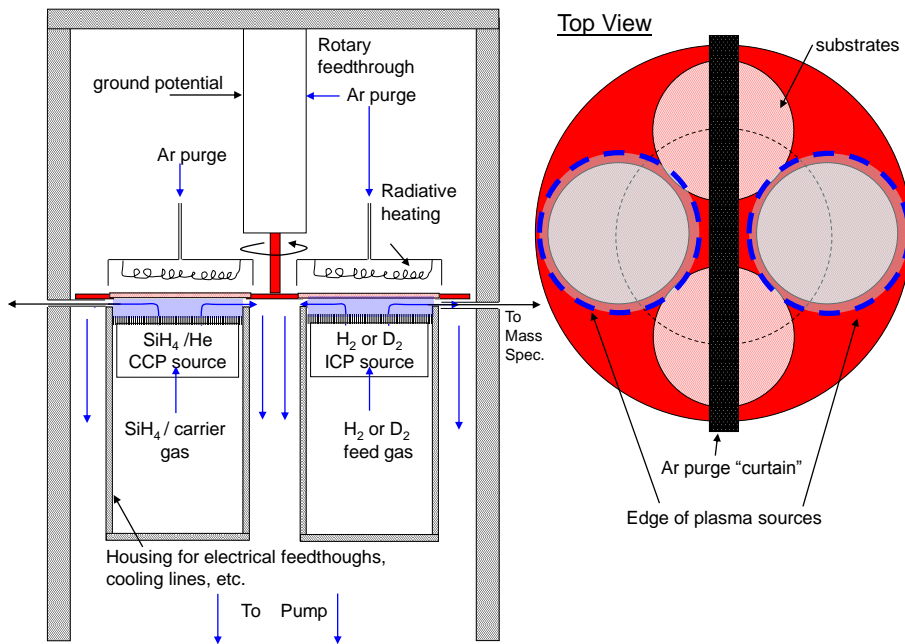


Figure 3.1 Schematic of the dual plasma source with rotating susceptor.

3.1. Capacitively Coupled Plasma (CCP) Reactor Design

Figure 3.2 shows a schematic of the CCP source. Gas flowed into the plasma region from the bottom through a showerhead. Ceramic standoffs were used in the middle (at the ceramic plate location) to isolate the gas feed line, water lines and supports from the applied RF power. Above the ceramic plate, all the metal connectors and rods were at RF potential, while below the ceramic plate, the metal parts were grounded. Figure 3.3 shows the design of the ceramic plate with several holes for the electric feed-through, two supports, 2 water lines and a gas line.

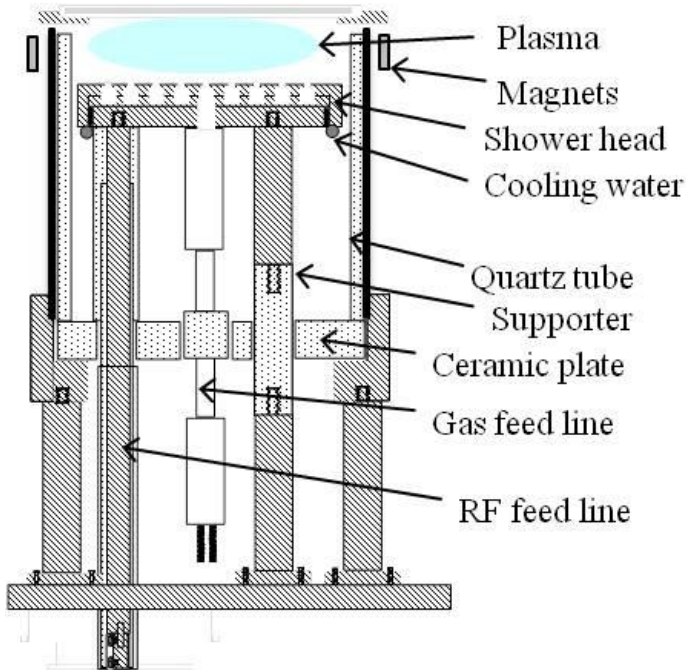


Figure 3.2 Schematic of the CCP source

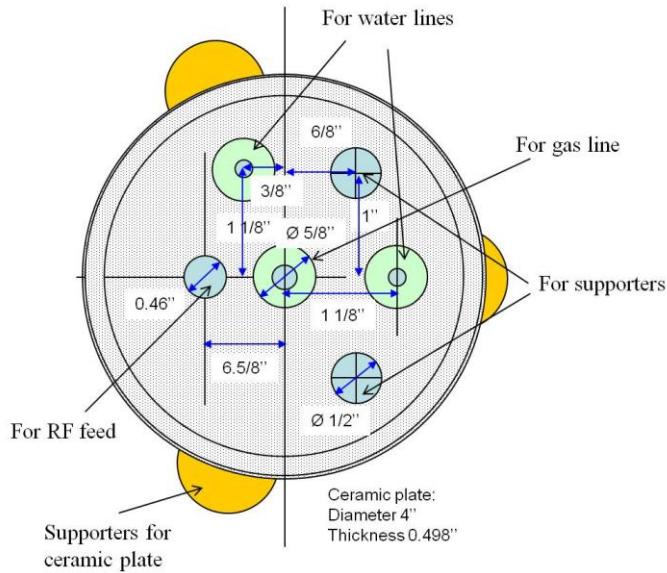


Figure 3.3 Top view of the ceramic plate with holes for gas line, RF feed line, two water lines and supports.

The SiH_4/He CCP was formed between a grounded substrate (top part of Figure 2.2) and an RF showerhead electrode. The gap between the electrode and the substrate was 20 mm. RF power was delivered to the showerhead through a metal rod using an electrical feed through. Power was provided by a function generator (Hewlett Packard model 3325A) and RF power amplifier (ENI model A-150). The output of the amplifier was connected to the electrode through a π -type matching network. A schematic of the matching network is shown in Figure 3.4. Two Bird meters were used to monitor the forward and reflected power before the matching network. The capacitor before “RF out” in Figure 3.4, is used to block DC current generated because of the different areas of the powered and grounded electrodes (blocking capacitor). The two variable capacitors and the inductor can be tuned to minimize the reflected power.

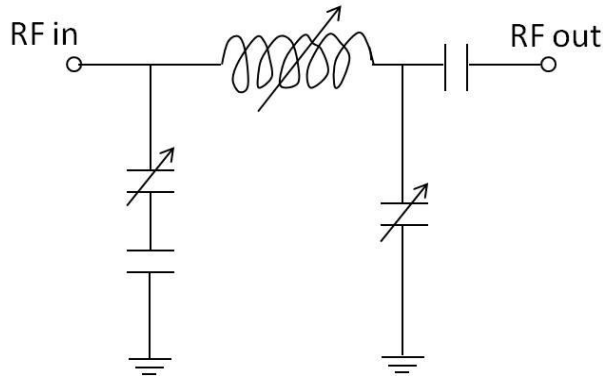


Figure 3.4 Schematic for CCP π -type matching network.

The showerhead electrode, shown in Figure 3.5 (a), has more than 1200 holes with 0.7 mm diameter to provide uniform gas flow. The small hole diameter prevents plasma from forming inside the holes. Cooling water flows through a tube welded to the backside of the showerhead to avoid overheating caused by plasma in contact with the showerhead.

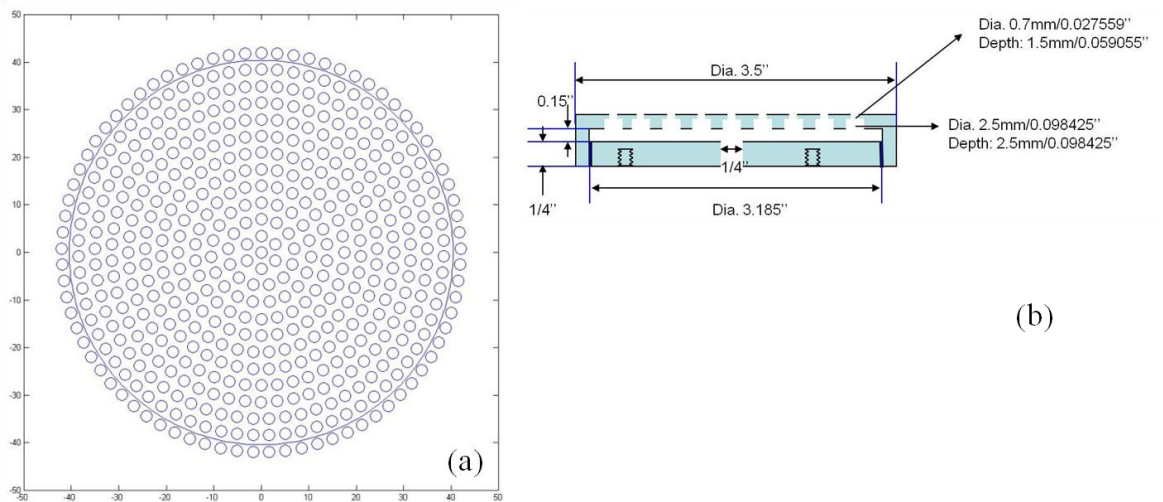


Figure 3.5 Schematic of the showerhead RF powered electrode. (a) Top view of the showerhead, and (b) Side view of the showerhead. The width and height of the hollow space behind the holes were designed to make gas flowthrough the showerhead uniform.

A quartz tube was used to confine the plasma. A narrow gap (2 mm) between the substrate and the edge of the quartz tube provides enough space for gas pumping. In order to confine the plasma between the electrode and the substrate, a multi-pole magnetic arrangement was used. Fourteen NdFeB permanent magnets (~10,000 Gauss) were placed azimuthally outside the quartz tube with alternating poles as shown in Figure 3.6. The magnetic field suppresses the loss of electrons to the radial wall or the escape of electrons through the 2 mm gap.

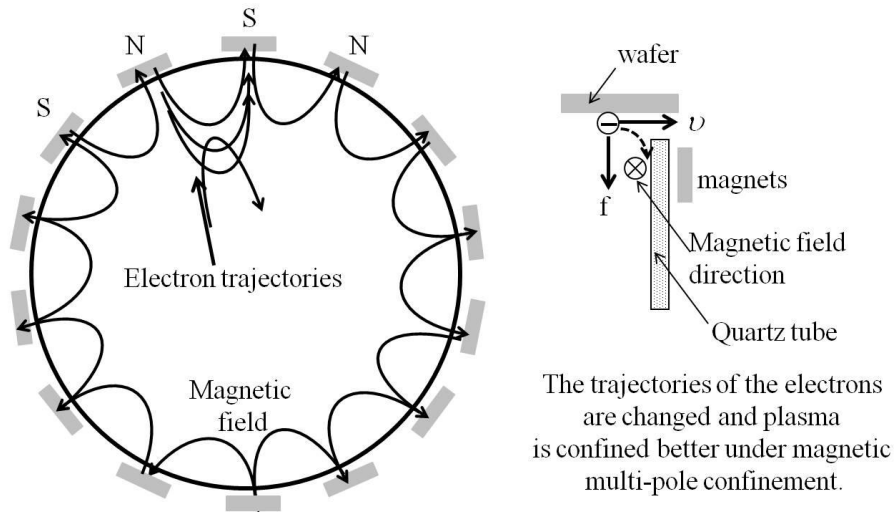


Figure 3.6 Magnetic multi-pole confinement of the plasma.

Within the 4 inch diameter, 2.5 inch long volume between the showerhead and the ceramic plate, the metal parts were all connected to the RF line. As a result, a bright plasma was created between these parts (Figure 3.7a) because of the hollow cathode effect [106]. Under these conditions, most RF power was lost outside the main reactor volume. To solve this problem, the empty space where the parasitic plasma formed was

filled with a conductor. This confined the plasma in the main reactor volume (Figure 3.7b).

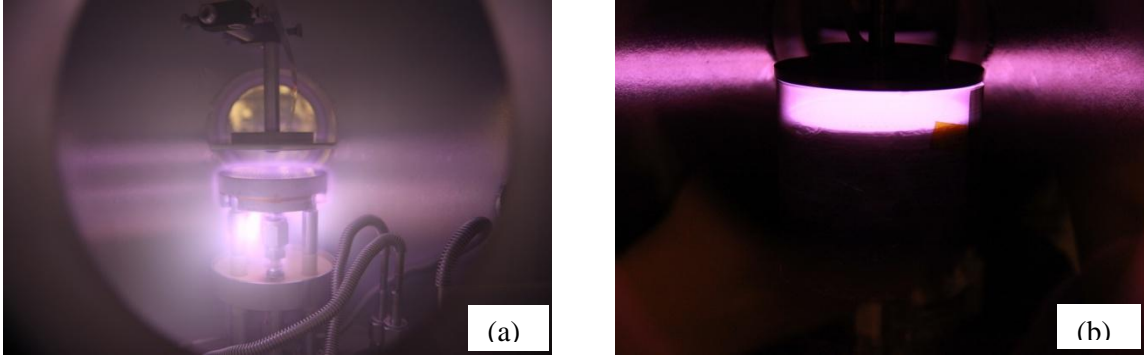


Figure 3.7 (a) Strong parasitic plasma behind the showerhead in-between metal parts. (b) Uniform plasma could be obtained under pressure of 400~1600 mTorr and input power of 5~30 W.

3.2. Inductively Coupled Plasma (ICP) Reactor Design

In order to generate a high density H_2 (or D_2) plasma, an ICP reactor was designed and built, as shown in Figure 3.8. The center of the ICP source was located on the same circle (described by the substrate rotation) as that of the CCP source but on the opposite side of the vacuum chamber. Plasma was ignited by a 3-turn flat spiral water-cooled coil under a 4 inch diameter alumina plate. The plasma was confined by a focus ring with 4 3/8 inch ID. The gap between the alumina plate and the wafer was 20 mm. 29 MHz RF power was supplied by a high frequency function generator (Hewlett Packard model 8656B) and RF power amplifier (ENI model A-300) through an L-type matching network. An aluminum cylinder supports the alumina plate and also provides gas through two 1/4 inch diameter tubes. A water cooling jacket was welded on the inner surface of the

Al cylinder. Gas flows radially inwards in the plasma region through 8 small holes placed symmetrically in the azimuthal direction.

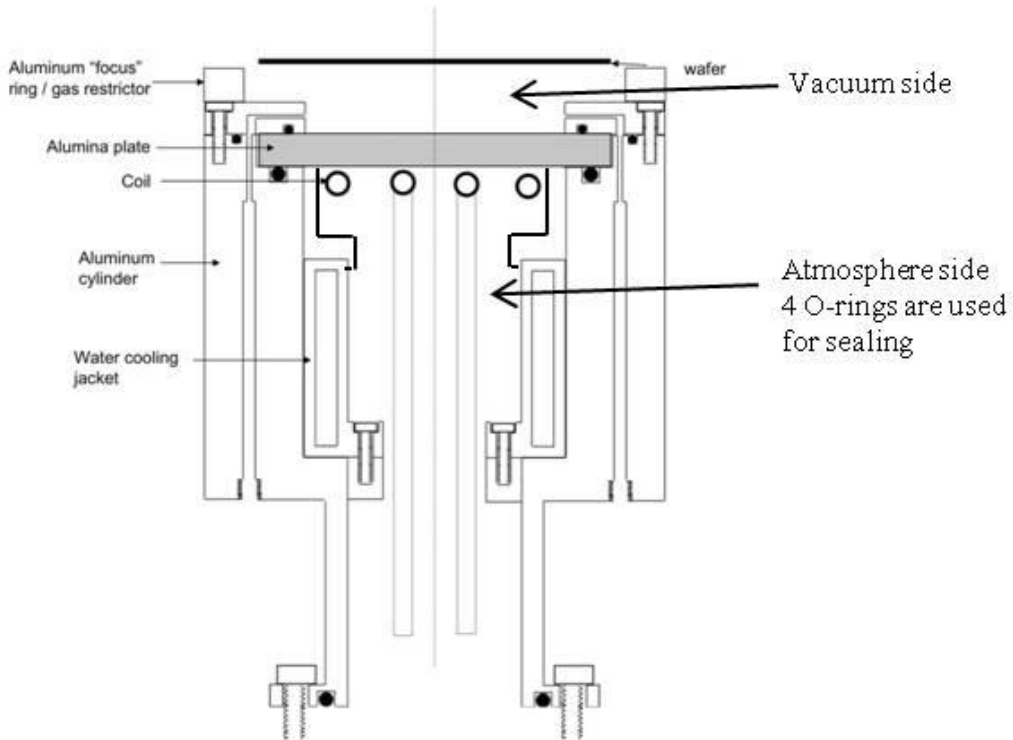


Figure 3.8 Schematic of the ICP reactor.

Figure 3.9 shows a schematic of the gas inlet. Gas flows through the two tubes inside the aluminum cylinder, into a radial channel, and then into the reactor through 8 grooves to provide uniform gas distribution.

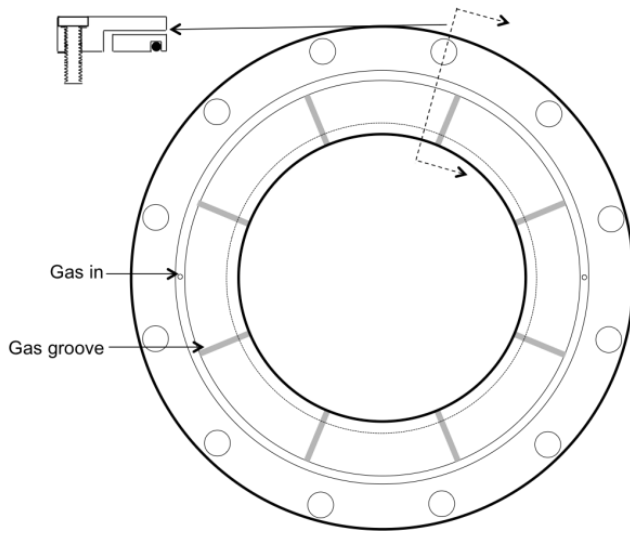


Figure 3.9 Schematic of gas inlet.

Because of the relatively small coil length, the inductance and consequently the RF impedance of the coil was quite low. (impedance Z is given by $Z = i\omega L$ where ω is the RF frequency and L is the inductance.) When using RF power at the standard 13.56 MHz frequency, large RF currents and overheating of the RF feed cables occurred. To alleviate this problem an RF frequency of 29 MHz was used instead, increasing the impedance, and reducing the RF current.

3.3. Heaters and Susceptor

Substrate temperature is an important factor for both deposition and nano-crystallization [107]. Increasing temperature can increase the deposition rate and also enhance nano-crystallization. A heater was installed behind each of the two substrates to vary the substrate temperature (Figure 3.10).

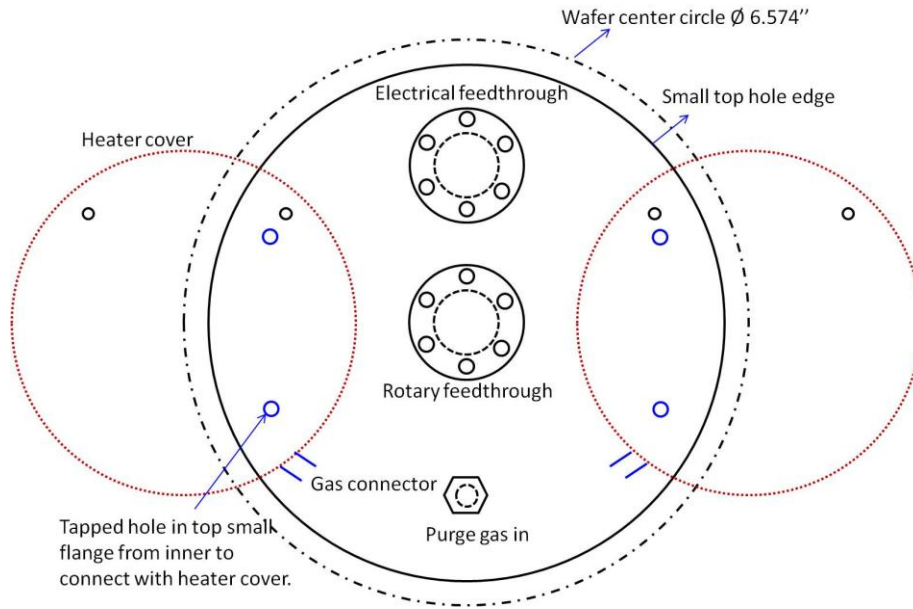


Figure 3.10 Top view of the heater covers and the top flange.

A heater cover was suspended from the top flange of the vacuum chamber with two rods. The center of the two heaters was on the circle of the substrates. To avoid decomposition of the feed gas and deposition on the heater wires, Ar purge gas showers the heater wires. A tantalum foil (Ta has excellent corrosion resistance to most chemicals and high melting point), was bent into a spherical section and used as a heat reflector above the heater wire, as shown in Figure 3.11.

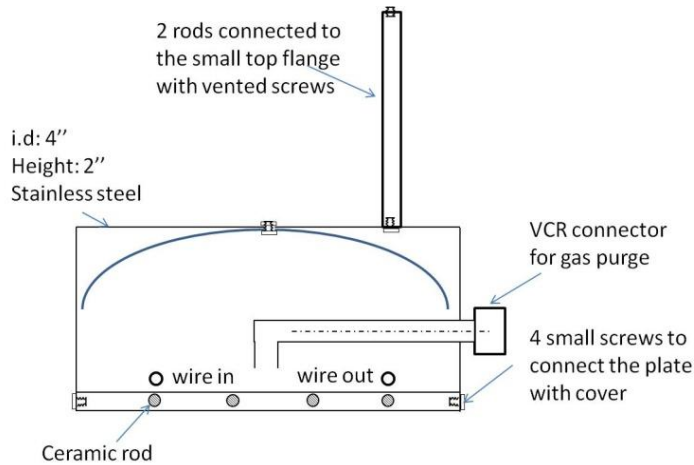


Figure 3.11 Schematic of a heater.

Tungsten wire was used for the heaters. The wires were wrapped around 4 ceramic rods under the arched tantalum roof to provide uniform heating of the substrate. DC voltage was supplied to the wires to obtain the required temperature. A thermocouple was connected to the heater cover to monitor its temperature. During deposition, the substrates were rotated and it was not possible to measure their temperature with an attached thermocouple. Therefore, to determine the temperature of the substrate, calibration experiments were performed in which the substrate was not rotated, but fixed under the heater with a thermocouple attached to the substrate. The gas pressure was set up to be the deposition process pressure. The temperature calibration results are shown in Table 3.1.

Table 3.1 Temperature calibration for Si and SiO₂ substrates.

Si substrate	Substrate temperature (°C)	Cover temperature (°C)	DC Voltage (V)
T calibration	298	305	17
	260	275	14
	200	219	8.98
	99	119.2	4.3
SiO ₂ substrate T calibration	300	230	13
	150	115	5.8
	100	70	4.08

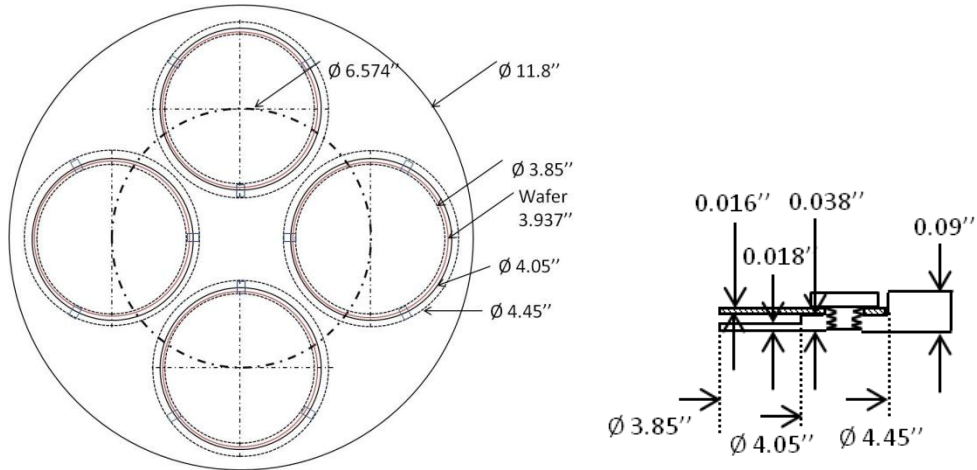


Figure 3.12 Top view of the susceptor and design of the edge of the well where the substrate rests.

Each substrate rested in a well shown schematically in Figure 3.12. Three clamps were used to mount the substrate firmly. The center of the susceptor was connected to a rotary feed-through and a stepping motor (Superior model M061-LF02) that controlled substrate rotation via a computer running a LabView program. The number of process cycles, rotation speed, and residence time of the substrate in each reactor could be set independently via the LabView interface, shown in Figure 3.13. To avoid oscillations when the substrate was rotated into the plasma zone, a ramp speed was implemented so that the substrate entered the plasma region gradually. The susceptor could also be rotated continuously without extra dwelling in each reactor. The fastest rotation speed for the current set-up was 0.5 s per revolution.

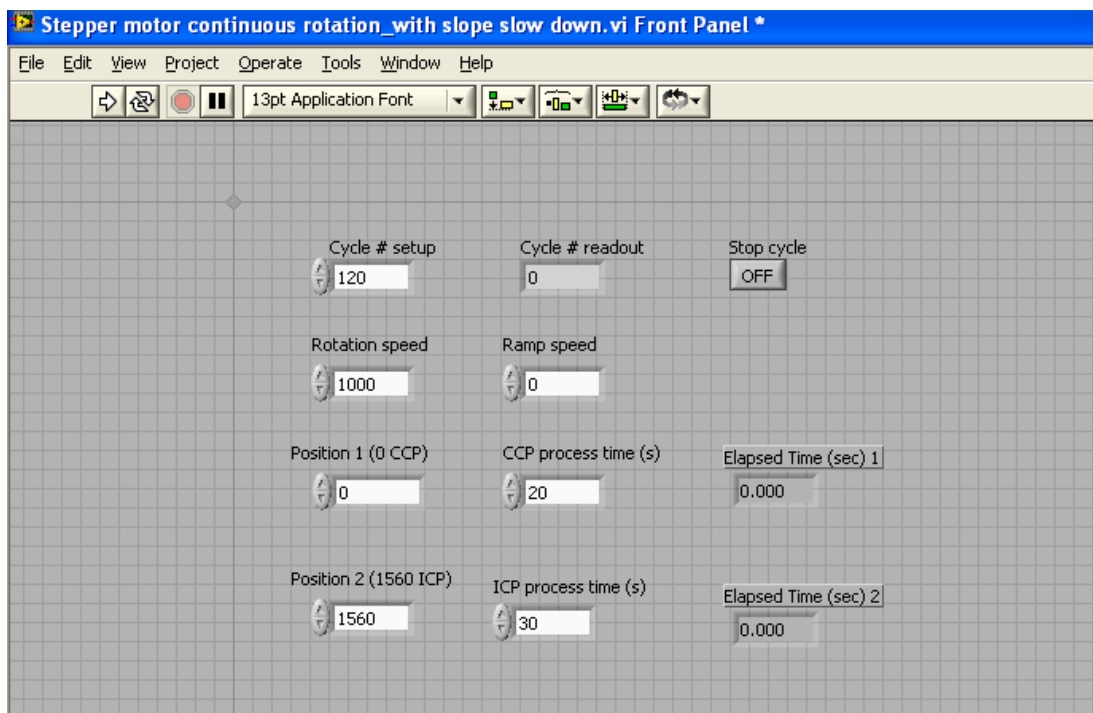


Figure 3.13 Stepping motor control interface.

3.4. Ar Curtain

An Ar “curtain” was designed to block mixing of the gases fed to CCP and ICP.

A schematic of the Ar curtain is shown in Figure 3.14.

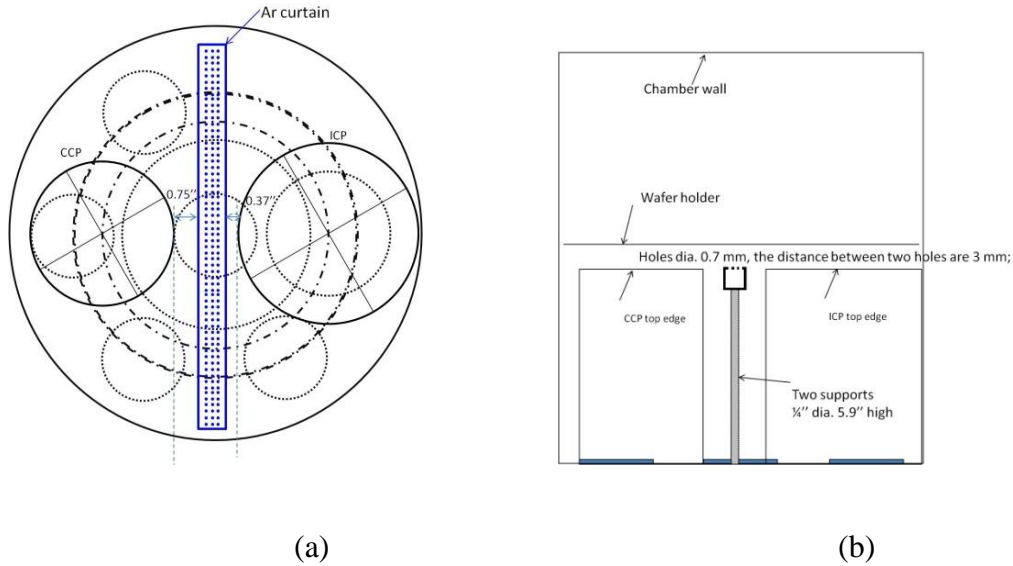


Figure 3.14 The schematic of the Ar curtain (a) top view and (b) side view.

The curtain had a rectangular cross section and it was placed between the CCP and ICP reactors. The top of the curtain was at a plane 1 mm below the top of the two reactors. Ar gas was fed from the bottom and exited the top forming a curtain to suppress mixing of the gases fed to the two reactors. On the top surface of the curtain, there were hundreds of small holes with 0.7 mm diameter and 3 mm distance between hole centers (square pattern arrangement) to form uniform gas flow. The Ar curtain was not used in the experiments reported in this dissertation. Nevertheless, the efficacy of the curtain in preventing gas mixing was evaluated for future experiments.

3.5. Mass Spectrometer Setup

A mass spectrometer (MS) was employed to sample the effluent of the ICP reactor to monitor reaction byproducts during nano-crystallization. The mass spectrometer (UTI 100C) was used in conjunction with a small intermediate chamber for differential pumping. The base pressure in the mass spectrometer chamber was $\sim 1 \times 10^{-8}$ Torr. A turbomolecular (turbo) pump (100 l/s, Edward model RV5) was used to pump the intermediate chamber and another turbo pump (600 l/s, Ebara model ET600WS) was used to evacuate the mass spectrometer chamber. The output of both turbo pumps was connected to a roughing pump. Figure 3.15 shows a schematic of the MS setup. For a typical process pressure of 0.72 Torr, the pressure at the mass spectrometer side was adjusted by the throttle valve between the intermediate chamber and its turbo pump to be 5×10^{-7} Torr. The ICP plasma zone was sampled through a pinhole on the face of a SS disk that blocked the opening of a $\frac{1}{4}$ " diameter SS tubing.

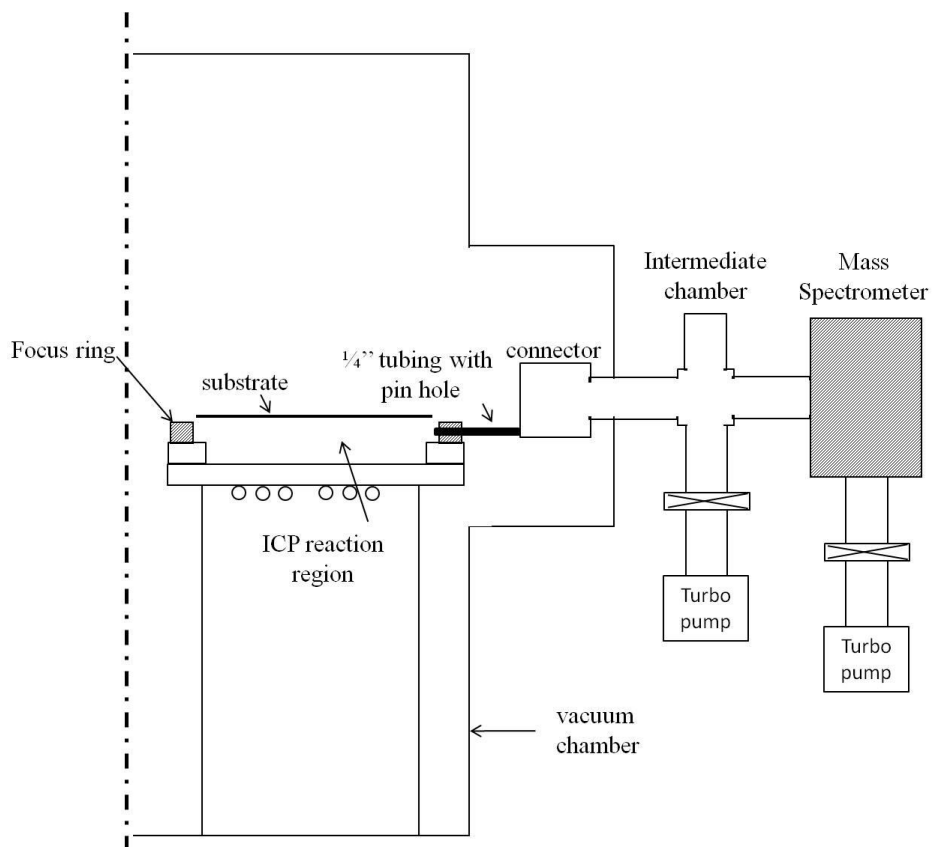


Figure 3.15 Schematic of the mass spectrometer setup.

3.6. Optical Emission Spectroscopy (OES)

OES was used to monitor H_2/D_2 plasmas in the ICP source. A schematic of the OES setup is shown in Figure 3.16. Light from the plasma was imaged at the entrance slit of the spectrometer (Jobin Yvon SPEX series Model TRIAX 550) with an intensified ICCD (ICCD) camera (Princeton Instruments, Model PI-MAX) and controller (ST-133) that could provide high resolution (about 1.5 \AA) spectra. A sampling period of $\sim 100 \text{ ms}$ was used. Cooling water was used for the camera head, which housed the CCP camera and intensifier. The operation mode was always set to “shutter mode,” that was high voltage was applied to the intensifier’s photocathode during the exposure time period, but not during readout of the array. Figure 3.17 shows the main components of the ICCD.

Electrons are accelerated by the high voltage and thus a weak signal can be intensified. D₂ plasma was monitored looking especially for emission from HD, which was the product of D atoms abstracting H from the surface.

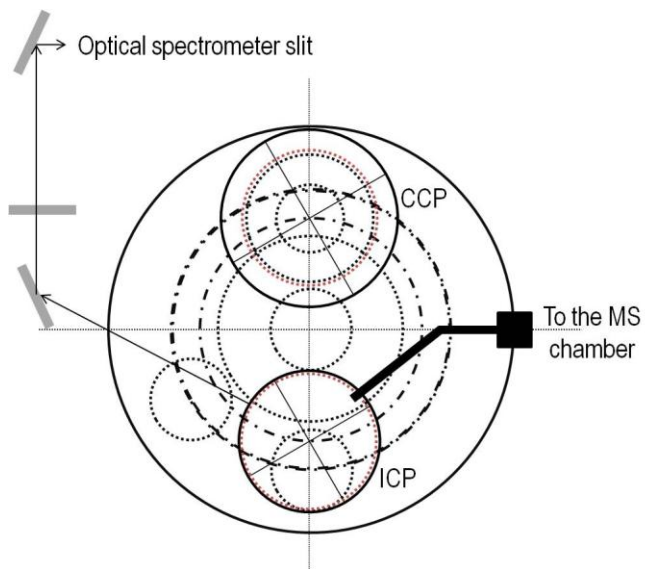


Figure 3.16 Schematic for OES set up to monitor ICP source.

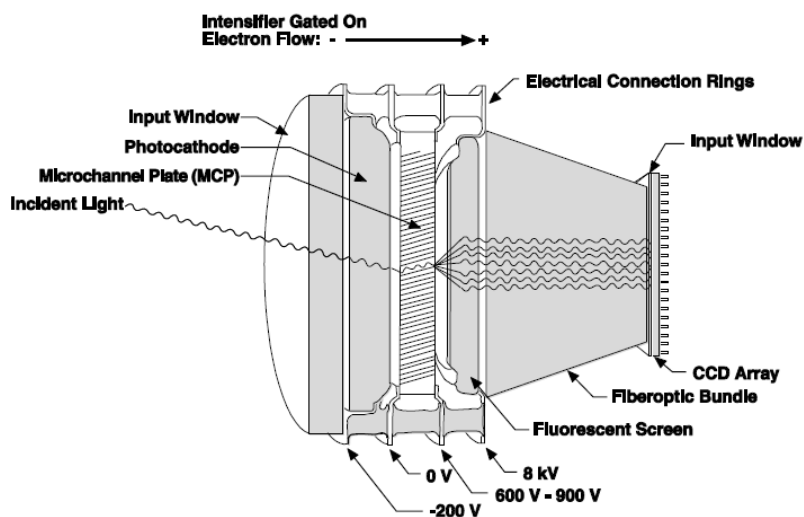


Figure 3.17 Main components of intensified charge coupled device (ICCD).

Chapter 4. Raman Spectroscopy of Layer-by-Layer Processed Films

In this chapter, a layer-by-layer cyclic process for a-Si:H film deposition and nano-crystallization is discussed and film microstructure characterization by Raman spectroscopy is presented.

4.1. Layer-by-Layer Cyclic Process Design

In the present work, a cyclic process was implemented to obtain nano-crystalline Si thin films by repeatedly moving substrates between a capacitively coupled plasma (CCP) for deposition, and an inductively coupled plasma (ICP) for nano-crystallization. Thin a-Si:H layers were deposited in a 1% SiH₄/He CCP and then rotated into a H₂ ICP for nano-crystallization. Different plasma conditions in the CCP were tested to optimize the a-Si:H deposition process, avoiding powder production or non-adherent films. These unwanted results were found under relatively high RF power (30 W) and high SiH₄ flow rate (6 sccm SiH₄ diluted in 594 sccm He, 900 mT) conditions. Optimized CCP and ICP conditions are shown in Table 4.1. Gas was flowing in both plasmas during the cyclic process.

Table 4.1 CCP and ICP operating conditions.

	Gas flow	Pressure (mT)	RF power/frequency	Process time
CCP	SiH ₄ 1% /He 100 sccm H ₂ 40 sccm	710	27 W/13.56 MHz	t_1 per cycle
ICP	H ₂ 80 sccm	710	170 W/29 MHz	t_2 per cycle

To avoid possible interference from crystalline Si, glass cover slips (Schott D263M) were used as substrates for Raman spectroscopy. Figure 4.1 shows the Raman spectrum of a glass substrate.

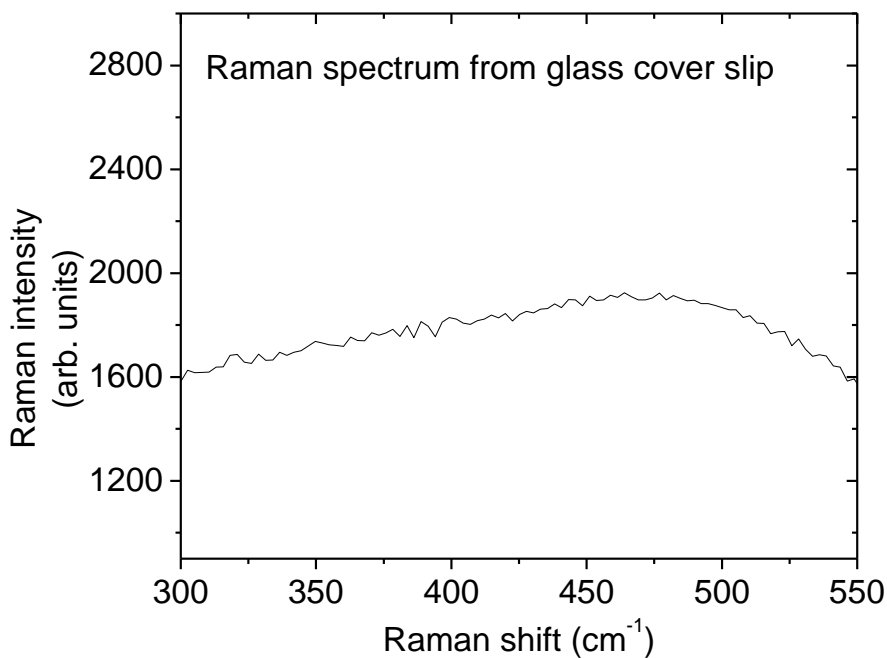


Figure 4.1 Raman spectrum of a glass cover slip substrate.

The crystalline volume fraction of the films was derived from features between 400 and 550 cm^{-1} in Raman spectra. Fortunately, the intensity of the Raman spectrum of the substrate is nearly constant over this range. Therefore, no corrections were made for substrate contribution in estimating crystalline volume fractions.

One inch diam. glass cover slips were clamped at the center of a 4" diam. Al disc substrate holder, having a 1" diam. opening in the middle. The substrate holder was fixed

in the well of the rotating susceptor with three clamps. Substrates were heated to 250 °C for about 30 min. before the start of the process, and were kept at that temperature for the duration of the process. Substrates were rotated repeatedly between the CCP and ICP reactors. During each cycle, a substrate was stopped in the CCP plasma for a-Si:H deposition for time t_1 , and then rotated into the ICP discharge for nano-crystallization for time t_2 . This was repeated for n_c number of cycles. Both plasmas were ON for the duration of the process. Three main groups of experiments were performed to study nano-crystallization with different ICP process times and 1, 10 or 120 cycles. In addition, 480 cycles with $t_2/t_1 = 5$ s/5 s, and continuous rotation was investigated. 19 different conditions, as shown in Table 4.2, were studied with the fixed plasma conditions listed in Table 4.1.

Table 4.2 The 19 conditions with various CCP and ICP process times and cycle numbers used in the layer-by-layer cyclic process.

Sample #	t_1 (minute)	t_2 (minute)	t_2/t_1	n_c	Sample #	t_1 (minute)	t_2 (minute)	t_2/t_1	n_c
s55/s87	40	0	-	1	s74	1/3	1/12	0.25	120
s65	40	10	0.25		s75	1/3	1/6	0.5	
s66	40	20	0.5		s73	1/3	1/4	0.75	
s70	40	30	0.75		s76/s97	1/3	1/2	1.5	
s69/s86	40	60	1.5		s76_2	½	1/3	0.67	
s68	4	1	0.25	10	s73_2	¼	1/3	1.33	480
s67	4	2	0.5		s75_2	1/6	1/3	2	
s56	4	3	0.75		s74_2	1/20	1/3	4	
s58	4	6	1.5		s95	1/12	1/12	1	
					s93	Continuous rotation for 121 min. with 4500 turns			

4.2. Raman Spectroscopy Results

Raman spectroscopy was used to evaluate the crystalline volume fraction of the films. All Raman spectra were taken from the center of the samples. For samples s55 to s76 of Table 4.2, the total CCP deposition time was 40 min. and the film thicknesses were similar (as found by spectroscopic ellipsometry, see below). Sample s55 was subjected to deposition only (no nano-crystallization). The Raman spectrum of this sample (Figure 4.2) shows only the amorphous peak located at 479 cm^{-1} with 69 cm^{-1} FWHM.

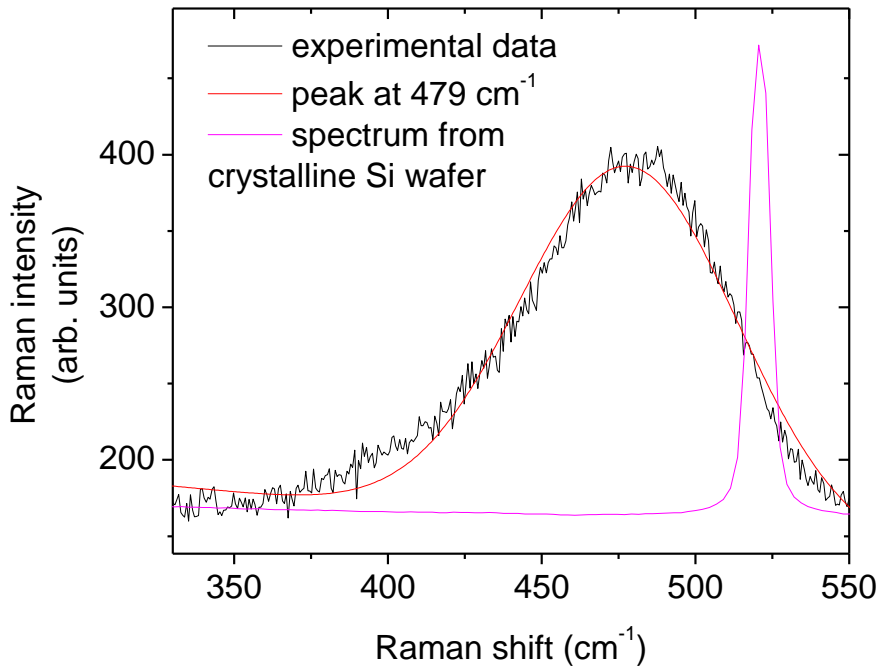


Figure 4.2 Raman spectrum of sample s55 subjected only to CCP a-Si:H deposition. The spectrum was deconvoluted into one Gaussian peak at 479 cm^{-1} with 69 cm^{-1} FWHM. The Raman spectrum from single crystalline Si is also shown for reference (peak at 520 cm^{-1} with 7 cm^{-1} FWHM).

For the rest of the samples, after CCP deposition of a-Si:H, the substrate was rotated into the hydrogen ICP for nano-crystallization. The Raman spectrum of sample s69 (1 cycle, 40 min. CCP deposition followed by 60 min. hydrogen ICP crystallization) shows extra peaks at 503 cm^{-1} and 520 cm^{-1} (Figure 4.3), suggesting the presence of small grain crystallites mixed in the amorphous phase.

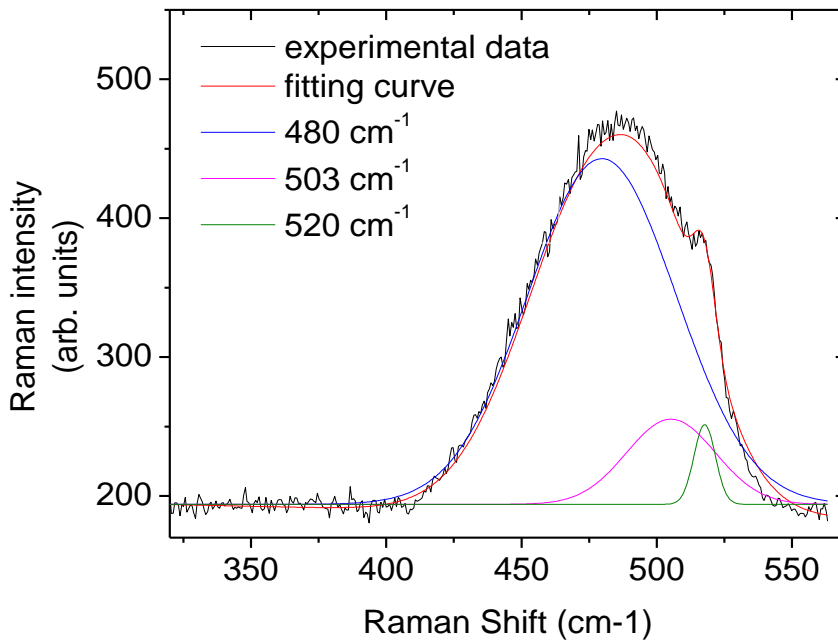
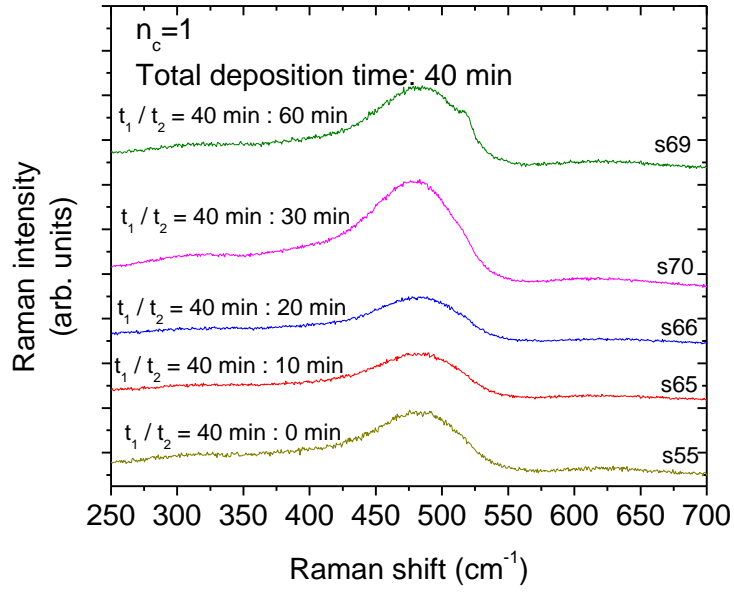
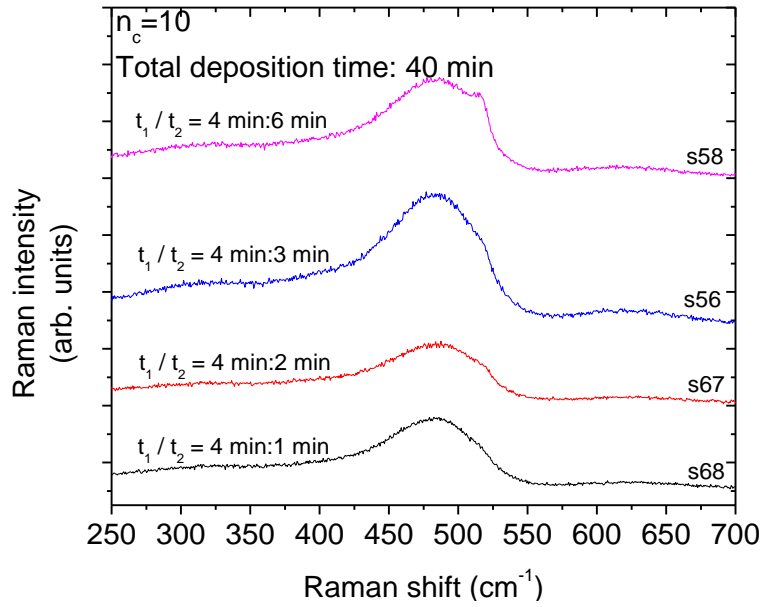


Figure 4.3 Raman spectrum of sample s69 subjected to 40 min. CCP a-Si:H deposition and then 60 min. ICP nano-crystallization (one cycle). The spectrum was deconvoluted into three Gaussian peaks at 480 cm^{-1} (64 cm^{-1} FWHM), 503 cm^{-1} (42 cm^{-1} FWHM) and 520 cm^{-1} (10 cm^{-1} FWHM).

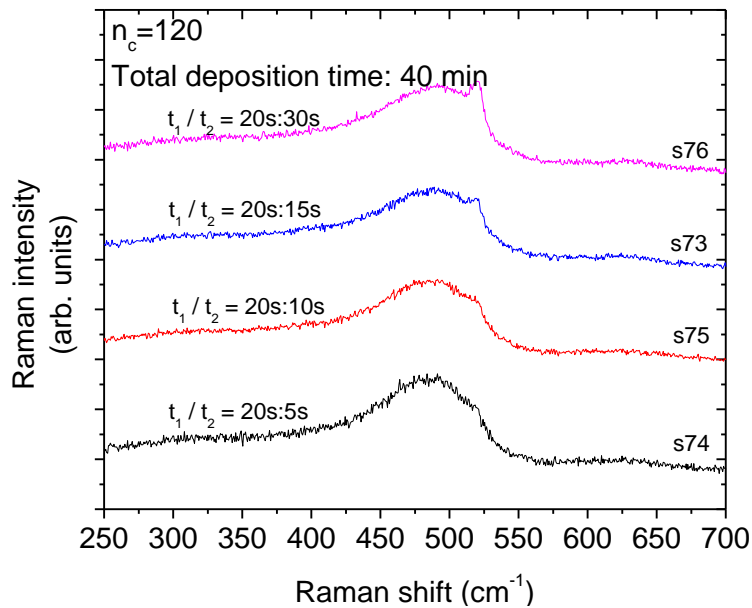
The number of cycles was then varied (1, 10 or 120 cycles) keeping the *total* (overall cycles) deposition time constant, for different nano-crystallization times (giving different film thicknesses). The corresponding Raman spectra (for a total of 13 samples) are shown in Figure 4.4.



(a)



(b)



(c)

Figure 4.4 Raman spectra of films deposited at a substrate temperature of 250°C with the same *total* deposition time of 40 min., and variable ratio of deposition time to nano-crystallization time t_1/t_2 , as well as variable number of cycles, $n_c = 1$ in (a), $n_c = 10$ in (b) and $n_c = 120$ in (c).

Figure 4.4 (a) shows Raman spectra for 1 cycle with $t_1=40$ min. deposition in the CCP, followed immediately by exposure to the H₂ ICP for times t_2 of 0, 10, 20, 30 and 60 min. The spectra indicate that the films contain mostly amorphous Si, except when the H₂ ICP exposure time was 60 min. ($t_1:t_2 = 4:6$), for which a small peak at 520 cm⁻¹ s indicated the conversion of a small fraction of the material to nano-crystalline Si.

When the number of cycles was increased to 10 and the deposition time per cycle was correspondingly reduced to 4 min., formation of nano-crystallites occurred at $t_1:t_2 = 4:3$ (Figure 4.4 b). Finally with 120 cycles and a deposition time per cycle of 20 s, nano-crystallites were formed at $t_1:t_2 = 4:1$ (Figure 4.4 c). Thus, the thinner the a-Si:H layer

was, the less exposure time in the hydrogen ICP was needed to induce nano-crystallization.

To evaluate the crystalline volume fraction in the film, the three-peak fit was used to deconvolute the spectra into components due to amorphous Si (480 cm^{-1}), small nano-crystalline particles ($500 \sim 510\text{ cm}^{-1}$) and larger crystalline domains (520 cm^{-1}). Figure 4.5 shows an example of this peak fitting.

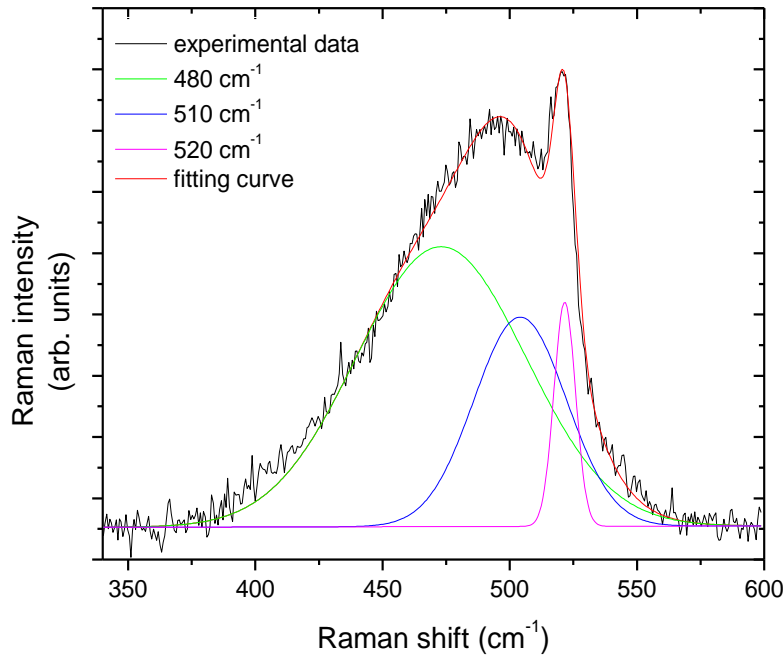


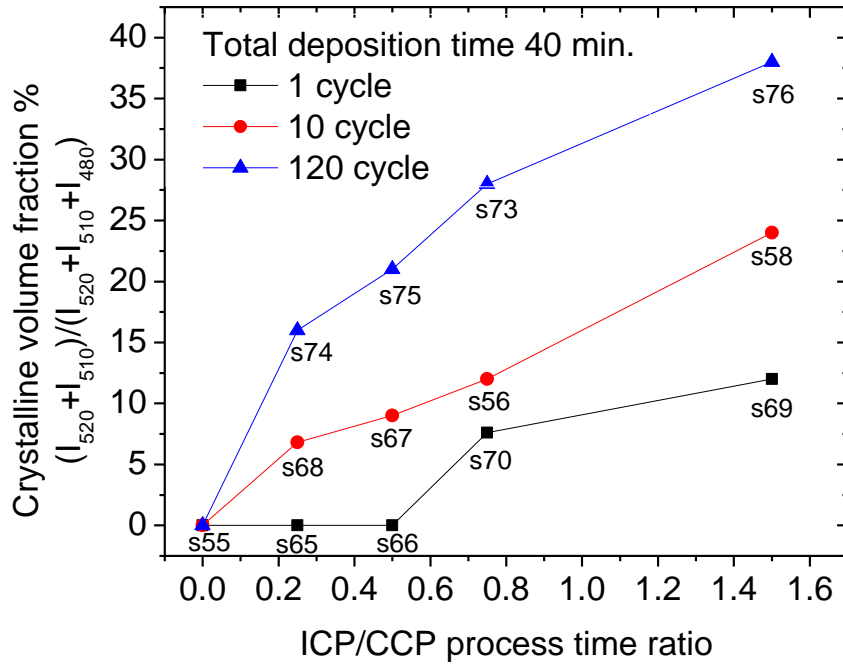
Figure 4.5 Raman spectrum for sample s76, along with the fit (red line) obtained from a Gaussian three-peak deconvolution.

The three-peak deconvolution for all 19 conditions (21 samples) is given in Appendix A. Figure 4.6 (a) shows the crystalline volume fraction X_c obtained by considering the contribution from small sized nano-crystallites (510 cm^{-1} peak) as well as

larger size crystallites (520 cm^{-1}) using the three-peak method (using $\frac{I_{510} + I_{520}}{I_{480} + I_{510} + I_{520}}$, see

Eq. 2.5), while Figure 4.6 (b) shows X_c by considering the larger size crystallites only, i.e.,

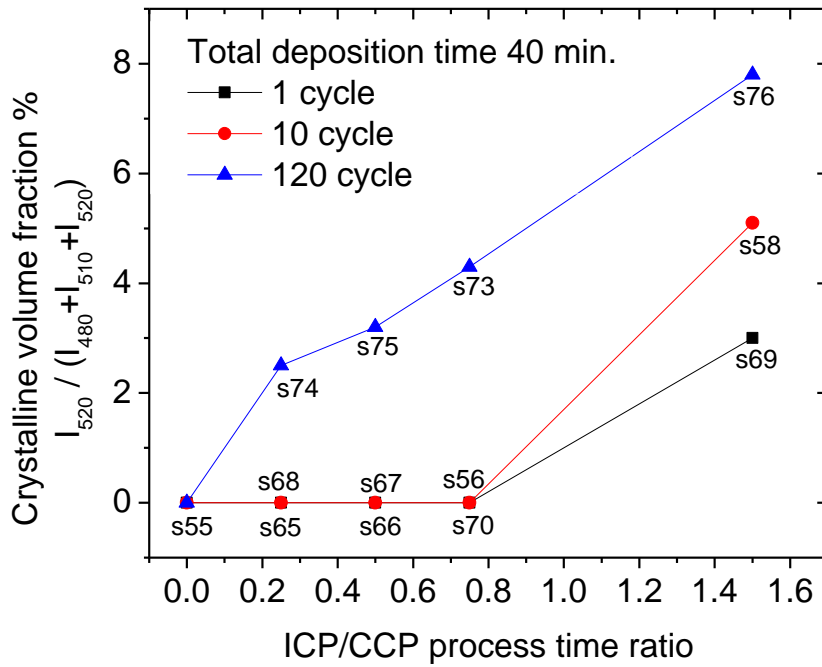
by using the ratio $\frac{I_{520}}{I_{480} + I_{510} + I_{520}}$.



(a)

Figure 4.6 Crystalline volume fraction as a function of the ratio of H_2 ICP nano-crystallization time to CCP deposition time and number of process cycles, (a) using the

three-peak method $\frac{I_{510} + I_{520}}{I_{480} + I_{510} + I_{520}}$.



(b)

Figure 4.6 Crystalline volume fraction as a function of the ratio of H₂ ICP nano-crystallization time to CCP deposition time and number of process cycles, (b) using the

two-peak method $\frac{I_{520}}{I_{480} + I_{510} + I_{520}}$.

The lower values of X_c in Figure 4.6 (b) compared to those in Figure 4.6 (a) indicate that most of the crystalline regions were composed of small grain nano-particles. The shift in the Raman peak near 480 cm⁻¹ (before deconvolution) plotted in Figure 4.7, can be used to estimate the crystallite size [87-89], since this peak includes the contribution from small grain size crystallites.

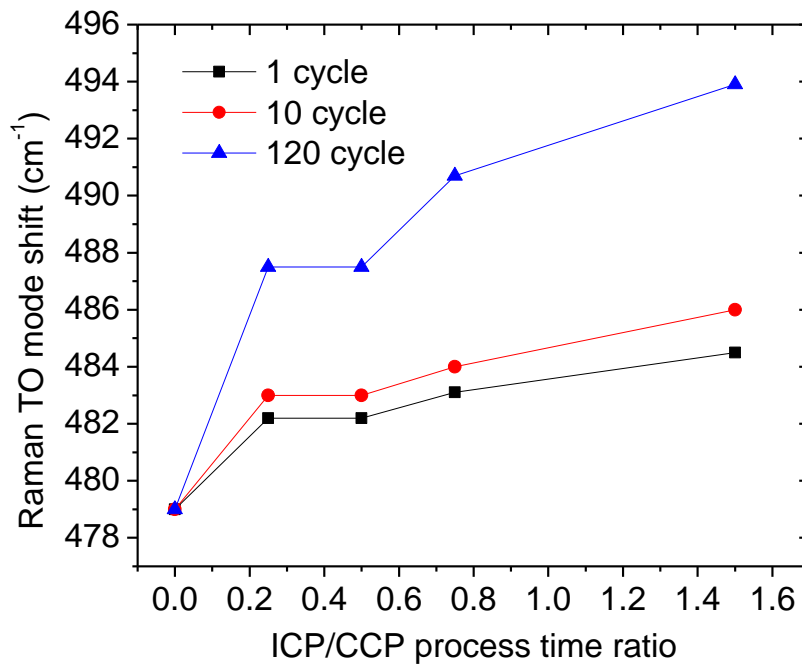


Figure 4.7 The ~ 480 cm^{-1} Raman peak position as a function of ICP exposure time and number of cycles.

The shift towards higher wavenumbers indicates that larger crystallites are formed in the film with increasing ICP process time and number of cycles. This trend was more apparent when the cycle number was increased (more cycles resulted in thinner film per cycle). Based on Figure 2.13 (b) of Chapter 2, the corresponding nano-crystallite size is plotted in Figure 4.8.

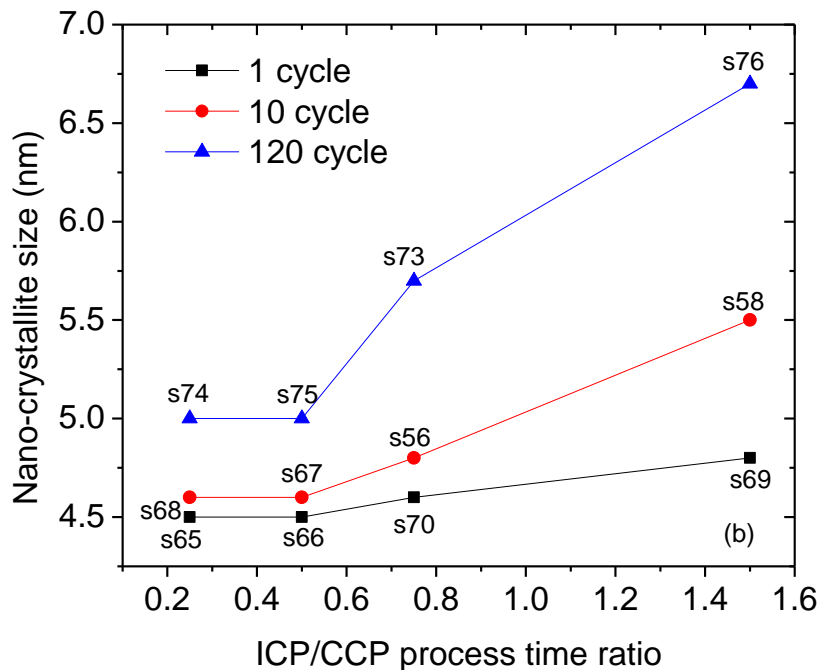


Figure 4.8 Nano-crystallite size with different ICP/CCP process time ratios for 12 samples from s56 to s76. Crystallite size increases with ICP process time and cycle number. With 120 cycles and ICP/CCP process time ratio 1.5 the largest crystallites (6.7 nm) were found in s76.

Figure 4.8 suggests the presence of small size grains in the samples exposed to the H₂ ICP for a short time, especially for the 1 and 10 cycle experiments. Such small grains are not accounted for in the two-peak deconvolution method. However, these small size grains were included as “crystalline” material in the 3-peak method. Therefore this method was used to determine the crystalline fraction in the films.

The average deposition rate measured by UV-VIS absorption was about 14 Å/min. Therefore, for the 40 min. total deposition time, the deposited layer per cycle was 560 Å, 56 Å and 4.67 Å for 1, 10 and 120 cycles, respectively. For the thickest deposition layer,

even a 60 min. H₂ ICP exposure resulted in only 12% nano-crystalline Si. However, when only 4.67 Å was deposited per cycle, the same 60 min. total H₂ ICP exposure produced a crystalline volume fraction of 38%.

Raman spectra for samples with 120 cycles (s74, s75, s73 and s76) show high crystalline volume fraction and relatively large crystallites compared with the samples with fewer numbers of cycles. To achieve a higher crystalline volume fraction, larger ratios of ICP to CCP exposure times were used for s74_2 (ICP/CCP process time ratio, $t_2/t_1=4$) and s75_2 (ICP/CCP process time ratio, $t_2/t_1=2$). Raman spectra for samples with various t_2/t_1 time ratios, each subjected to 120 cycles are shown in Figure 4.9.

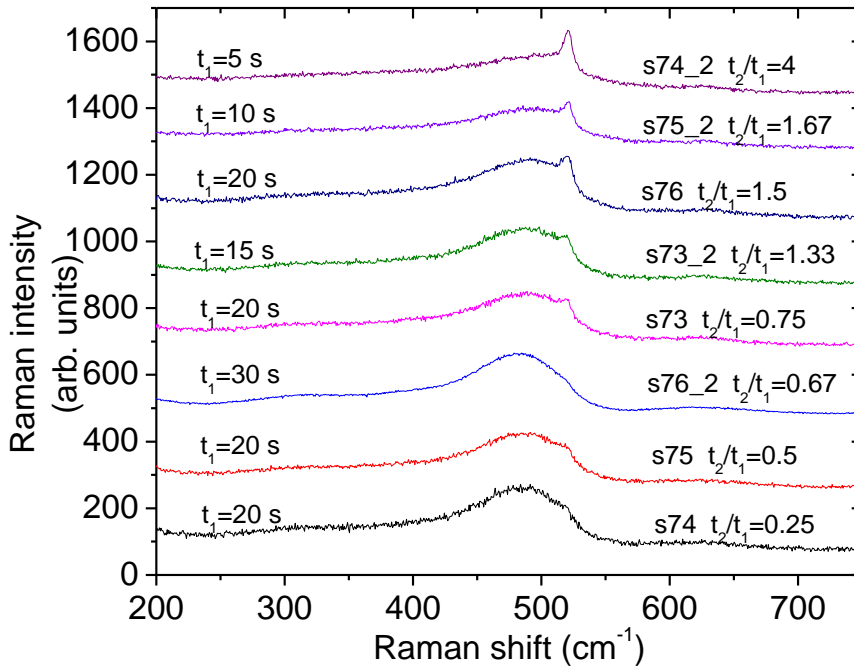


Figure 4.9 Stacked Raman spectra for samples with various ICP/CCP process time ratios, each subjected to 120 cycles.

Figure 4.9 shows that higher t_2/t_1 ratios result in higher crystalline peak intensities at 520 cm^{-1} except for sample s76_2, for which $t_2/t_1 = 0.67$ was a bit larger than that of sample s75 ($t_2/t_1 = 0.5$), but the corresponding crystalline peak was lower than that of s75. This was because the CCP deposition time t_1 for s76_2 was 1.5 times as long as that for s75. For two films with the same or comparable t_2/t_1 , the thicker film has a smaller fraction of crystalline material. This agrees with the data of Figure 4.6, where thicker films required longer H_2 ICP exposure time to achieve the same volume fraction of crystallites. For sample s74_2, corresponding to a short CCP deposition time (5 s) and long H_2 ICP exposure time (20 s) per cycle, the crystalline volume fraction was 72%.

To further compare the effect of H_2 ICP exposure time on the crystalline fraction of films with short CCP deposition time, two more experiments (points s74_2 and s95) were performed with 0.08 min. per cycle deposition in the CCP, and 0.32 min. and 0.08 min. H_2 exposure in the ICP. Figure 4.10 shows these additional points, along with the data of Figure 4.6(a). For the very short CCP deposition time of $t_1 = 0.08$ min., the crystalline volume fraction was higher (for both $t_2/t_1 = 1$ and 4) than that of samples with longer CCP deposition time.

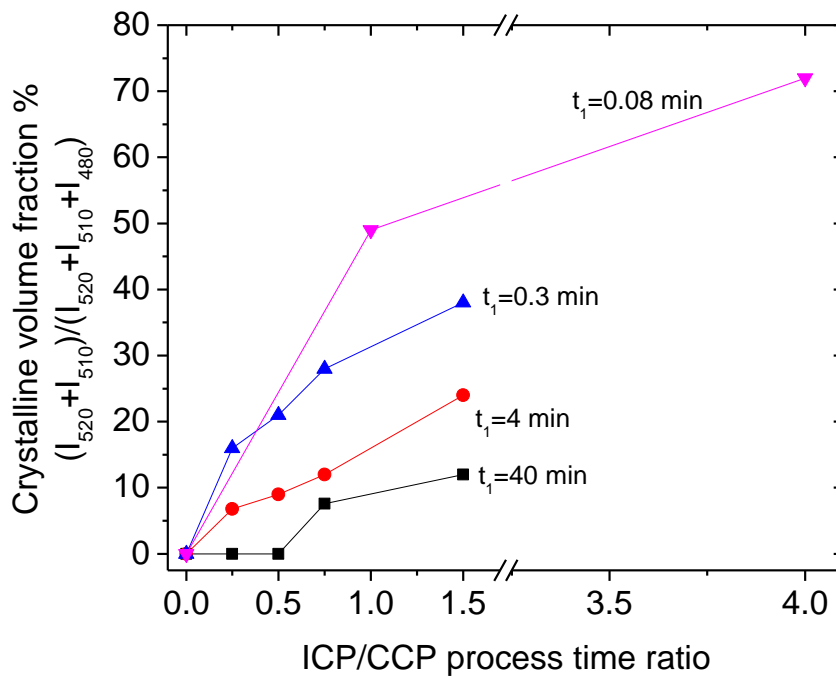


Figure 4.10 Crystalline volume fraction for different CCP deposition times t_1 (0.08 min., 0.3 min., 4 min. and 40 min.) and t_2/t_1 (0, 0.25, 0.5, 0.75, 1, 1.5 and 4).

The film exposure time per cycle to the deposition plasma was further decreased by continuously rotating the susceptor at a rate of 0.625 cycles/s. In this experiment, the substrate made 4500 turns in 120 min. The Raman spectrum of this sample (s93) processed with continuous rotation is shown in Figure 4.11, where it is compared with sample s95, exposed to a 5 s deposition in the CCP and a 5 s crystallization in the ICP.

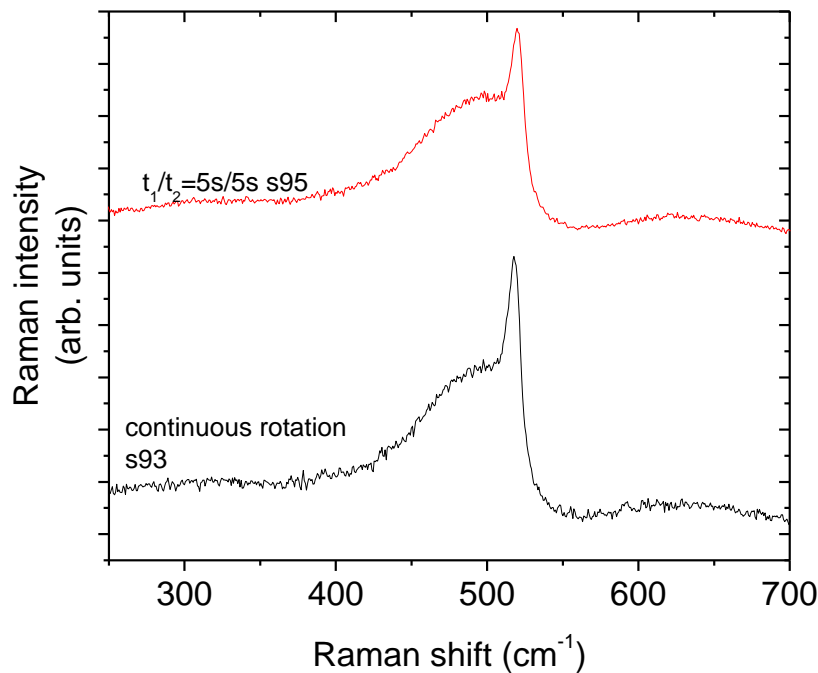


Figure 4.11 Raman spectra of a layer-by-layer processed sample (s95, $t_1:t_2 = 5s/5s$, 480 cycles) and a sample (s93) processed by continuous rotation of the susceptor.

The two samples had comparable crystalline volume fractions (51% for s93 and 49% for s95). For sample s93, the exposure time per cycle was around 0.4 s, which is shorter than the time it takes to deposit one monolayer. Substrate temperature also influences the crystallization process. A lower substrate temperature yields lower crystalline volume fraction [24, 76, 82]. For continuous processing (sample s93), from the geometry of Figure 4.12, the substrate was under the heaters $\sim 100(72+108)/360\%$ or 50% of the time. However, layer-by-layer processed samples spent more than 92% of the time under the heaters. With the same heating power, but shorter time under the heaters, the substrate temperature of sample s93 was therefore lower than that of sample s95, the latter being near 250 °C. The similar crystalline fractions in these two experiments is

therefore attributed to the compensating effect of shorter cycle times (causes an increase in crystal fraction) and the lower average substrate temperature (causes a decrease in crystal fraction) of the continuously-rotated sample.

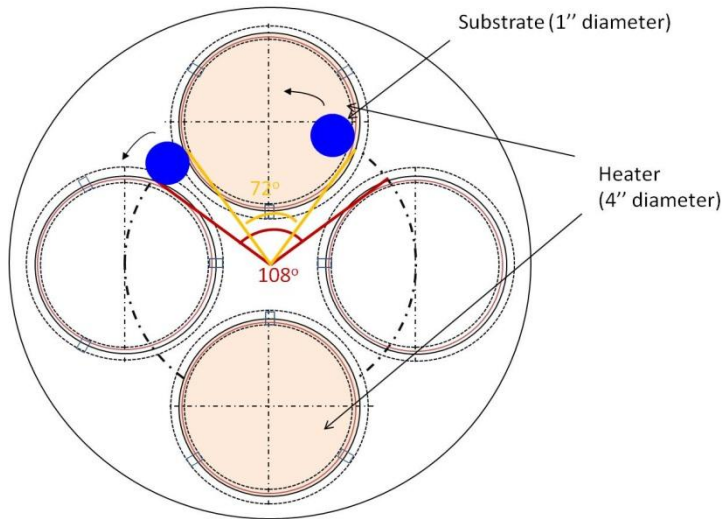


Figure 4.12 Schematic of the geometry of the substrate and the two heaters. During continuous rotation, the substrate was underneath the heaters for $\frac{108^\circ/2+72^\circ/2}{360^\circ} \times 2=50\%$ of the time.

Three experiments were repeated with conditions that led to no crystallinity (s55), small grains (s69, Raman peak at 510 cm^{-1}) and large grains (s76, Raman peak at 520 cm^{-1}). The Raman spectra for these comparisons are given in Figure 4.13.

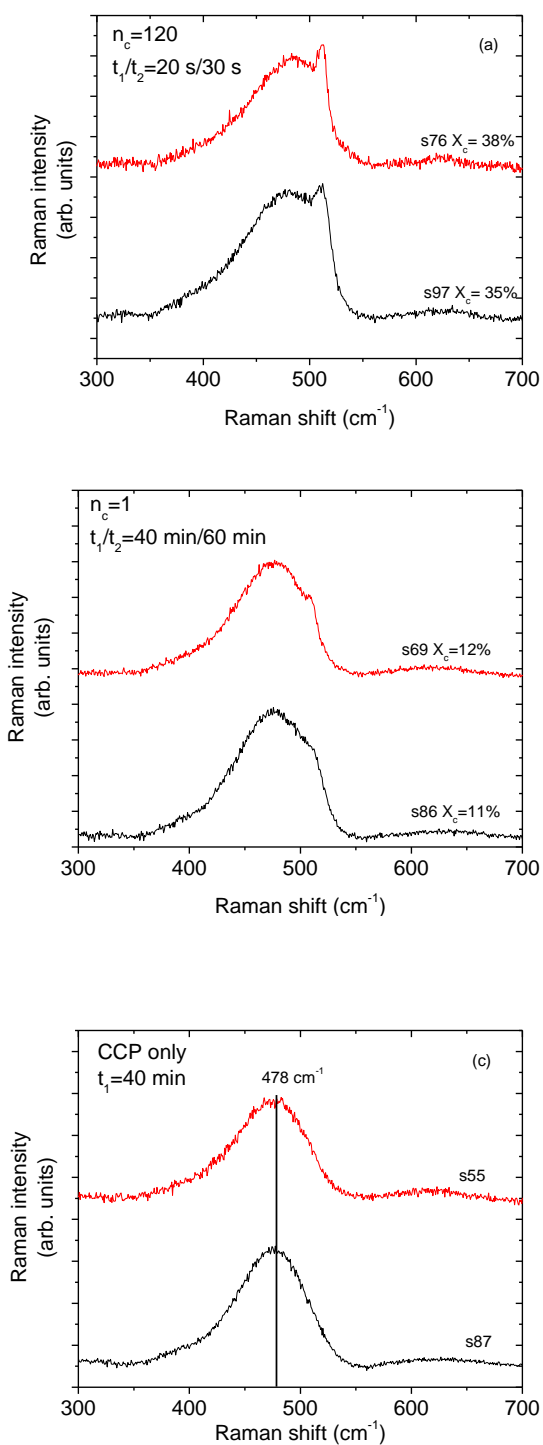


Figure 4.13 Raman spectra of sample s76 and s97 in (a) with 120 cycles and $t_1/t_2=20\text{ s}/30\text{ s}$, the difference of crystalline fraction is within 8%; s69 and s86 in (b) with 1 cycle and $t_1/t_2=40\text{ min}/60\text{ min}$, the difference of crystalline fraction is within 8.3%; and s55 and s87 in (c) with only CCP deposition, they all show the amorphous-like Raman peak.

Chapter 5. Infrared Absorption of Layer-by-Layer Processed Films

Layer-by-layer deposited films were analyzed by Fourier Transform Infrared (FTIR) absorption to evaluate the SiH_x and hydrogen content of the films. Due to the opacity of glass in the IR, Si substrates were used in these experiments. In particular, two sets of experiments were performed to study the variation of the Si-H/Si-D bonds after hydrogen or deuterium plasma exposure.

5.1. IR Analysis of Films after Hydrogen nano-crystallization

Three cyclic process conditions were selected (from Table 4.2) and Si substrates were used to grow films, for IR analysis, at 250 °C substrate temperature. IR transmission spectra in the SiH and SiH_2 stretching vibration wavenumber range are shown in Figure 5.1.

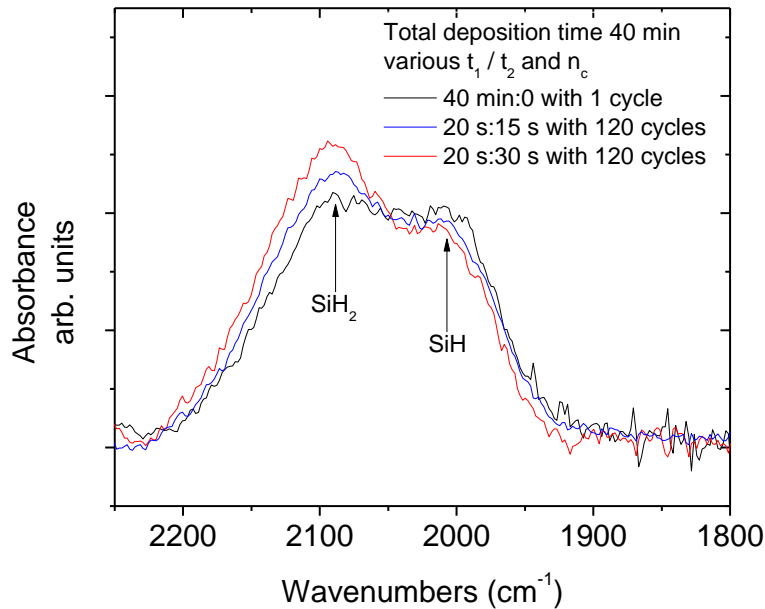


Figure 5.1 Infrared spectra of films with 40 min. total deposition time, and H_2 ICP process times of 0 s for 1 cycle (condition as for sample s55), 30 min. total for 120 cycles (s73), and 60 min. total for 120 cycles (s76).

According to the assignment of the IR spectra in Table 2.1, the absorption peak at 2000 cm^{-1} was attributed to the isolated SiH bonds and the peak at $2090 \sim 2100\text{ cm}^{-1}$ was attributed to clustered $(\text{SiH}_2)_n$ bonds. In Figure 5.1, the absorption peaks at 2000 cm^{-1} and 2100 cm^{-1} are found for all three conditions (s55, s73 and s76 in Table 4.2, 40 min. CCP deposition only, $t_1:t_2=20\text{ s}:15\text{ s}$ with 120 cycles and $t_1:t_2=20\text{ s}:30\text{ s}$ with 120 cycles, respectively). For the same 40 min. total deposition time, longer H_2 ICP exposure results in higher $(\text{SiH}_2)_n$ and lower SiH absorption intensities. Detailed peak fitting for these three samples can be found in Appendix B. Figure 5.2 shows the ratio of the integrated $2090\text{-}2100\text{ cm}^{-1}$ peak to the sum of the integrated intensities of the $2090\text{-}2100\text{ cm}^{-1}$ and 2000 cm^{-1} peaks. The corresponding crystalline volume fraction determined from Raman spectroscopy for these samples is also shown. The increase in SiH_2 relative to SiH bonds correlates with the increase of the crystalline volume fraction in the films, as H_2 ICP exposure time was increased.

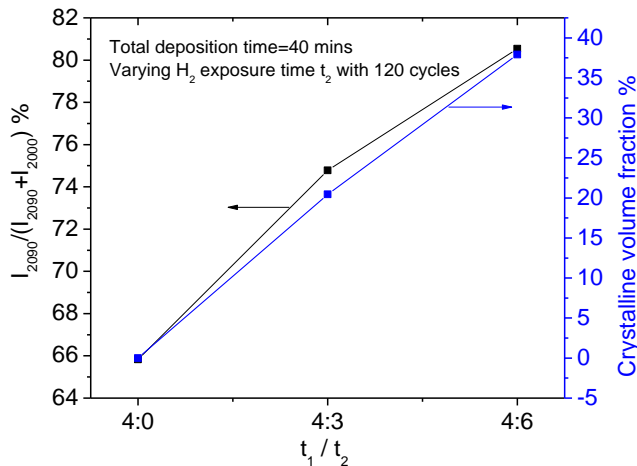


Figure 5.2 Integrated FTIR intensity of the $2090\text{-}2100\text{ cm}^{-1}$ peak (SiH) divided by the sum of integrated intensities of the $2090\text{-}2100\text{ cm}^{-1}$ and 2000 cm^{-1} (SiH_2) peaks vs. CCP/ICP exposure time ratio. The crystalline volume fraction in the films, as measured by Raman spectroscopy, is also shown.

The wagging/rocking mode of hydrogen bonded in SiH, SiH₂, clustered (SiH₂)_n, and SiH₃ displays an absorption peak around 640 cm⁻¹ [8, 38, 91]. The integrated intensity of that peak was used to estimate the hydrogen content. The hydrogen absorption coefficient is obtained according to Eq. 5.1,

$$\alpha(\omega) = \frac{1}{d} [\ln(XR) - \ln(\sqrt{1+X^2} - 1)], \quad (5.1)$$

where d is the film thickness and $R=0.3$ is the reflectivity of silicon [91]. X is found from Eq. 5.2,

$$X = 2R(T/T_b)/(1 - R^2), \quad (5.2)$$

where T is the transmittance of the sample and T_b is the transmittance of the substrate [90]. Eq. 2.11 ($I_{640} = \int_{-\infty}^{+\infty} \alpha_{640}(\omega) d\omega/\omega$) and Eq. 2.12 ($[H] = A_{640} I_{640}$) were used to calculate the integral of the absorption coefficient to obtain the hydrogen amount in the film. By assuming the deposited film density was the same as that of crystalline silicon [96], i.e., an atomic density of $5 \times 10^{22} \text{ cm}^{-3}$, the hydrogen concentration was estimated and is shown in Figure 5.3. With 40 min. CCP deposition and 120 cycles, the hydrogen concentration dropped from 13% at $t_1:t_2=4:0$ to 10.5% at $t_1:t_2=4:6$.

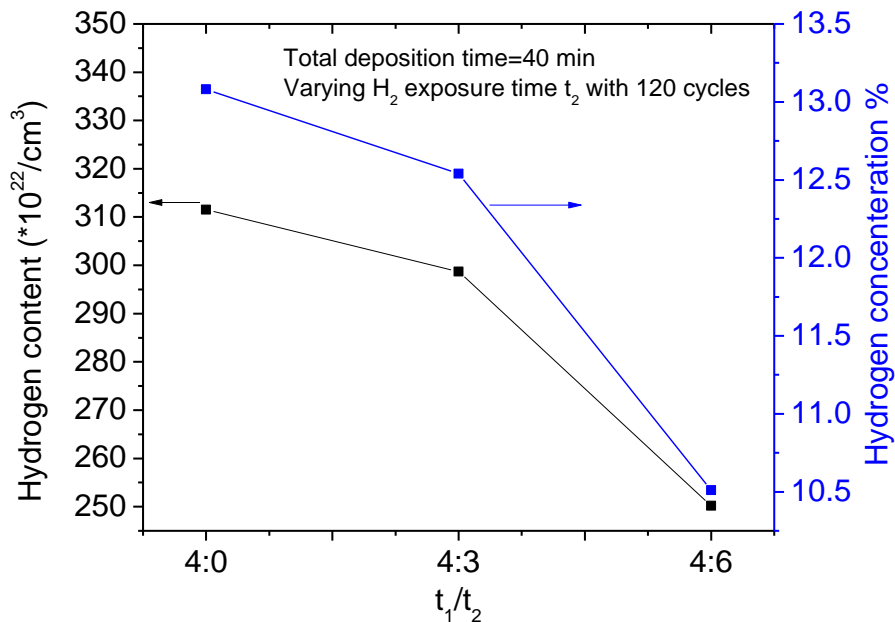


Figure 5.3 Hydrogen content and % hydrogen concentration as a function of ICP exposure time t_2 . Other conditions were 120 cycles and a total deposition time of 40 min. Hydrogen concentration decreases from 13% to 10.5% with increasing t_2 .

5.2. IR Analysis of Films after Deuterium Exposure

Si-H bonds may originate from the a-Si:H film deposited in the CCP and also from reactions of hydrogen with the film upon subsequent exposure to the H_2 ICP. To distinguish between these two sources, D_2 was used in the ICP instead of H_2 .

A combination of three different process times and number of cycles were used in this experiment with constant CCP and ICP conditions (s70, s56 and s58 in Table 4.1). Figure 5.4 shows the infrared spectra after a-Si:H film exposure to D_2 ICPs for different numbers of cycles and D_2 ICP exposure times.

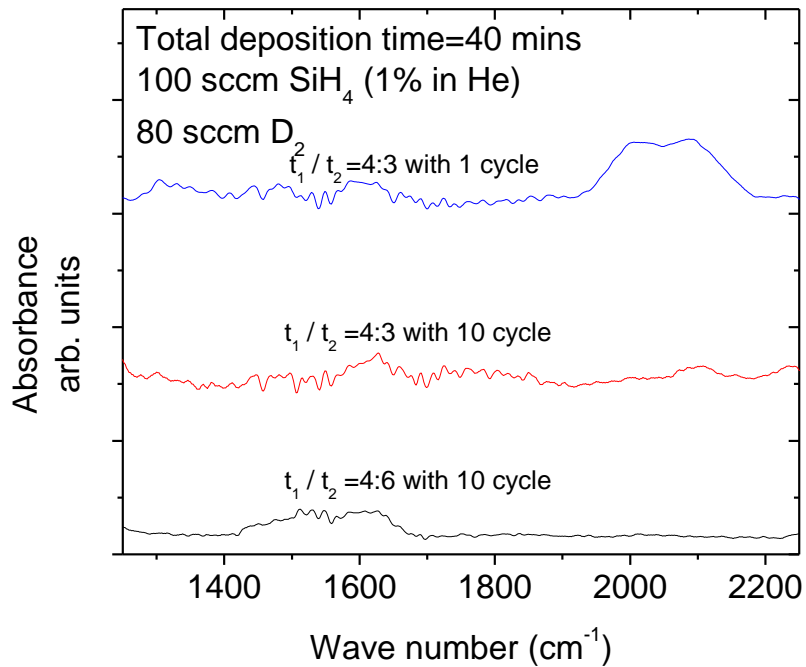


Figure 5.4 Infrared spectra of films deposited in SiH₄ (1% diluted by He) for time t_1 and then exposed to a D₂ ICP for time t_2 . With 1 cycle and $t_1: t_2=4:3$, Si-H bonds were detected, while for 10 cycles and $t_1: t_2=4:3$, the Si-H intensity decreased and the Si-D intensity increased. With longer ICP time ($t_1: t_2=4:6$) the Si-D intensity increased further and the Si-H peak disappeared.

The peaks at 2000 cm⁻¹ and 2100 cm⁻¹ found in the one cycle deposition and D₂ ICP exposure experiment, were due to SiH and SiH₂, respectively. The infrared absorption peaks at 1460 cm⁻¹ to 1622 cm⁻¹ were assigned to SiH_xD_y ($x=0,1,2,3$, $y=0,1,2,3,4$), as shown in Table 5.1. Figure 5.5 shows the infrared spectrum for a sample with $t_1:t_2 = 4:6$, subjected to 10 process cycles.

Table 5.1 Infrared peak assignment for SiH_xD_y (x=0, 1, 2, 3, y=0, 1, 2, 3, 4) on the surface and in the bulk of the film.

Species	Wavenumber (cm⁻¹)	References
SiD	1460	22, 108
SiD on surface	1510	22
SiD ₂ /SiHD	1525	22, 24, 108
SiD ₂ /SiHD on surface	1527	22, 109
SiH ₂ D	1541	109
SiHD ₂	1550	22, 109
SiD ₃	1570	109
SiH ₃ D	1584	109
SiH ₂ D ₂	1591	22, 109
SiHD ₃	1599	22, 109
SiD ₄	1598	110, 111, 112

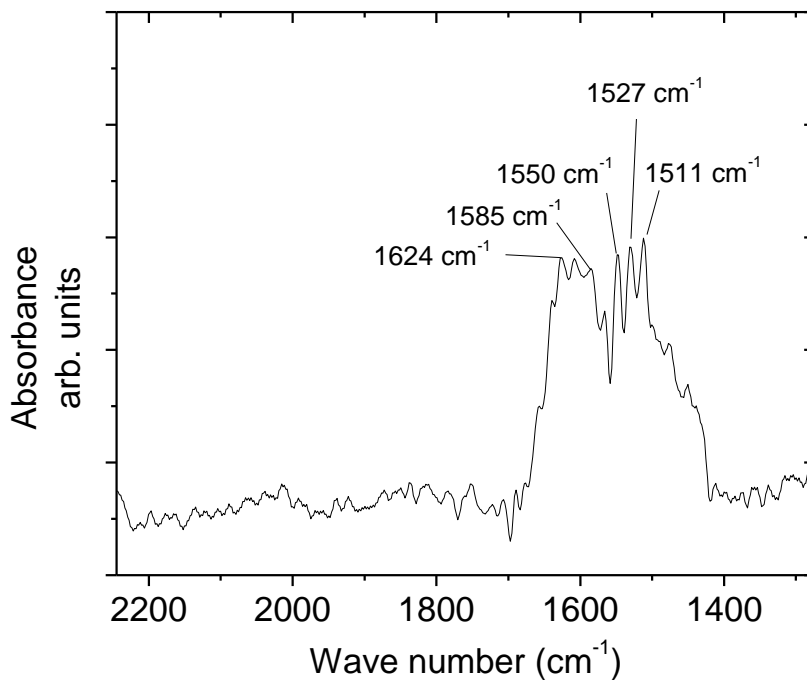


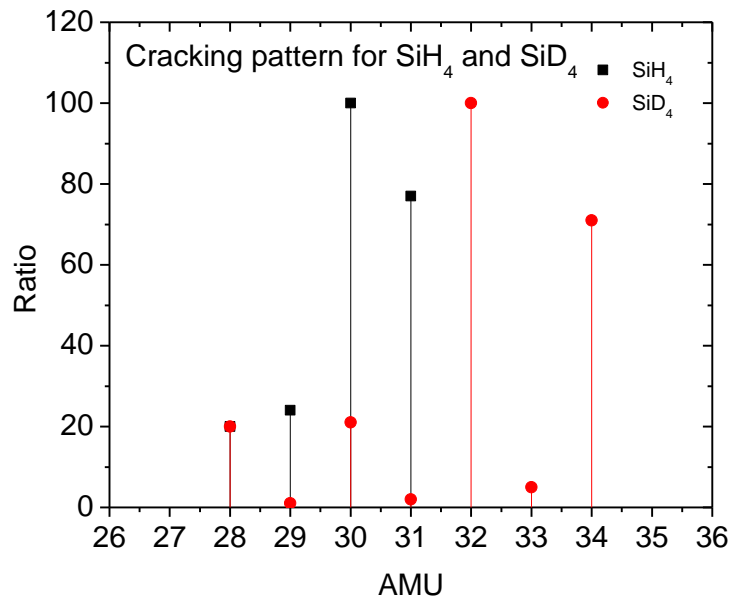
Figure 5.5 Infrared spectra of a sample with $t_1 / t_2 = 4:6$ and 10 process cycles of CCP deposition and ICP D_2 exposure.

Figure 5.4 shows that with the same deposition time / D_2 exposure time (t_1 / t_2) ratio of 4:3, the 2090 cm^{-1} and 2011 cm^{-1} peaks (SiH and SiH₂) decrease dramatically in going from 1 to 10 process cycles, while the peak at 1622 cm^{-1} (SiD₄) increases. Additionally, when the D_2 plasma exposure time t_2 was increased, more Si-D bonds were formed (including SiD, SiHD, SiD₂/SiHD₂, SiH₃D and SiD₄), with vibrational frequencies in the range 1511 cm^{-1} to 1624 cm^{-1} . At the same time the Si-H bonds disappeared, as shown in Figure 5.5. This implies that, for long D_2 exposure time, D can displace all the available H in the film. This is consistent with the experimental results of Aydil and coworkers [22] as well as Parsons [24].

Chapter 6. Mass Spectrometry during ICP Exposure

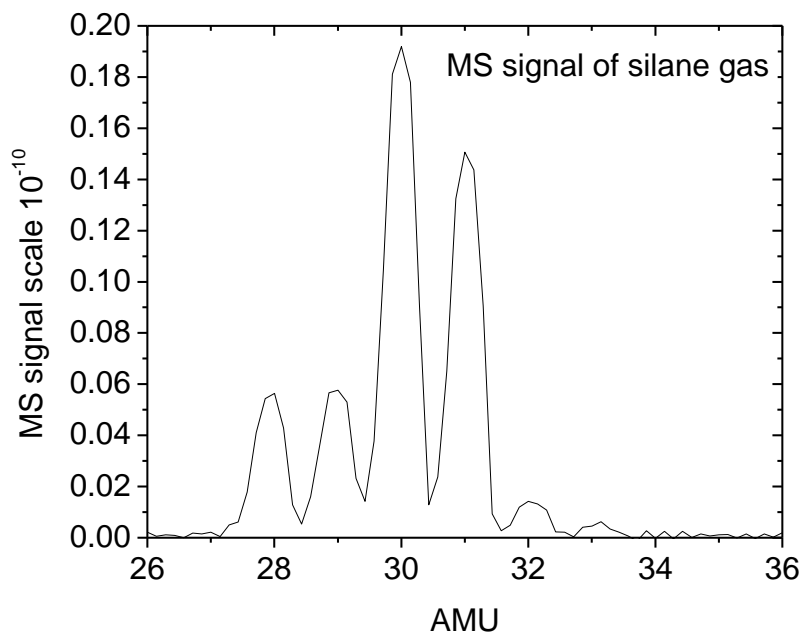
To understand the kinetics of the transition from amorphous to nano-crystalline silicon when a film was exposed to the ICP, D_2 was used instead of H_2 to distinguish H in the starting film from H incorporated in the film during ICP exposure. Deuterated silicon etching products formed in the ICP were detected with a mass spectrometer (MS). Unfortunately, the MS signal of HD (AMU 3) could not be separated from the large background from D_2 (AMU 4) and D and H_2 (AMU 2).

With D_2 fed to the ICP source, the etching products detected included SiD_4 , SiH_4 and SiH_xD_{4-x} . To help determine the possible parent molecules, the cracking patterns of SiH_4 and SiD_4 were examined. Reported cracking patterns of SiH_4 and SiD_4 [108] are shown in Figure. 6.1 (a). The SiH_4 cracking pattern measured in our lab is given in Figure 6.1 (b).



(a)

Figure 6.1 (a) Reported cracking patterns of SiH_4 and SiD_4 [108].



(b)

Figure 6.2 (b) measured cracking pattern of SiH_4 in this work.

Ions formed in the MS ionizer from the etching products $\text{SiH}_x\text{D}_{4-x}$ ($x=0, 1, 2, 3, 4$) at AMU 29 (SiH^+), 30 (SiH_2^+ , SiD^+), 31 (SiH_3^+ , SiHD^+), 32 (SiH_2D^+ , SiD_2^+), 33 (SiHD_2^+) and 34 (SiD_3^+), were monitored during the D_2 ICP exposure. Figure 6.2 shows a typical MS spectrum (with the background removed) at the start of ICP exposure of an amorphous silicon film deposited in the CCP source for 4 min.

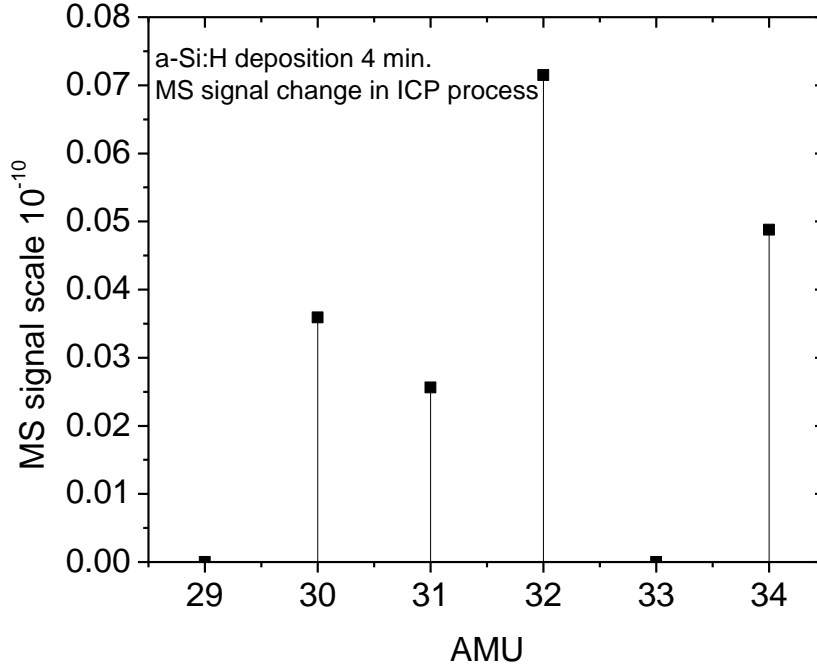


Figure 6.3 MS signal intensity in the range AMU 29 to 34 (after background correction) at the start of ICP exposure of an amorphous silicon film deposited in the CCP source for 4 min.

The strongest signal at AMU 34 comes from SiD_4 which can be an etching product, but also can be formed in the bulk of the plasma. Figure 6.3 shows the signal decay (AMU 29 to 34) as a function of exposure time.

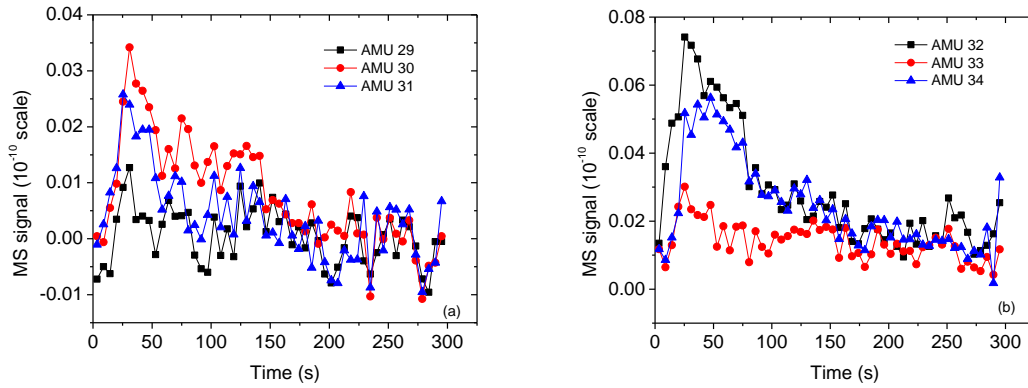


Figure 6.4 MS signal (AMU 29 to 34) decay vs. ICP exposure time.

The decay of MS signals in the AMU range from 29 to 34 showed similar trends. The peak at AMU 34 was selected for monitoring the D₂ ICP exposure for films deposited under different conditions. Figure 6.4 shows the AMU 34 variation with time for different thicknesses of the a-Si:H film deposited in the CCP. The CCP deposition conditions and ICP exposure conditions for the experiments in Figure 6.4 are listed in Table 6.1.

Table 6.1 CCP and ICP process conditions for the experiments in Figure 6.4.

	Gas flow	Pressure (mT)	RF power/frequency	Substrate T (°C)
CCP deposition	SiH ₄ 1% /He 100 sccm H ₂ 40 sccm in CCP source H ₂ 80 sccm in ICP source	710	27 W/13.56 MHz	250
ICP exposure	D ₂ 80 sccm	710	170 W/29 MHz	

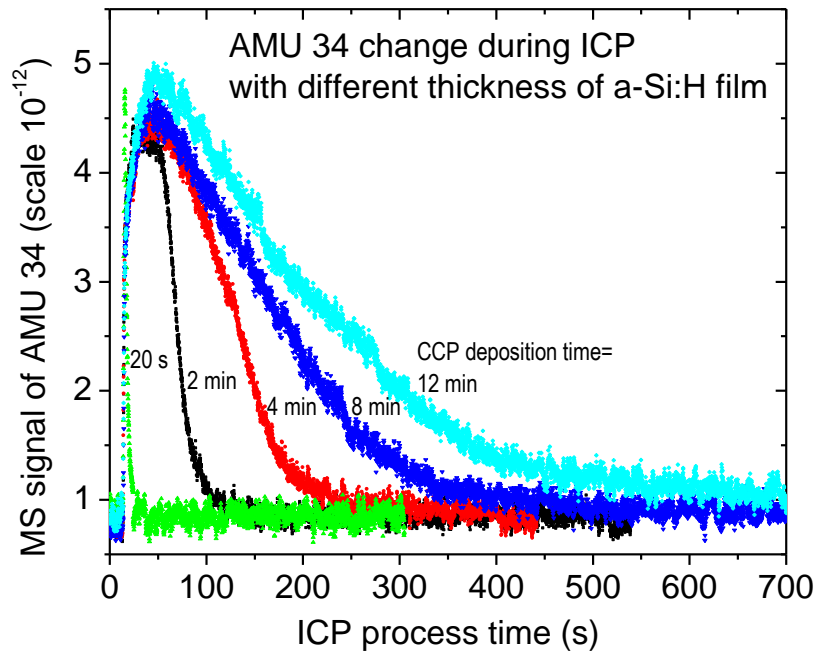
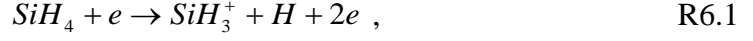


Figure 6.5 Mass spectroscopic signal (AMU 34) variation with D_2 ICP exposure time of films grown in the CCP for different deposition times (and therefore different thicknesses).

With longer a-Si:H deposition time, it takes longer for the MS signal to eventually drop to the baseline. However, even after the MS signal decayed to the baseline, most of the film remained on the substrate, as measured by UV-VIS absorption. Therefore, exposure to D_2 ICP does not remove much of the film. The corresponding etching rate can be estimated from the MS signal intensity of SiD_4 . First, a flow of SiH_4 gas (1% in He) was established in the ICP chamber and the MS signal ($S_{SiH_3^+}$) from SiH_3^+ (AMU 31) was recorded. Power to the plasma was then turned off, the feed gas was switched to D_2 , and power to the ICP was turned back on. The MS signal $S_{SiD_3^+}$ was recorded, corresponding

to SiD₄ products in the D₂ ICP. Assuming that SiH₃⁺ and SiD₃⁺ were formed in the MS ionizer through the reactions,



the partial pressure of SiD₄ can be determined from the relationship,

$$\frac{S_{SiD_3^+}}{S_{SiH_3^+}} = \frac{P_{SiD_4}}{P_{SiH_4}} \cdot \frac{\sigma_{SiD_4}}{\sigma_{SiH_4}} , \quad (6.1)$$

where, P_{SiH_4} is the SiH₄ partial pressure, P_{SiD_4} is the partial pressure of the etch product SiD₄ and $\frac{\sigma_{SiD_4}}{\sigma_{SiH_4}}$ is the dissociative ionization cross section ratio of SiD₄ and SiH₄ to form SiD₃⁺ and SiH₃⁺, (this ratio is ~ 1.062 [113]). Therefore, the SiD₄ partial pressure in the D₂ ICP can be obtained.

The SiD₄ flow rate was then be computed from the partial pressure,

$$\frac{P_{SiD_4}}{P_{D_2}} = \frac{f_{SiD_4}}{f_{D_2}} , \quad (6.2)$$

where, f_{SiH_4} is the flow rate of SiH₄ used at the start. Assuming $P_{SiD_4} \ll P_{D_2}$, then P_{D_2} is the known ICP chamber pressure.

Finally, the etched thickness was computed from

$$thickness = \frac{\int f_{SiD_4} dt * M_{Si}}{22.4 * 10^3 * \rho_{a-Si:H} * A} , \quad (6.3)$$

where $\int f_{SiD_4} dt$ is the time integrated flow rate of SiD_4 , M_{Si} is the molecular mass of silicon, $\rho_{a-Si:H}$ is the density of the amorphous silicon film, and A is the area of the substrate.

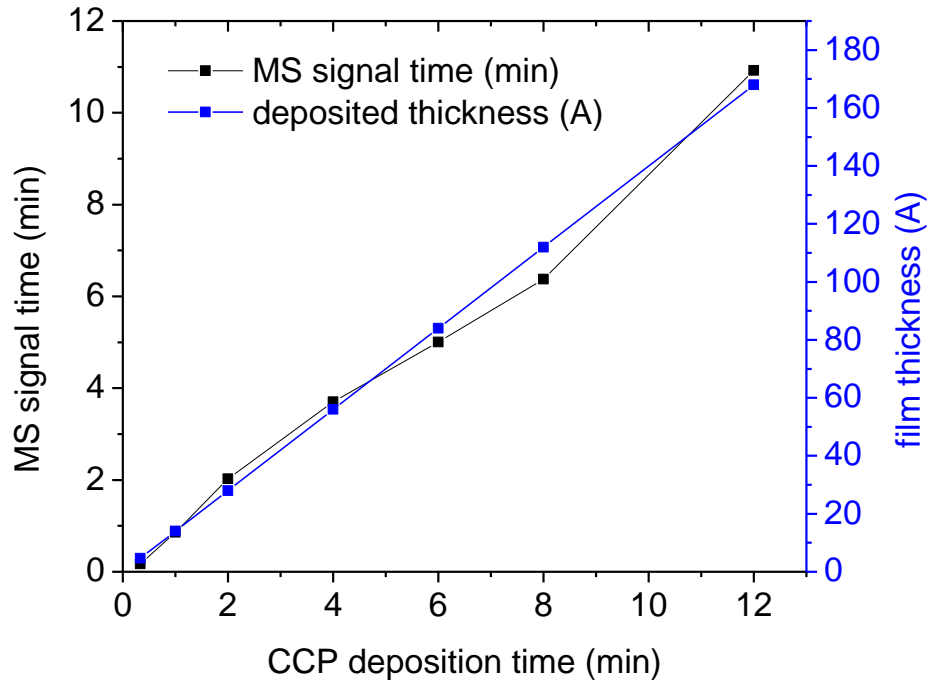


Figure 6.6 Relation between deposited thickness and MS signal time for different CCP deposition times.

In Figure 6.5, the deposited film thickness was obtained by assuming a deposition rate of $14 \text{ \AA}/\text{min}$, as found using UV-VIS absorption in independent experiments. Figure 6.5 shows that thicker a-Si:H films require longer D_2 ICP exposure times for the MS signal to decay to background.

The thickness of the samples used for Figure 6.5 was not measured, since such action would necessitate taking the samples out of the chamber, after deposition. Film deposition and D₂ ICP treatment need to be done without exposing the films to the atmosphere. Otherwise a native oxide would grow and spoil the subsequent etching experiment in the D₂ plasma.

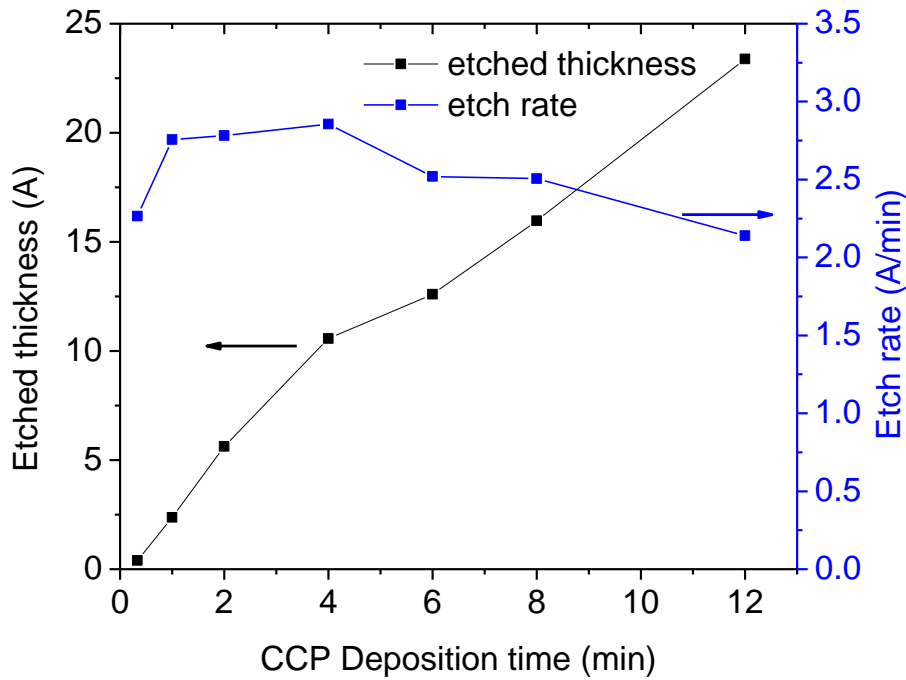


Figure 6.7 Etched thickness and etching rate in the D₂ ICP for films with different CCP deposition times.

The etching rate and etched thickness of the films is shown in Figure 6.6. The etched thickness increases for thicker films, but the etching rate remains constant or decreases slightly when the CCP deposition time exceeds ~ 5 min. The increase of the etched thickness with increasing film thickness shows that etching does not occur

predominantly at the surface of the film. Such a “surface only” etching mechanism was proposed by Shirai [27], and would lead to a SiD_4 signal that would be independent of film thickness and would decay rapidly.

The dependence of the film etching rate to the ICP power was then examined. The other plasma conditions were kept as shown in Table 6.1. Figure 6.7 showed the MS signal change with exposure time for different ICP powers. Films with the same thickness were deposited in the CCP (conditions were listed in Table 6.1) for 4 min. before ICP exposure.

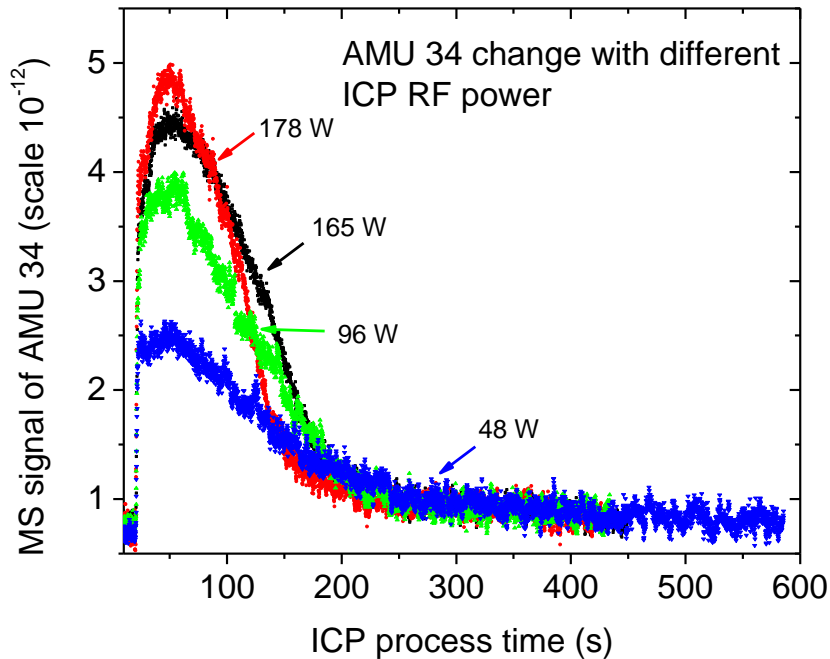


Figure 6.8 MS signal at AMU 34 as a function of time for different ICP powers. All films were deposited under the same CCP conditions, resulting in constant film thickness before exposure to the ICP.

As ICP power was increased, the etching product signal was larger at the start of D₂ ICP exposure, but then the signal exhibited a somewhat shorter time to decay to background. The area under the MS signal in Figure 6.7 should be proportional to the amount of material etched from the film (given by Eqs. 6.1-6.3). Figure 6.8 shows that the integrated MS signal at AMU 34 as a function of ICP exposure time, increases with increasing power.

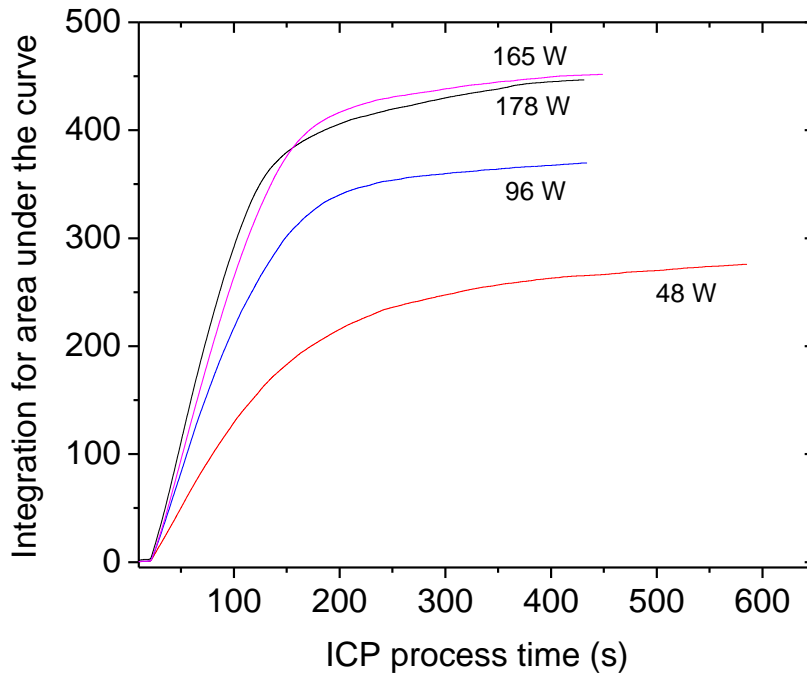


Figure 6.9 Integral of the AMU = 34 signal vs. ICP exposure time for different D₂ ICP powers.

The slope of the curves increases as the ICP power increases. The integrated intensities “saturate” beyond a certain ICP process time. The “saturation” value increases

with power implying that the amount of etching product released also increases with power.

Data reported so far were obtained at a substrate temperature of 250 °C. D₂ ICP etching was also studied at 150 °C. Films were deposited in the CCP on two substrates under 250 °C for 4 min. One of the films was then etched in the D₂ ICP (80 sccm D₂/ 710 mT/ 175 W/ 29 MHz). The other film was held in the vacuum chamber and allowed to cool (at a reduced heating power) until the substrate temperature decreased to 150 °C. The D₂ ICP was then ignited to etch the film. Figure 6.9 shows the MS signal as a function of ICP exposure time for these two temperatures.

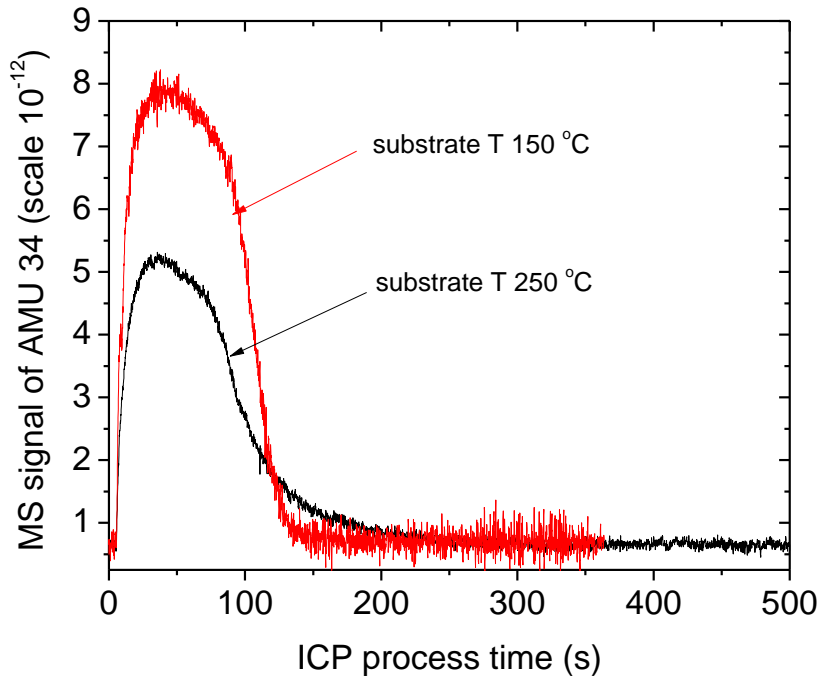


Figure 6.10 MS signal at AMU 34 as a function of ICP exposure time for substrate temperatures of 150 °C and 250 °C. Both films were deposited at 250 °C and were ~56 Å thick.

The areas under the curves were integrated as a function of ICP time and are shown in Figure 6.10. The etching rate (proportional to the slope of the curve) at 150 °C is about two times larger than that at 250 °C. The decrease of Si etching rate in a hydrogen plasma with increasing substrate temperature has been attributed to fast diffusion of H atoms into the film as well as fast recombination that depletes the H atoms [114, 115].

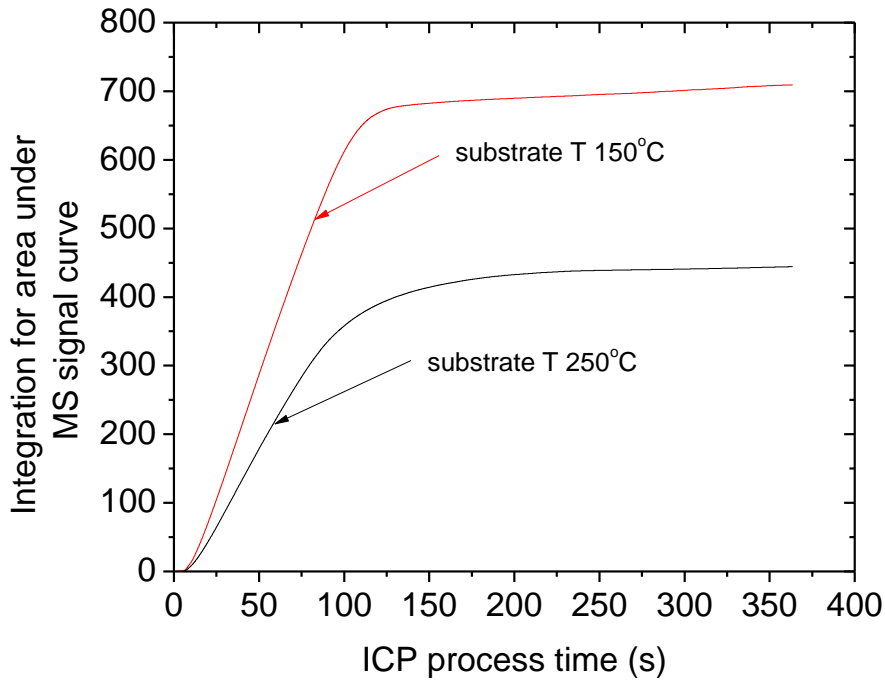


Figure 6.11 Integral of the AMU 34 peak as a function of D₂ ICP process time at different substrate temperatures.

Although a full modeling study was not attempted because to the complex nature of the films that evolves over the deposition and crystallization times. A qualitative mechanism in which H₂ (or D₂) diffuses into the a-Si:H film and SiH₄ (or SiH_xD_{4-x})

diffuses out can explain the decay times in Figures. 6.4 and 6.7 if the D and silane diffusion coefficients start at 6.2×10^{-20} and $1.4 \times 10^{-21} \text{ m}^2\text{s}^{-1}$, respectively, and increase several-fold during the crystallization process, with larger increases occurring for thicker films.

Chapter 7. Spectroscopic Ellipsometry (SE) of Layer-by-Layer Processed Films

In this chapter the properties of layer-by-layer processed films were analyzed by spectroscopic ellipsometry (SE), to estimate film thickness, voids content, and surface roughness, as well as the optical and dielectric constants.

7.1. SE Model and Procedures

Figure 7.1 is a schematic of the ellipsometer (M-2000L, J. A. Woollam Co.) used in the present work. Polarized light from a Xenon arc lamp, in the 250-850 nm wavelength range, was directed onto the film surface with incidence angle $\Phi = 55^\circ$, 65° or 75° (for some samples, a 62° angle was also used for test purposes). A rotating analyzer followed by a detector was used to analyze the reflected beam. The light was binned into 800 wavelengths. The compensator before the rotating analyzer was used to improve the measurement accuracy over the complete range $0-90^\circ$ of Ψ and $0-360^\circ$ of Δ .

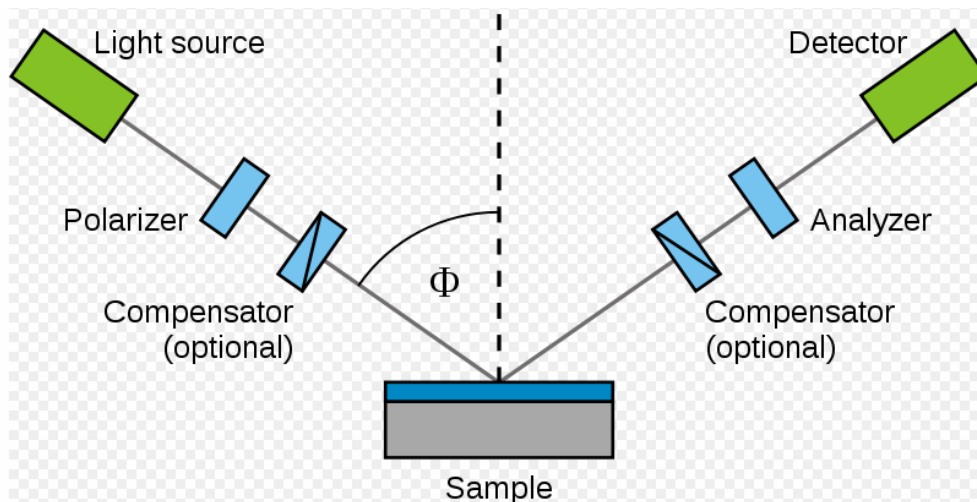


Figure 7.1 Schematic of the spectroscopic ellipsometer.

Surface roughness layer (4)
EMA layer (3)
Crystalline silicon coupling layer (2)
Amorphous silicon coupling layer (1)
Glass substrate (0)

Figure 7.2 Model with five layers for SE data fitting.

SE data were fit using the model structure shown in Figure 7.2. The surface roughness layer (4), as defined by the Woollam WVASE 32 software, is an effective medium approximation (EMA) layer that is a mixture of 50% voids and 50% of the adjacent EMA layer (3) material. The top layer is EMA layer (3) which is composed of a-Si, c-Si and voids. Thus, for example a 40% void EMA layer results in 70% voids for the roughness layer. There is no apparent actual topographic roughness associated with the surface roughness layer. It is assumed to be a homogeneous mixture. Therefore, scattering was not adequately simulated in modeling Ψ and Δ and the modeled results were likely to be sensitive to the angle of incidence (AOI).

The EMA layer consisted of amorphous silicon, crystalline silicon and voids, and was used to simulate the nano-crystalline silicon film. Layer #1, Cody-Lorentz amorphous silicon, and #2 crystalline silicon (Si_Jaw.mat, material data file from J. A. Woollam WASE 32 software [116]) were coupling layers with zero thickness, used to

provide the optical constants for the constituents of the EMA layer. Besides the Cody-Lorentz amorphous silicon component and crystalline silicon component, voids are also included in the EMA layer. The EMA approximation provides a method to mix components with different optical constants, and it is commonly used to model nanocrystalline Si films [96, 97, 99, 117]. To use the EMA approximation two assumptions need to be satisfied: (1) the film is macroscopically homogeneous (i.e., uniformly dispersed components throughout the volume of the layer), and (2) the grain size is smaller than 0.1λ [118]. From Raman spectroscopy, the largest grain size encountered in this work was less than 7 nm, much smaller than 0.1λ .

The optical constants of the crystalline silicon constituent of the EMA were based on data of Herzinger and coworkers [119], which was only used to estimate the percentage of c-Si in the EMA layer and no optical constants were adjusted. The Cody-Lorentz oscillator model was used to describe the complex dielectric function (index of refraction and absorption coefficient) of the amorphous Si component [120],

$$\epsilon(E) = \epsilon_1(E) + i\epsilon_2(E), \quad (7.1)$$

$$\epsilon_1(E) = n^2(E) - k^2(E), \quad (7.2)$$

$$\epsilon_2(E) = 2n(E)k(E), \quad (7.3)$$

where $n(E)$ is the index of refraction and $k(E)$ is the extinction coefficient.

In the Cody-Lorentz oscillator model, seven parameters were fit to determine the optical constants of the film. Eg defines the bandand energy. Amp , En and Br are to find the shape of the absorption peak. Ep , Et and Eu are to determine the absorption edge

[121, 122]. All these parameters as well as the experimental conditions for each sample can be found in Appendix C.

The following steps were performed to fit the SE data by minimizing the mean square error (MSE). Data from sample s76 with an AOI 55° are used as an example below. The curve fit, surface roughness, film thickness and void fraction of the EMA layer, as well as the MSE in each step are shown in Table. 7.1.

1. Fit the thickness of the surface roughness layer, and thickness and void fraction of the EMA layer to obtain a first approximation to the values of each variable.
2. Fix the void fraction in the EMA layer and fit the Cody-Lorentz oscillator model parameters in the amorphous silicon coupling layer. The Cody-Lorentz oscillator parameters are strongly coupled to void fraction. Thus the void fraction was fixed in this step, otherwise the optical constants were found to differ considerably from the known amorphous Si values.
3. Fit % c-Si content of the EMA layer. In some cases, the % c-Si content was negative (e.g., for sample s55 it was -0.54%). In such cases the % c-Si content was set to zero.
4. The void fraction was added to get the final results, using all parameters in the fit.

The initial estimates of the Cody-Lorentz oscillator parameters used in the model were based on SE measurements of SiH_4/He deposited on fused silica substrates. These films exhibited minimal surface roughness, no voiding, nor crystal silicon based on SE

analysis. Two film deposits ($\sim 150 \text{ \AA}$ and 1500 \AA) and two areas of each film were fit simultaneously to yield a “best estimate” of Cody-Lorentz parameters to use as initial values. In addition, they show very good agreement with the optical constants of Aspnes material (see Figure 7.12 below). Sample s76, which has the largest crystalline volume fraction, is used as an example to show the fitting steps.

Table 7.1 Surface layer thickness, thickness of EMA layer, void fraction, crystalline volume fraction and MSE of sample #76 after each fitting step. The actual curve fits (x-axis is the photon energy (eV) and y-axis is Ψ) are also shown.

	Dashed curves =experimental data, solid curves =fits	Surface layer thickness (\AA)	EMA film thickness (\AA)	Void fraction (%)	Crystalline Si fraction (%)	MSE
Step 1		25.22	735.5	51.99	0	113.5
Step 2		65.18	715.89	51.99	0	11.58
Step 3		64.73	716.13	51.99	2.93	11.2
Step 4		64.73	716.13	51.99	2.93	11.2

The dielectric constants of the EMA layer#3, and the solid a-Si coupling layer #1, of sample s55, are shown in Figure 7.3, in comparison with the dielectric constants of a-Si from Aspnes in the Woollam material library [123, 124].

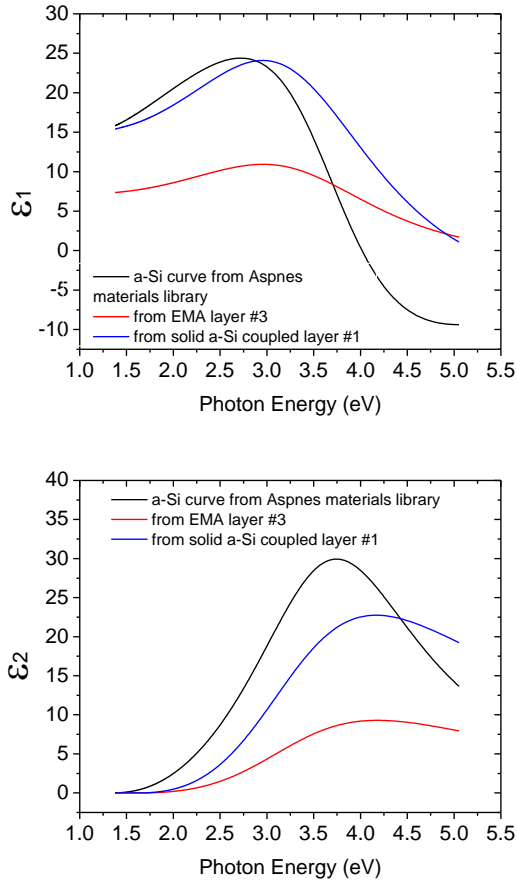


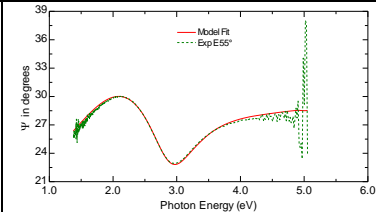
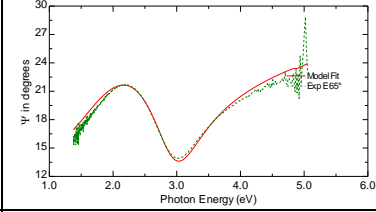
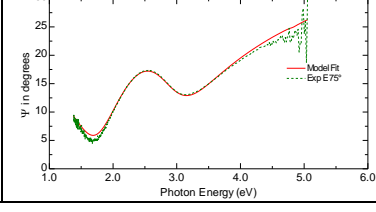
Figure 7.3 Dielectric constants ϵ_1 and ϵ_2 of sample s55 obtained by SE fitting, compared to those from the Aspnes material in the Woollam material library.

The fitted dielectric constants ϵ_1 and ϵ_2 of the solid a-Si in the coupled layer #1 are comparable with the Aspnes data but the peak value of the fit is shifted towards higher photon energies by about 0.25 eV. The peak values of the dielectric constants derived from the EMA layer were much lower than those of Aspnes, which could be caused by

the 40% void fraction in the EMA layer. Therefore, in the analysis below, the dielectric and optical constants were all derived from the solid a-Si layer #1.

Ellipsometric spectra were collected at three AOI and the data are shown in Table 7.2. The three AOI fits of thickness differ by less than 0.3% $((\text{max}-\text{min})/\text{max} \times 100\%)$. Under larger AOI, more scattering from the surface is expected, which could result in higher MSE. Since the MSE at AOI=55° is the lowest, in the following analysis, the results from AOI=55° were used. Figure 7.4 shows the MSE for all the samples subjected to layer-by-layer processing. Samples s58, s69, s70 and s75 had MSE larger than 10.

Table 7.2 Fits for sample s55 at three AOI. The MSE at AOI=55° was the lowest.

AOI	Dashed curves=experimental data, solid curves=fits	Surface roughness (Å)	EMA film thickness (Å)	Void fraction (%)	MSE
55°		40.77	575.42	40.7	4.62
65°		42.27	574.85	40.1	9.02
75°		48.36	576.44	38.1	8.25

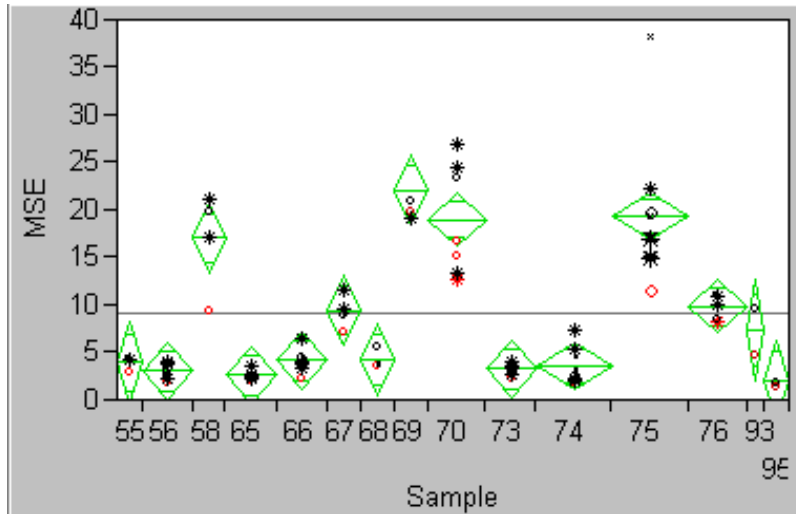
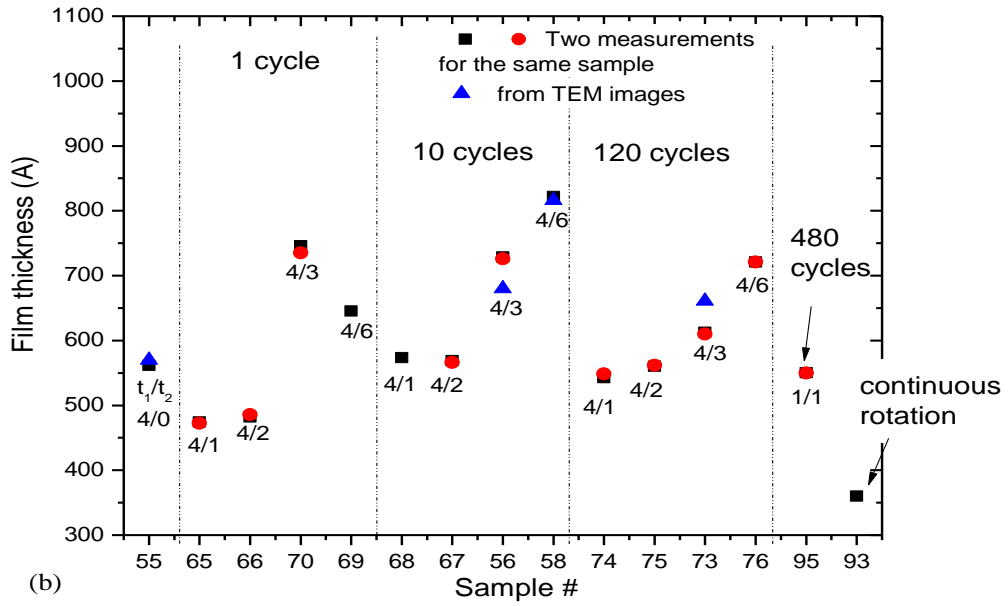
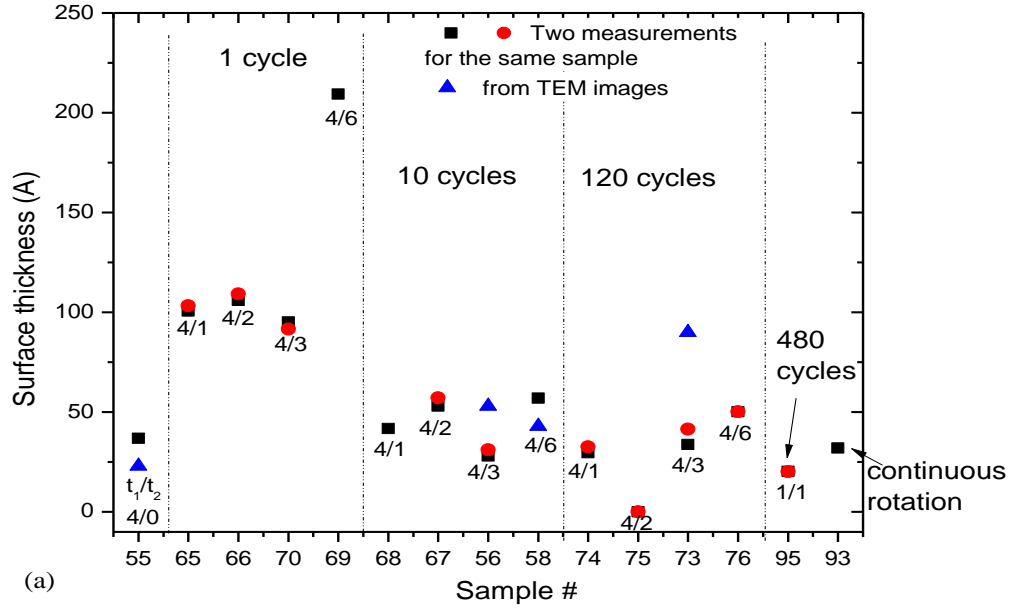


Figure 7.4 MSE for all samples subjected to layer-by-layer processing. x-axis is the sample number, y-axis is MSE. Different patterns correspond to different AOI (red circle AOI=55°; black star AOI=62°; black circle=AOI 65°).

7.2. SE Analysis Results

The layer-by-layer processed samples subjected to total deposition time of 40 min, but different H₂ exposure times (as well as the sample subjected to continuous rotation) were analyzed by SE. Figure 7.5 shows fitting data based on the procedure discussed in 7.1, including surface roughness layer thickness (Figure 7.5a), EMA film thickness (Figure 7.5b), and void fraction (Figure 7.5c), respectively.



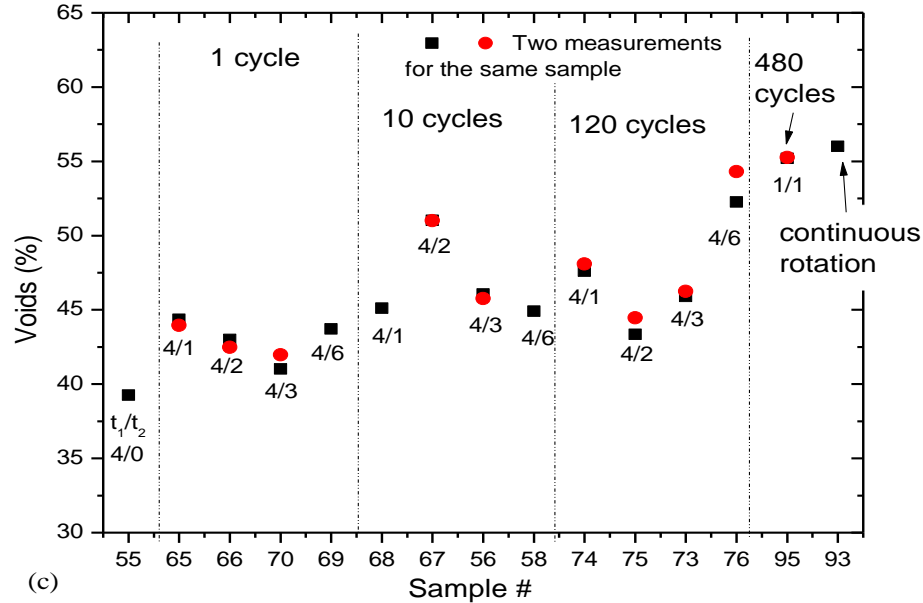


Figure 7.5 SE fitting data, including surface roughness layer thickness (a), film thickness (b), and void fraction (c) for samples with the same (40 min) total deposition time, but various H_2 exposure times and different number of cycles. The sample subjected to continuous rotation is also included. Red and black symbols were measurements from samples at identical conditions processed on different days. Blue symbols in (a) and (b) were measurements from TEM images. The x-axis is the sample number #. The ratios under the symbols are the t_1/t_2 time ratios for each cycle.

Figure 7.5 (a) shows that all samples had a surface roughness layer except for sample s75 (120 cycles, $t_1/t_2 = 20$ s/10 s). However, the MSE for this sample was quite high (~ 20), and this sample appears to be an outlier. The surface roughness layer thickness for the samples subjected to 1 cycle was around 100 \AA , except for sample s69 (with 40 min CCP deposition and 60 min H_2 exposure) which, according to SE, had a thickness of 200 \AA . This sample may also be an outlier. Unfortunately, there are no TEM data for these samples. For such samples, the long H_2 exposure might contribute to increased roughness of the surface layer. The surface layer thickness was around 50 \AA for

the samples subjected to 10 cycles (with maximum H₂ exposure of 6 min per cycle) and 120 cycles (with maximum H₂ exposure of 30 s per cycle). Measurements based on TEM images (blue triangles) were comparable except for sample s73. Figure 7.6 shows the statistical analysis using JMP software (“John's Macintosh Project”, from SAS Institute Inc., version 4.0.2) of the surface layer thickness versus number of cycles.

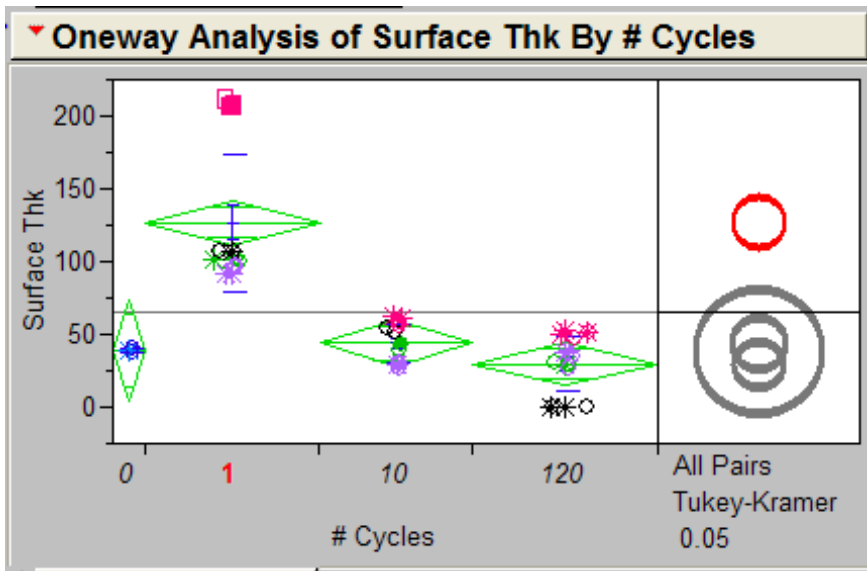


Figure 7.6 Surface layer thickness (Å) as a function of number of cycles (the outlier sample s75 was excluded). The circles on the right are indicators of the distribution of the samples with the same number of cycles. The different symbols at the same number of cycles were measured under different AOI (55°, 62°, 65°). Different colors indicate different t_1/t_2 time ratios, with the same number of cycles (blue: $t_2=0$; green: $t_1/t_2=1/4$; black: $t_1/t_2=2/4$; purple: $t_1/t_2=3/4$; pink: $t_1/t_2=6/4$). The horizontal line of the green diamond for each group shows the mean value of the group (groups have the same number of cycles). The vertical span of the diamonds shows the 95% confidence interval of the mean value.

Figure 7.6 shows that as the layer-by-layer process cycle number increases from 1 to 120 cycles, the surface layer thickness decreases. However, for the same number of cycles, there is no apparent trend of the surface layer thickness versus t_1/t_2 .

Looking back at Figure 7.5b, for samples with the same deposition time and various hydrogen exposure times, the EMA layer thickness had a mean value at 613 Å and a range of 348 Å. For 40 min CCP deposition, the thickness of sample s55 was 562 Å. The CCP deposition rate was, therefore, around 14 Å/min. When the H₂ exposure time was longer than 30 min, nano-crystallization occurred even in this relatively thick film (see Figure 4.6 (a), X_c of sample s70 was 7.6%). The difference between the thickness measurement by TEM images and SE analysis for samples s55, s56, s58 and s73 was less than 7.3%. The thickness of samples subjected to the three different number of cycles increased when the t_2/t_1 was larger than 3/4. This increase became less apparent when the number of cycles increased as shown in Figure 7.7.

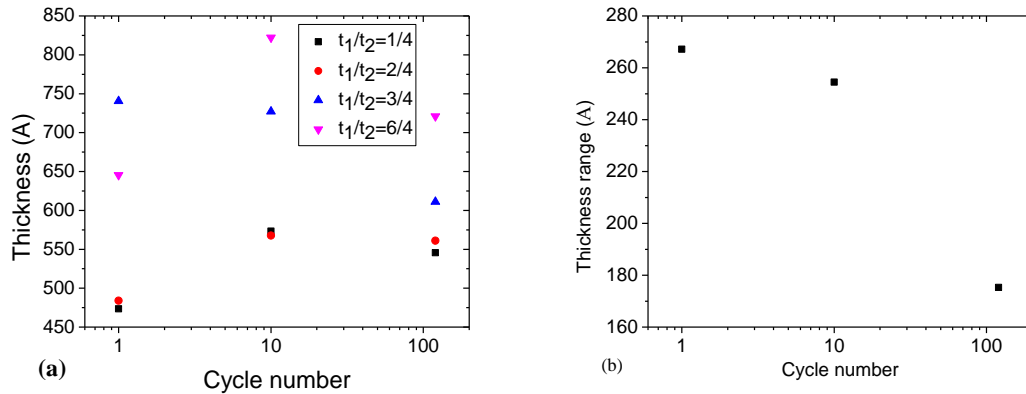


Figure 7.7 (a) Film thickness distribution with various t_1/t_2 as a function of number of cycles. (b) Range of film thicknesses as a function of number of cycles.

During H₂ ICP exposure, etching and nano-crystallization are thought to occur. From Figure 7.5 (b), the thickness of sample s55 (which was not exposed to H₂ plasma), is not substantially different than the rest of the samples which were subjected to the same deposition time but also to the H₂ ICP. Only the thickness of samples s65 ($t_1=40$

min, then $t_2=10$ min) and s66 ($t_1=40$ min, then $t_2=20$ min) decreased by 88 Å and 77 Å, respectively. This implies that etching does not contribute much to decreasing the film thickness. However, etching may increase the void fraction of the film. The increase of the film thickness for some samples over and above the deposited film thickness may be due to process variability and/or uncertainty in film thickness measurement.

H₂ exposure did result in increased film porosity as shown in Figure 7.5 (c). Sample s55 had the lowest void fraction (39%), while sample s93 (subjected to continuous rotation) had the highest void fraction (56%). The trend of the void fraction as a function of t_1/t_2 was not monotonic. However, the void fraction increased with increasing number of cycles shown by the statistical analysis in Figure 7.8. Voids can provide a mechanism for releasing the strain in the amorphous silicon film, thus promoting the nucleation of crystallites [75, 117]. They will also lead to a larger effective diffusivity of D₂ and silane in the film, perhaps explaining the mass spectrometer decay measurements as a function of thickness, presented in Ch. 6.

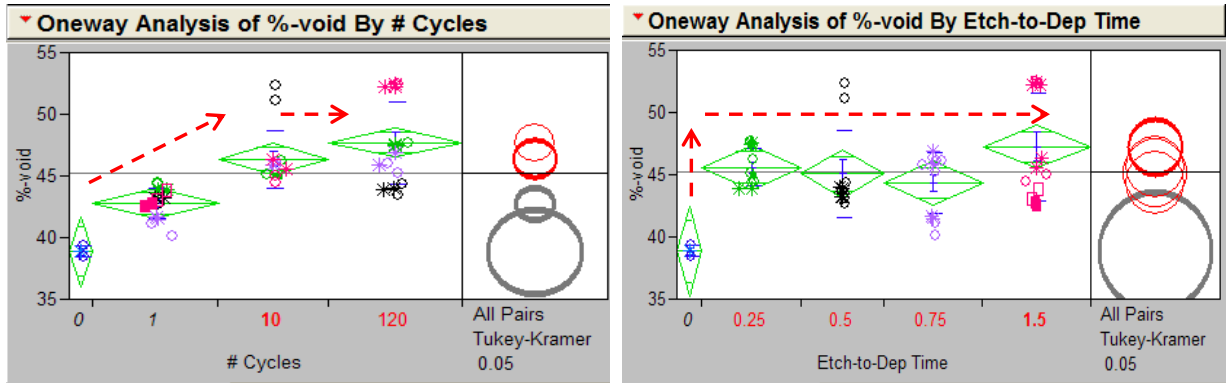


Figure 7.8 Void fraction as a function of number of cycles (left) and t_2/t_1 (right) for the layer-by-layer processed samples subjected to only CCP deposition, 1 cycle, 10 cycles and 120 cycles. The circles on the right are indicators of the distribution of the symbols under the same number of cycles. The different kinds of symbols at the same number of cycles were measured under different AOI (55° , 62° , 65°). Different colors correspond to different t_1/t_2 time ratios, under the same number of cycles (blue: $t_2=0$; green: $t_1/t_2=1/4$; black: $t_1/t_2=2/4$; purple: $t_1/t_2=3/4$; pink: $t_1/t_2=6/4$). The horizontal line of the green diamond for each group shows the mean value of the group (groups have the same number of cycles). The vertical span of the diamonds shows the 95% confidence interval of the mean value.

In the model of Figure 7.2, the EMA layer consisted of crystalline silicon, amorphous silicon and voids. The fraction of crystalline silicon includes only crystallites larger than about 50 nm. Crystallites above this size are expected to exhibit optical properties represented by crystalline Si, as will film containing them. From the analysis of SE, the crystalline fraction as a function of number of cycles is shown in Figure 7.9.

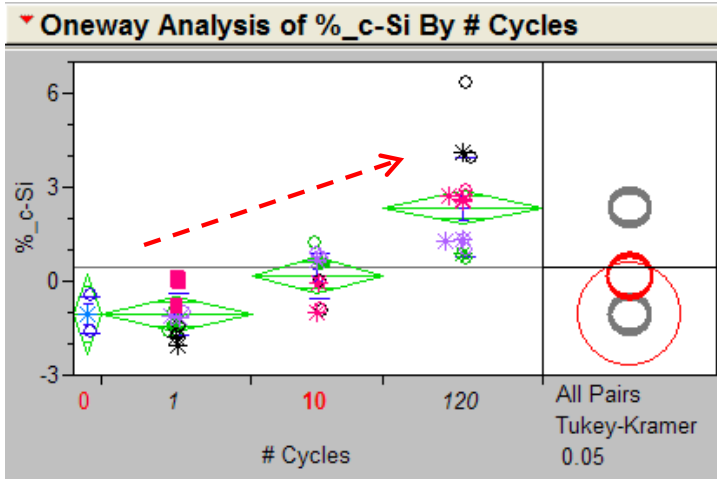


Figure 7.9 Crystalline fraction from SE analysis as a function of the number of cycles for the layer-by-layer processed samples subjected to only CCP deposition, 1 cycle, 10 cycles and 120 cycles. The circles on the right are indicators of the distribution of the symbols under the same number of cycles. The different symbols at the same number of cycles were measured under different AOI (55° , 62° , 65°). Different colors indicates different t_1/t_2 time ratios, under the same number of cycles (blue: $t_2=0$; green: $t_1/t_2=1/4$; black: $t_1/t_2=2/4$; purple: $t_1/t_2=3/4$; pink: $t_1/t_2=6/4$). The horizontal line of the green diamond for each group shows the mean value of the group (groups have the same number of cycles). The vertical span of the diamonds shows the 95% confidence interval of the mean value.

The crystalline volume fraction from SE analysis increased with the number of cycles, consistent with the results of Raman spectroscopy (Figure 4.6 (b)). However, the values of the crystalline fraction based on SE analysis were considerably lower than those from Raman spectroscopy. That could be because the crystalline volume fraction from Raman spectroscopy was based on the whole film being solid, while the crystalline fraction estimated by SE included nearly 50% voids. The crystalline fraction from the SE analysis had negative values for the samples with low number of cycles. Therefore, only the trend that more crystalline Si is present with films processed with 120 cycles compared to 10 or less cycles should be considered reliable. The crystalline fraction change with the ratio of CCP deposition to H_2 exposure is shown in Figure 7.10.

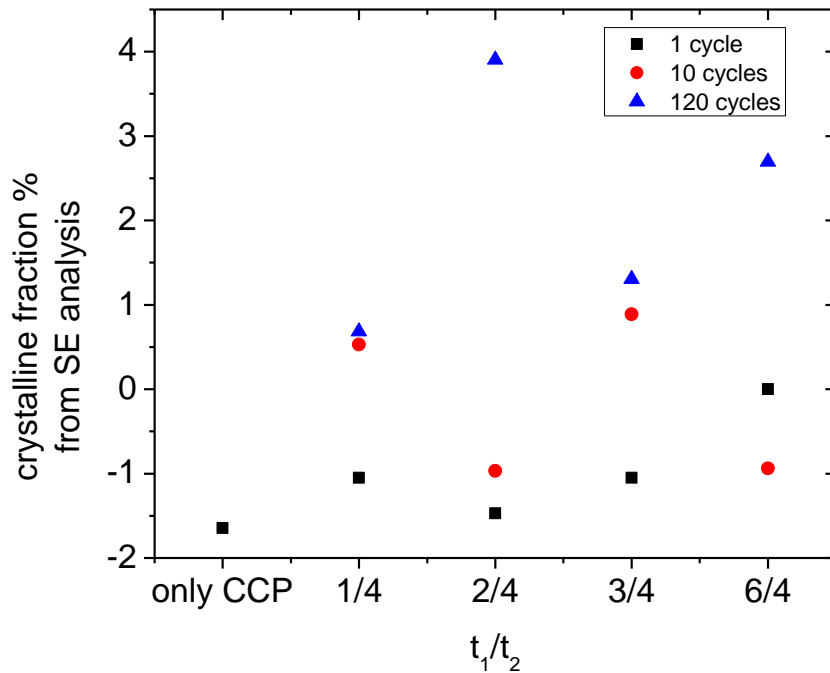


Figure 7.10 Crystalline silicon fraction from SE analysis as a function of t_1/t_2 . Black, red and blue symbols correspond to samples subjected to 1, 10 and 120 cycles, respectively.

While there was no clear monotonic variation of the crystalline silicon fraction with t_1/t_2 , it does appear that there is an upward trend, consistent with the Raman data where crystalline volume fraction increased with the ratio t_2/t_1 for all the groups with different number of cycles. It is possible that the large grain crystalline silicon (modeled by SE) did not change much as the H_2 exposure time increased. However, small grains could contribute to the change of the optical and dielectric constants of the amorphous layers in the SE model. Figure 7.11 shows the distribution of the Cody-Lorentz oscillator bandgap energy E_g for the layer-by-layer processed samples, except for the outlier sample s75.

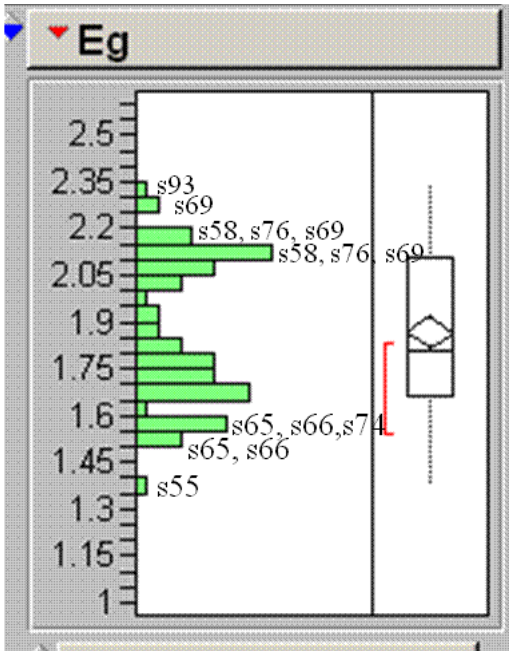


Figure 7.11 Distribution of Cody-Lorentz oscillator bandgap energy E_g for all the layer-by-layer processed samples. The right side of the figure showed the statistics information for the distribution, i.e. the mean value of E_g and upper/lower 95% mean shown by the diamond, median value of E_g and upper/lower quartile of median shown by the box.

E_g is defined as the threshold before the rapid rise of optical absorption [125], and is a critical parameter in determining the dielectric and optical constants of the material. From Figure 7.11, the samples (s55, s65, s66) with close to zero crystalline volume fraction, had low bandgap energy, while the samples (s93, s76, s58, s69) with high crystalline volume fraction had high bandgap energy. The high bandgap energy could be caused by the decrease of the states at the top of the valence band. The hydrogen content was increased with high bandgap energy [126, 127]. With increased hydrogen content, dangling bonds were saturated and weak Si-Si bonds were replaced by strong Si-H bonds. However, in Chapter 5, the results from IR analysis showed that, with longer H_2 ICP exposure, the crystalline volume fraction increased and the H content of the films

decreased a bit. Therefore, the bandgap energy increase from the SE analysis could be just an indicator of a stronger Si-H network formed in the film, which could also result in a shift towards higher photon energy in the peak of the dielectric constant ϵ_2 [28] (see below).

Figure 7.12 shows the dielectric constants ϵ_1 and ϵ_2 as a function of photon energy for amorphous silicon from Aspnes, crystalline silicon from reference [119], and a-Si:H deposited in this work with 6 sccm SiH₄ diluted by 594 sccm He in the CCP. Sample s55, which was processed with 1 sccm SiH₄ (1% SiH₄ diluted in He) and 40 sccm H₂ in the CCP is also included. ϵ_1 and ϵ_2 in the present work were derived from the solid amorphous silicon coupling layer of Figure 7.2.

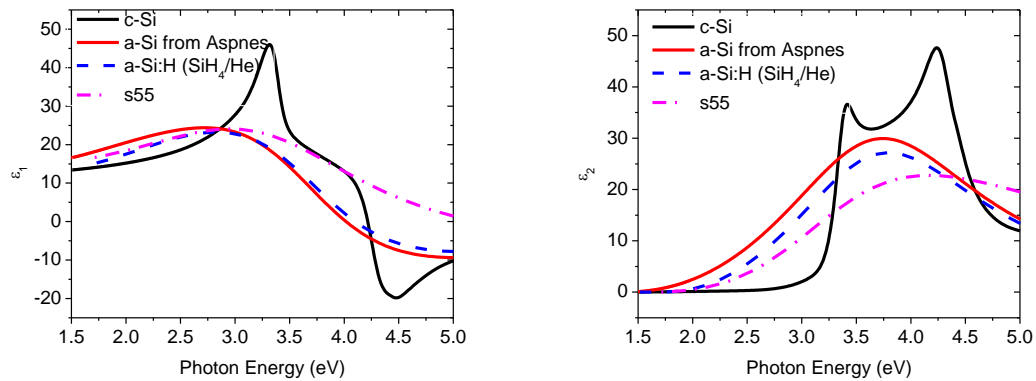


Figure 7.12 Dielectric constants ϵ_1 and ϵ_2 as a function of photon energy for crystalline silicon (black solid curve), Aspnes amorphous silicon (red solid curve), a-Si:H deposited with SiH₄ diluted in He (blue dashed curve) and sample s55 deposited with SiH₄ diluted in He and H₂ (purple dashed curve).

The dielectric constant curves of a-Si from the Aspnes material in the Woollam material library show a wide peak at around 2.7 eV, while the c-Si curve has two critical

points at 3.4 eV and 4.2 eV. The appearance of a peak at 4.2 eV indicates the transition from amorphous to crystalline phase [99, 117]. The a-Si:H film deposited by only SiH₄ and He (blue dashed curve), with zero voids (as measured and predicted by SE), has quite similar dielectric constants with the Aspnes a-Si (red solid curve). However, sample s55, deposited in the CCP using SiH₄ diluted in He and H₂ gas mixture shows blueshifts for both ϵ_1 and ϵ_2 . The structure of the film after hydrogen exposure may be changed, resulting in a shift of the dielectric constants. Figure 7.13 shows ϵ_2 for the samples subjected to 1, 10, 120 and 480 cycles.

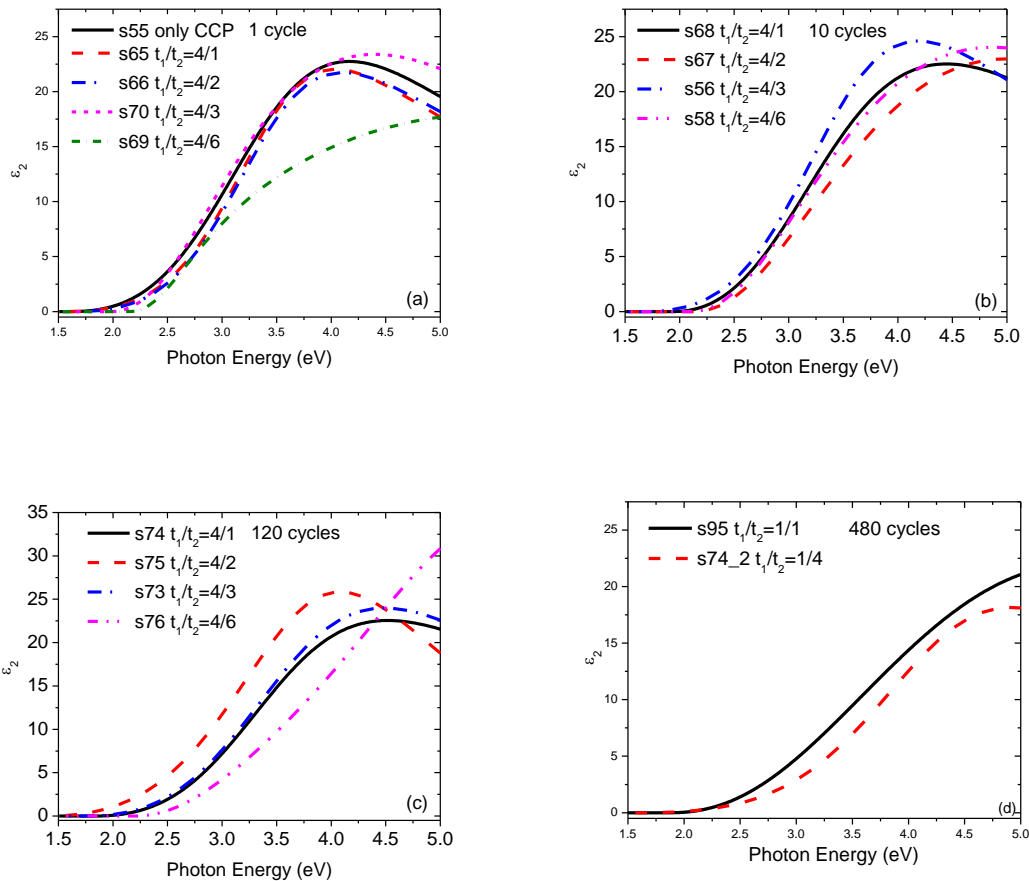


Figure 7.13 Dielectric constant ϵ_2 of layer-by-layer processed samples with various CCP deposition to H₂ ICP exposure time ratios. (a) samples subjected to 1 cycle, (b) 10 cycles, (c) 120 cycles and (d) 480 cycles.

With larger t_2/t_1 time ratios, the peak of ϵ_2 has more of a blue shift, except for samples s75 and s56 which show redshifts. Sample s75, as mentioned before, had an MSE of over 20, and was thus considered an outlier. For sample s56, the MSE was about 5 and its Raman spectrum (X_c 12%) showed a little larger crystalline volume fraction than that of sample s67 (X_c 9%). The reason for the redshift is not clear. For the other samples, the blueshift of the dielectric constant ϵ_2 might be indicative of the presence of small grain crystallites, which do not register as crystalline fraction in the EMA layer, or from the two critical points, shown with black curve in Figure 7.12b.

The dielectric constant of the amorphous coupling layer shows the presence of small crystallites. Figure 7.14 shows the SE results of ϵ_2 from the EMA layer (mixture of amorphous silicon, crystalline silicon and voids) with 50% voids and different fractions of crystalline silicon.

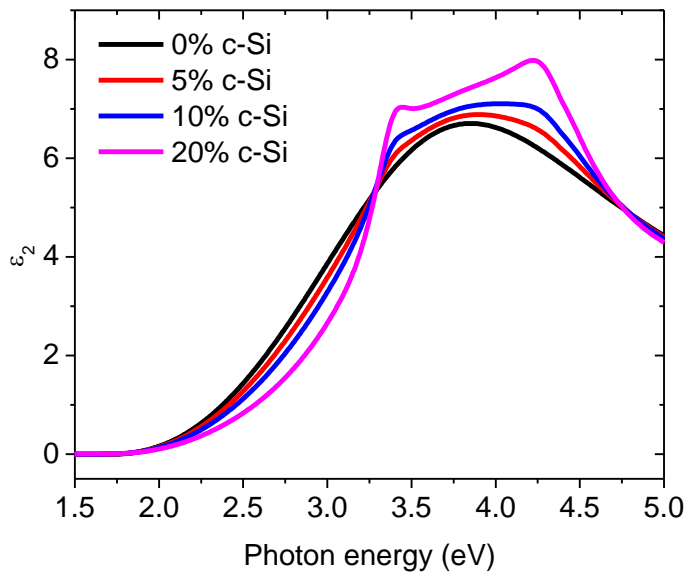


Figure 7.14 Simulated ϵ_2 from EMA layer as a function of photon energy with various crystalline silicon volume fractions.

Figure 7.15 shows ϵ_2 of the EMA layer for samples s55 (only CCP deposition), s69 (1 cycle, $t_1/t_2 = 4/6$) and s76 (120 cycles, $t_1/t_2 = 4/6$), which had X_c of 0%, 12%, and 38%, respectively (based on the three-peak deconvolution of Raman spectra, see section 2.6.1).

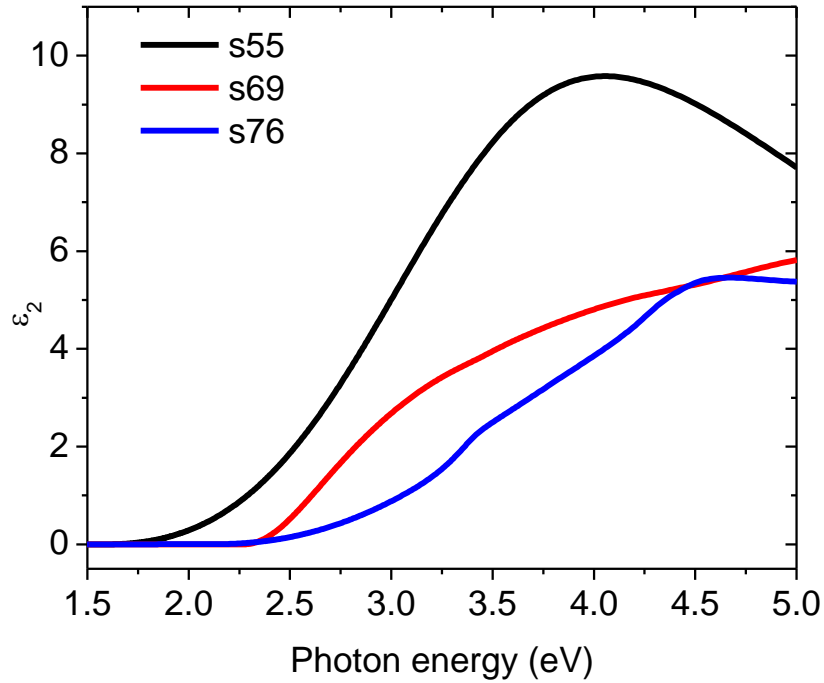


Figure 7.15 ϵ_2 of EMA layer for samples s55, s69 and s76.

The dielectric constant ϵ_2 of the EMA layer of sample s76 shows two peaks at 3.5 eV and 4.5 eV, which are the critical points of crystalline silicon. For sample s69, with 0% crystalline silicon fraction predicted by SE, ϵ_2 was blueshifted, similar to ϵ_2 of the solid amorphous layer. However, even though SE suggests no crystalline phase, small grain crystallites could still be present, in agreement with the results of Raman spectra

(12% X_c based on three-peak deconvolution). The decrease of the maximum value of ϵ_2 could be due to the voids in the film. Figure 7.16 shows simulation results of ϵ_2 of the EMA layer with increasing void fraction. The peak intensity decreases with increasing void fraction, but the relative shape is nearly constant, with a peak at 3.8 eV.

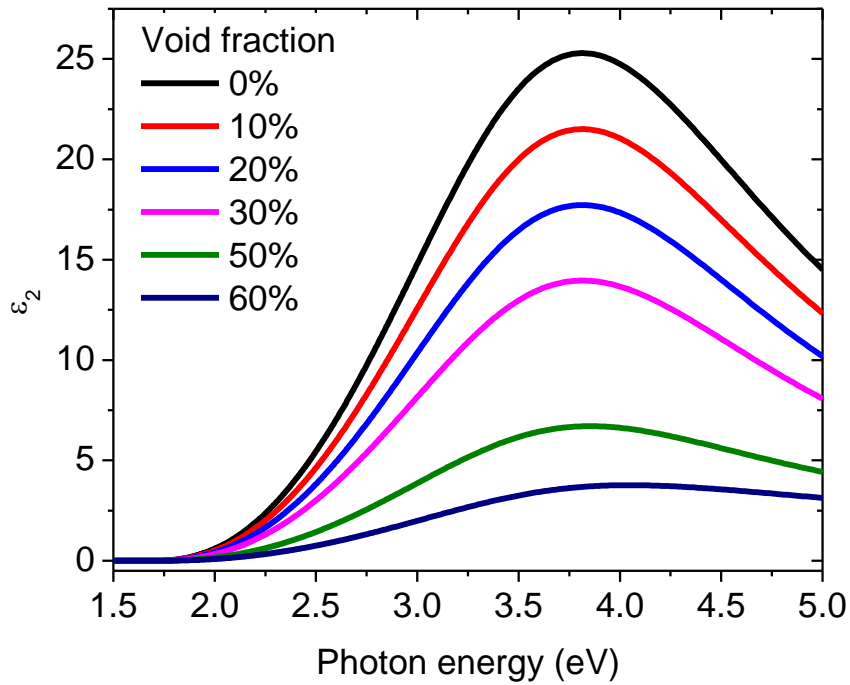


Figure 7.16 Simulated ϵ_2 of EMA layer with various void fractions.

The optical constants also show some shift for the samples with high crystalline volume fraction, e.g., sample s76, with $X_c=38\%$, and sample s95, with $X_c=49\%$. Figure 7.17 shows the fitted absorption coefficient of the EMA layer.

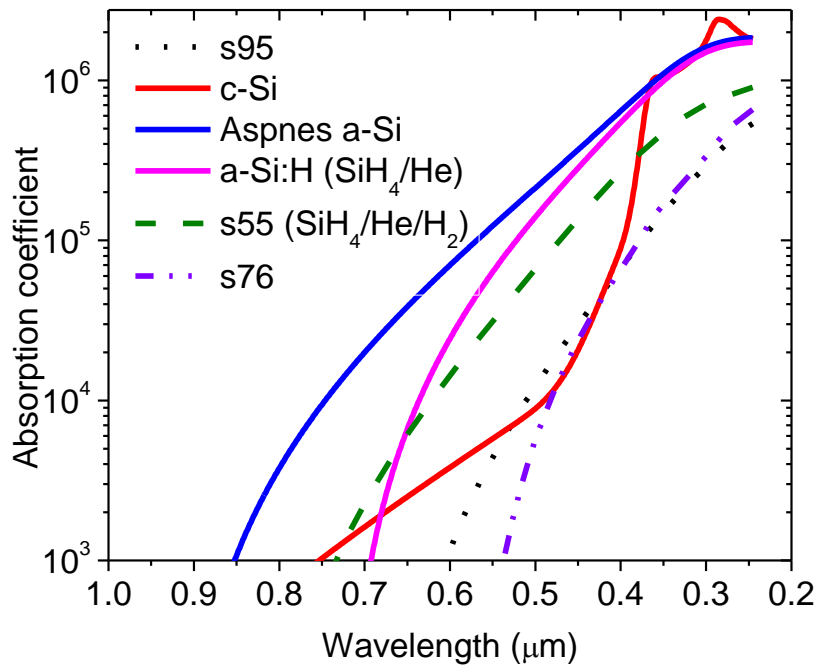


Figure 7.17 Absorption coefficient of the samples with zero crystalline volume fraction (a-Si:H and s55) and high nano-crystalline volume fraction (s76 and s95) compared to that of a-Si from the Aspnes material and c-Si in the Woollam material library.

The a-Si:H film deposited with SiH₄ diluted in He shows similar absorption coefficient to that reported by Aspnes for a-Si between 0.25 and 0.5 eV [123, 124]. Between 0.5 and 0.7 eV, the absorption coefficient in the present study lies increasingly lower than that of Aspnes. The absorption coefficient of sample s55 was comparable with a-Si:H film with only SiH₄ (diluted in He). However, the samples with high nano-crystalline volume fraction (s76 and s95) showed much lower absorption coefficient compared to a-Si:H films. Over the range 0.48 to 0.4 μm, the absorption coefficient was similar as that of c-Si, but outside this range, the absorption coefficient of samples s76 and s95 was lower than that of c-Si.

The dielectric constants and absorption coefficients of the samples with high crystalline volume fraction show shifts indicative of increased crystalline silicon. But from the SE model, no large crystalline silicon fraction (it was less than 4%) was obtained. The shift of the dielectric and other constants could be an indicator of the presence of small crystallites in the amorphous phase. The transmission spectrum and optical constants for all the samples can be found in Appendix D.

Chapter 8. TEM Characterization of Layer-by-Layer Processed Films

In this chapter cross-sectional bright-field transmission electron microscopy (TEM) and dark-field scanning transmission electron spectroscopy (STEM) of samples s55 (40 min CCP deposition), s56 (10 cycles, $t_1/t_2=4$ min/3 min), s58 (10 cycles, $t_1/t_2=4$ min/6 min), s73 (120 cycles, $t_1/t_2=0.3$ min/0.25 min) and s74_2 (120 cycles, $t_1/t_2=0.08$ s/0.3 s) are discussed. Images were acquired from the center region of the 1 inch samples. The film thickness ranged from 30~100 nm.

STEM dark-field images were taken by using a standard high angle annular dark field (HAADF) STEM detector. The incidence angle of the electron probe was converged to 4.5 milliradians (mrad) and the angular range of the electrons collected was between 5.6 to 12 mrad (half-angle). The angle was optimized for Si (111) diffraction with the bright regions corresponding to the crystalline material. STEM images were taken for three samples, s55 ($X_c=0\%$ (using the three-peak method from Raman spectroscopy), s58 ($X_c=24\%$) and s74_2 ($X_c=72\%$). Figure 8.1 shows a cross sectional image of sample s58, including the SiO₂ substrate, at 100 nm resolution (a) and 50 nm resolution (b). The surface of the film was coated with a Au-Pd sputtered layer to prevent charging during sample preparation using a focused ion beam (FIB) [128]. The interface between the film and SiO₂ substrate is apparent. The coating layer, film and substrate are marked in image (a). The bright zones are due to crystallites in the film. The amorphous phase is predominant with agglomerates of small crystallites embedded in it. Two large columnar structures of crystallites are circled on the image. They are about 37 nm and 22 nm long, parallel to the growth direction of the film. At 50 nm resolution (Figure 8.1b) more columnar crystallites are visible.

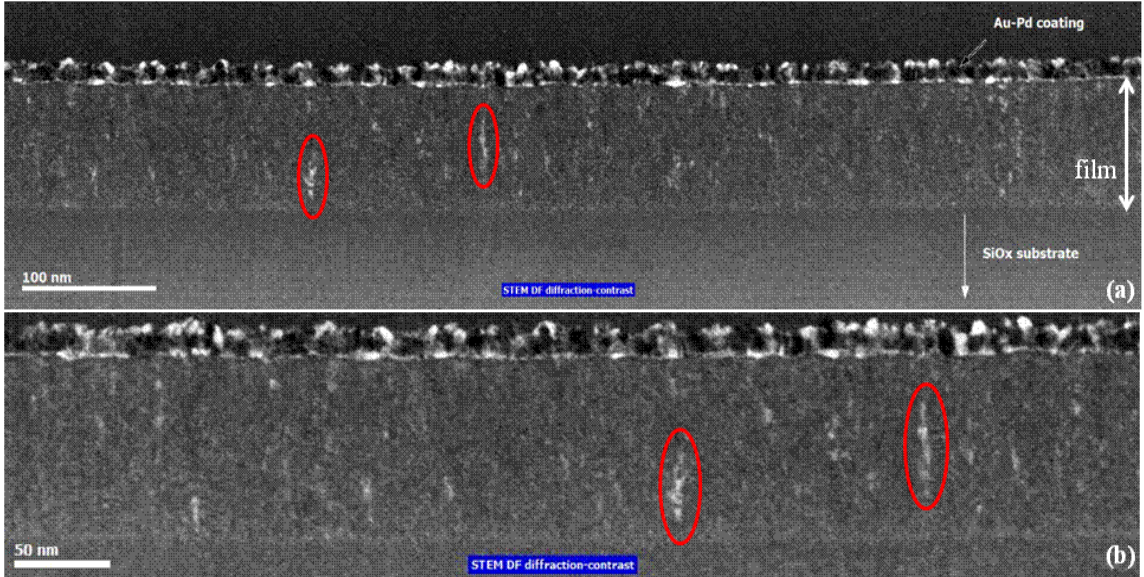


Figure 8.1 Cross sectional dark-field TEM images of sample s58 at 100 nm resolution (a) and 50 nm resolution (b).

Sample s58 was subjected to 10 cycles of CCP deposition and H₂ ICP exposure ($t_1=4$ min and $t_2=6$ min). STEM showed no apparent layered distribution of the crystallites parallel to the surface of the film. A columnar structure along the growth direction was observed, instead. This finding suggests that nano-crystallization did not occur only on the *surface* or *near surface* region of the film, but throughout a substantial *volume* of the film. In the selective etching model of nano-crystallization, the etching rate of the amorphous phase is about 10-20 times faster than that of the crystalline phase [129, 130] and etching takes place on the surface of the film [129]. If that model was operative under the present conditions, a layered distribution of crystallites parallel to the surface of the film should be observed. Instead, the columnar growth of crystallites perpendicular to the film surface suggests that selective etching is not the primary mechanism for nano-crystallization, at least under the present conditions.

Figure 8.2 shows the dark-field images of sample s55 (exposed to 40 min. CCP deposition only) and sample s74_2 (subjected to 120 cycles, with $t_1/t_2=5$ s/20 s).

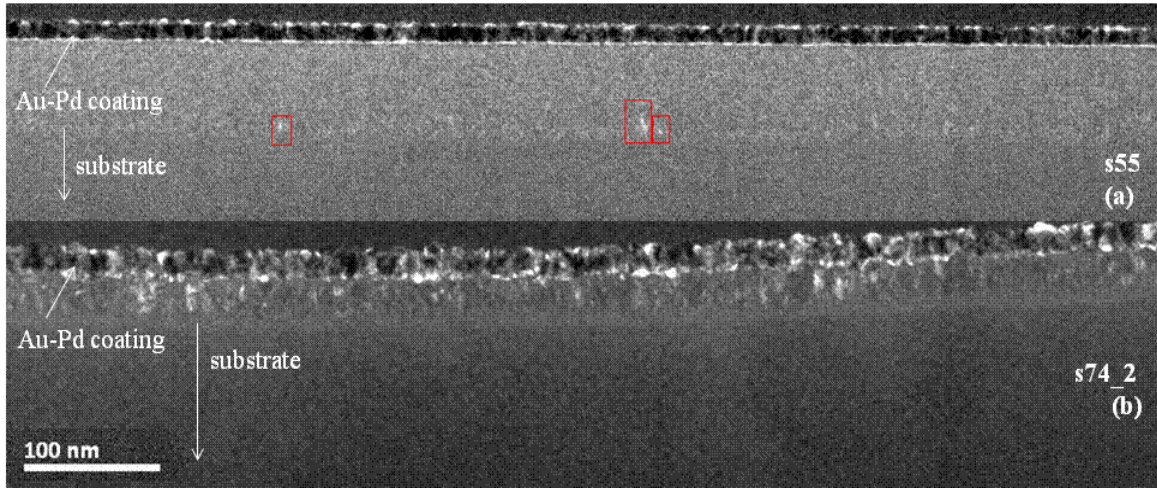


Figure 8.2 Cross sectional TEM dark field images of sample s55 (40 min. CCP deposition only) and sample s74_2 (120 cycles, $t_1/t_2=5$ s/20 s) at 100 nm resolution.

There are a few small crystallites around the interface between the film and the glass substrate in Figure 8.2 (a). These nano-crystallites could be nucleated on some type of contamination on the surface of the glass substrate. No crystallites were found in the bulk of the film. In contrast, for sample s74_2, with 5 s deposition in the CCP and then 20 s exposure to the H₂ ICP (for a total of 120 cycles), a large amount of nano-crystallites was formed as shown by the bright regions in Figure 8.2 (b). The thickness of sample s74_2 measured from the TEM image was around 250 Å and some columnar crystallites traversed the thickness of the film. The columns were wider than those of sample s58. The average width and height of the crystallites as well as the crystalline volume fraction measured from the dark-field TEM images, at 100 nm resolution, are shown in Table 8.1. To obtain more accurate results, the TEM images at 100 nm resolution were separated

into five equal regions along the surface direction and the crystalline volume fraction was calculated for each of these regions. Figure 8.3 is an example for the selection of the crystallites regions.

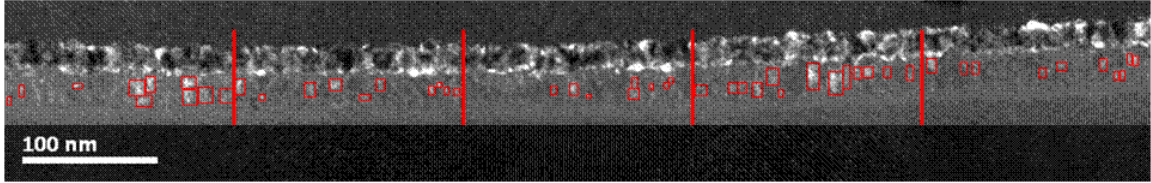


Figure 8.3 The example for the selection of the crystallites under 100 nm resolution of dark-field image (s74_2), the red circles were the regions of crystallites and red lines were used to separate the image into five equal regions.

Table 8.1 Average width and height of the crystallites, crystalline volume fraction, and the number of regions counted on dark-field TEM images of samples s55, s58 and s74_2.

	Average width of nano-crystallites (nm)	Average height of nano-crystallites (nm)	Average crystalline volume fraction	Number of regions counted
s55	3.8 ± 0.74	5.1 ± 0	$0.16\% \pm 0.038\%$	4
s58	3.9 ± 1.0	6.4 ± 3.5	$2.5\% \pm 0.17\%$	48
s74_2	6.2 ± 2.4	8.4 ± 3.3	$13.5\% \pm 0.93\%$	51

Sample s55 had a very small fraction of crystallites in the film. The average width and height of the nano-crystallites of sample s58 were 3.9 nm and 6.4 nm, respectively. These dimensions are comparable with the crystallite size of 5.4 nm, estimated from the Raman spectrum peak shift (see Figure 4.8 in Chapter 4). For sample s74_2, the long columnar structure consisted of crystallites with average width and height of 6.2 nm and 8.4 nm, respectively, again comparable to the crystallite size estimated by Raman spectroscopy.

The thickness of the TEM samples along the direction (say y direction) perpendicular to the cross sectional plane and parallel to the TEM electron beam was about 30~100 nm. Since the whole thickness in the y-direction is projected into a 2-dimensional image, the estimated crystalline volume fraction would be larger than the real (3D) value. The average crystalline volume fraction thus found should represent an upper limit of the actual value. On the other hand, the image contrast was not high enough for very small crystallites to be visible at 100 nm resolution; it was hard to define the fringe pattern of very small crystallites. Therefore, the above calculation could only account for the fraction of relatively large crystallites. Figure 8.4 shows the crystalline volume fraction ($\frac{I_{520}}{I_{480} + I_{510} + I_{520}}$) and crystallite size (from Figure 2.13b) from Raman spectroscopy, compared to those from analysis of TEM images.

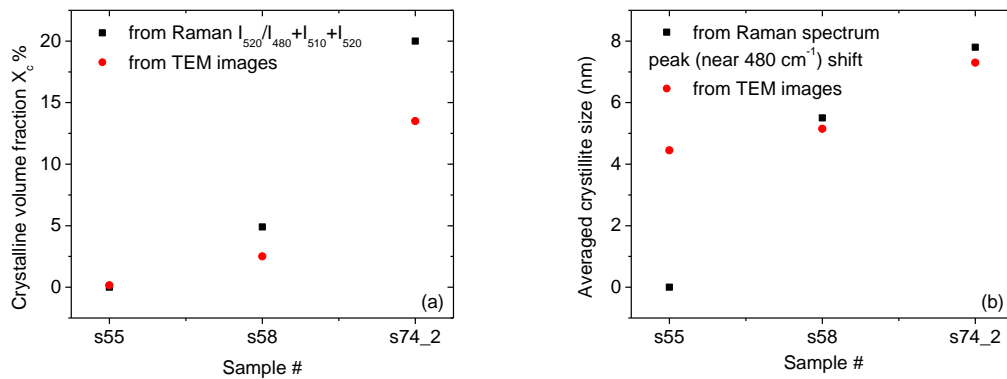


Figure 8.4 Crystalline volume fraction and average crystallite size from Raman spectra and TEM.

Given the uncertainty in the TEM counting method, the volume fractions are in reasonable agreement. The crystallite sizes determined by these methods are also in

agreement, except for sample s55. There were only four regions of nano-crystallites visible in TEM images (which contributed to 0.16% crystalline volume fraction), that did not result in amorphous peak shift in the Raman spectrum.

Figure 8.5 shows bright-field TEM images for samples s55, s56, s58, s73 and s74_2, at 100 nm resolution.

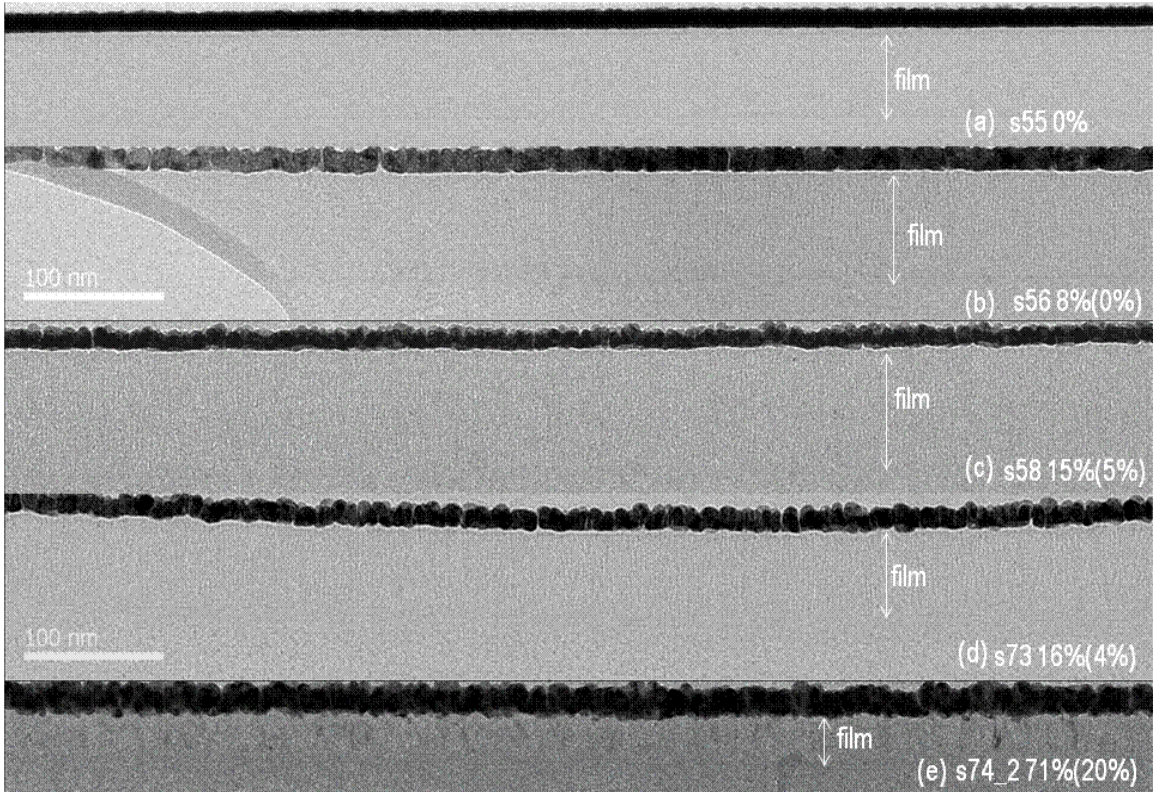
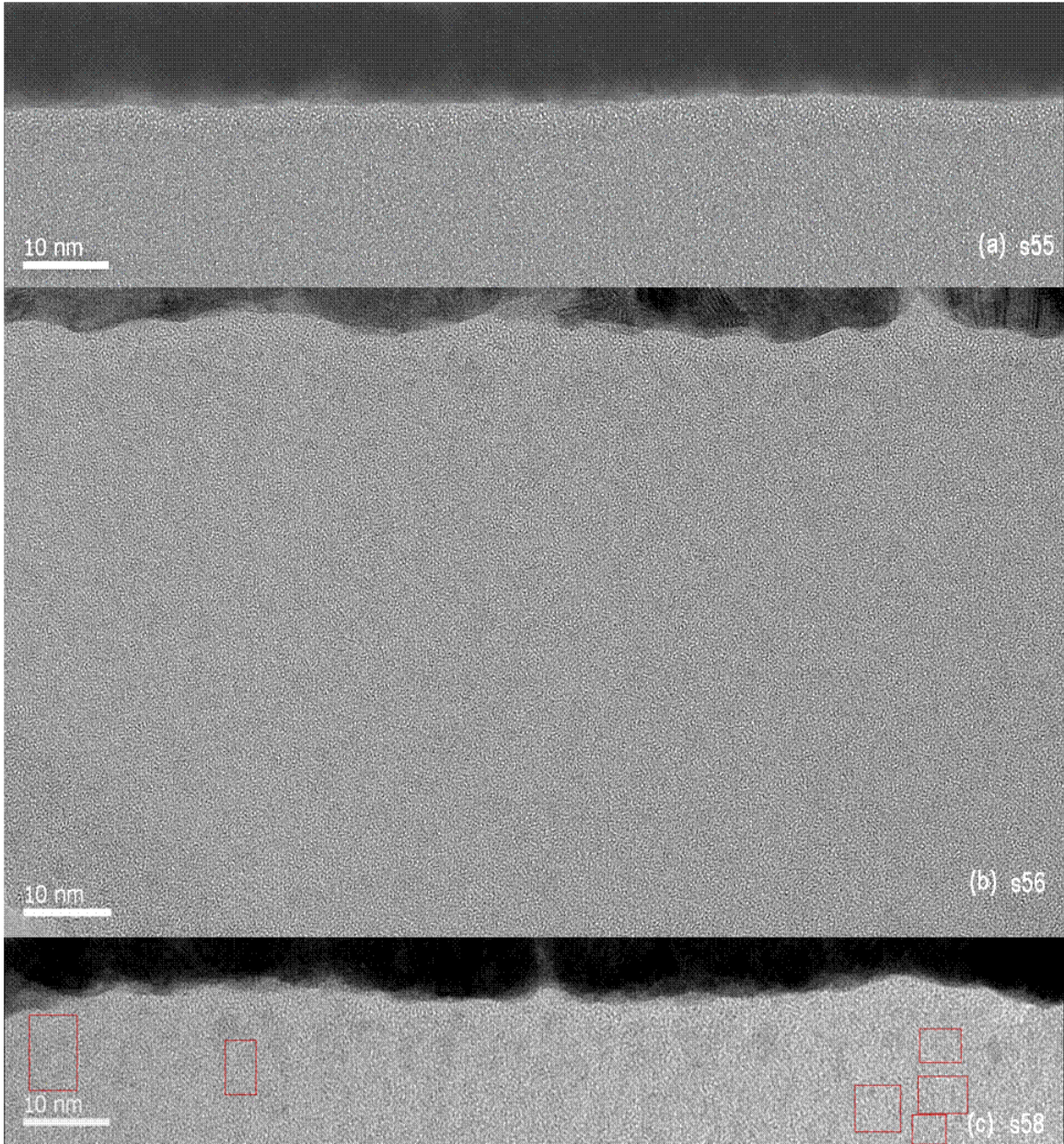


Figure 8.5 Cross sectional TEM bright-field images of samples with different X_c calculated by the three-peak method (two-peak method) from Raman spectra. In each image, the Au-Pd coating and SiO_2 substrate are shown.

Based on the cross-sectional bright-field TEM images, all the samples displayed columnar growth of the crystalline film. Voids are visible between the columns. For the samples with larger values of X_c , columnar growth was more prominent. No crystallites

are detectable at this low resolution. Surface roughness was estimated from the TEM images and compared with the thickness of surface layer (layer #4) estimated by SE (Figure 7.5a). Bright-field TEM images at higher resolution are shown in Figure 8.6.



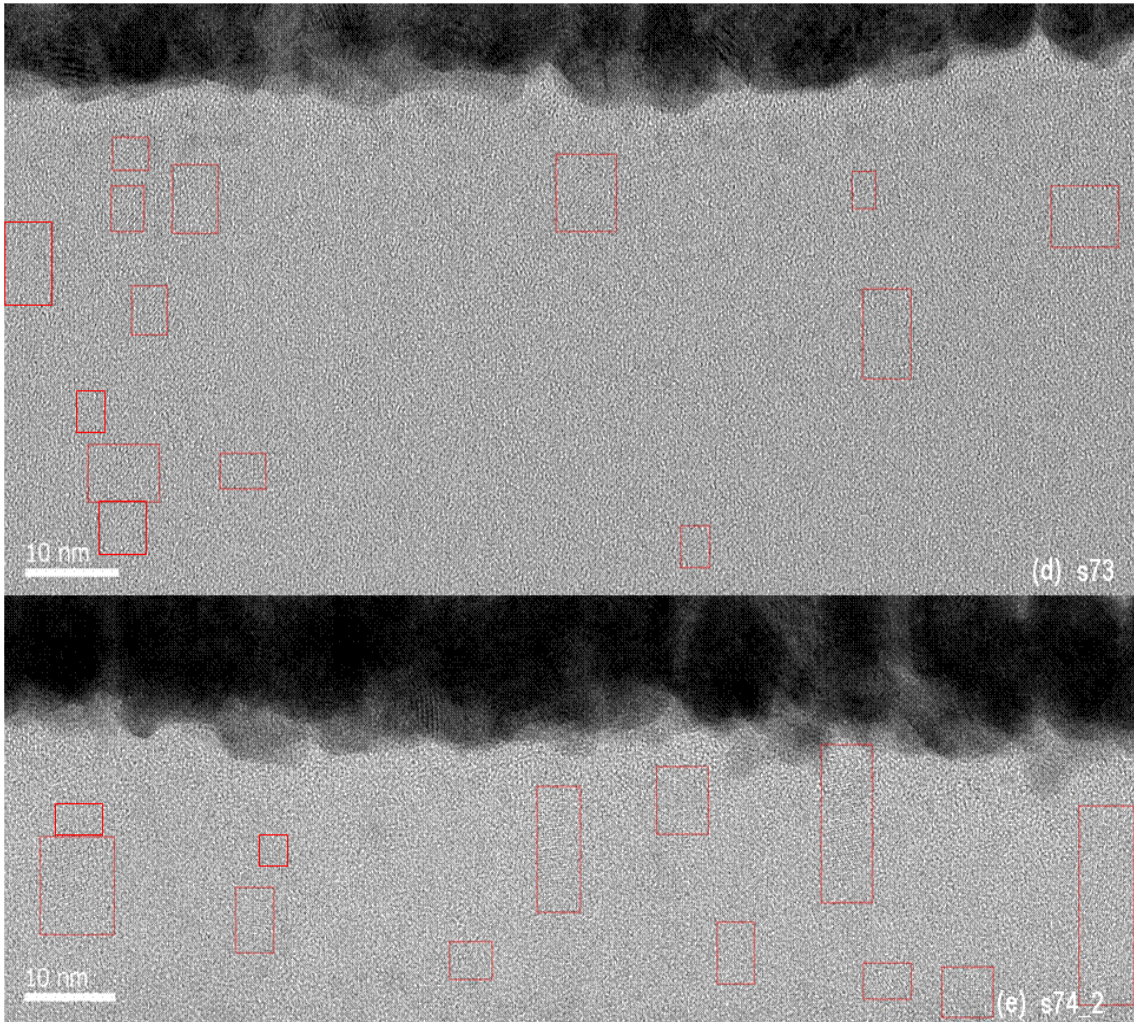


Figure 8.6 High resolution cross sectional TEM bright-field images of different samples. Crystalline regions in samples s58, s73 and s74_2 are enclosed by red rectangles.

High resolution images of samples s55 (only CCP deposition) and s56 (10 cycles, $t_1/t_2=4$ min/3 min) did not show any crystallites. The crystalline planes in the other samples are enclosed in red rectangles. The crystalline volume fraction of sample s56 was 8% by the three-peak Raman method (0% by the two-peak method), which may be too small to be seen in the TEM image. Samples s56 and s58 were both subjected to 10 layer-by-layer process, but sample s58 had longer H₂ ICP process time in each cycle (6 min)

compared to sample s56 (3 min). Small crystallites appeared in sample s58 with 4.5 nm average crystallite size (average length=4.9 nm and average width=4.2, the measurement involved 6 regions). This result was similar with the measurement from dark-field TEM images at 100 nm resolution, which showed 5.1 nm average crystallite size. For the film with the same deposition thickness but longer H₂ ICP exposure, more nano-crystallization occurred through the film, causing more crystallites to form. For shorter deposition time (thinner film) at each cycle, longer and more columnar crystallites were formed in sample s74_2 where the longest crystallite was about 14.6 nm in the TEM image. Nano-crystallization did not only happen on the growth surface but throughout the film, normal to the growth surface. The crystalline volume fraction and the crystallite size depended on both deposited film thickness and H₂ ICP exposure time. In the TEM images, no apparent spherical voids were found. The presence of spherical voids was suggested to be evidence for the “chemical annealing” model [70]. In this model, hydrogen diffused through the film and reacted with Si-H bonds when SiH₄ and H₂ mixing gas was used to deposit nc-Si:H film. Due to the heat generated from this exothermic reaction, the film structure was rearranged, resulting in the formation of free volume and crystalline regions [70].

Chapter 9. Conclusions and Recommendations for Future Work

9.1. Conclusions

Layer-by-layer growth of nano-crystalline Si (nc-Si) films for solar cell applications was investigated. For this purpose, a novel dual-plasma source reactor was designed and built. By utilizing two plasma sources in one vacuum chamber, film deposition and subsequent nano-crystallization were spatially separated. The susceptor was rotated sequentially into a capacitively-coupled plasma (CCP) fed with SiH₄/He gas to deposit an a-Si:H layer, followed by exposure to a H₂ inductively-coupled plasma (ICP) to induce crystallization in the film. The cyclic process was controlled by individually adjusting deposition time (from 40 min, 4 min, 20 s to 5 s per cycle), nano-crystallization time (from 60 min to 5 s per cycle), and number of cycles (1, 10, 120 and 480). Separation of the deposition and crystallization steps provided flexibility in controlling film nanostructure and properties. The films were characterized by Raman spectroscopy, transmission electron microscopy (TEM), Fourier transform infrared (FTIR) spectroscopy and spectroscopic ellipsometry (SE). In addition, the nano-crystallization process was monitored by a mass spectrometer.

The crystalline volume fraction of the films (X_c) ranged from 0% to 72%, which covers the range of crystalline fraction (40%~60%) required for relatively stable solar cells with minimal light-induced degradation [15, 70]. It was found that X_c increased from 0% to 72% by increasing the number of cycles from 1 to 480. Shorter exposure (20 s or 5 s) to the deposition plasma (thinner film per cycle) followed by crystallization in the hydrogen plasma, resulted in higher X_c (e.g. 38% for sample s76 with 120 cycles, $t_1/t_2=2/3$ vs. 12% for sample s69 with 1 cycle, $t_1/t_2=2/3$) and larger crystallite size (e.g. 6.7

nm for s76 vs. 4.5 nm for s69). Also, for the same deposited layer thickness per cycle, longer H₂ plasma exposure resulted in higher X_c (about 2.5 times higher when t_2/t_1 increased from 1/4 to 2/3) and larger crystallite size (increased by 34% when t_2/t_1 increased from 1/4 to 2/3). For given total deposition time (40 min), the crystalline Si peak in the Raman spectrum appeared at lower ratio of H₂ crystallization time to CCP deposition time (i.e., a larger number of cycles), indicating that a thinner film was easier to crystallize. Longer and wider crystallites, found by dark-field TEM, of samples subjected to 480 cycles (thinnest film deposition per cycle) confirmed this finding.

The columnar crystallite structure (along the growth direction) revealed by TEM dark-field imaging suggested that crystallization in the H₂ plasma was not limited to the surface or subsurface region, but it also occurred in the bulk of the film.

The average deposition rate in the CCP plasma was 14 Å/min, determined by SE. For the same *total* deposition time in the CCP reactor, the final film thickness was nearly constant with the change less than 22%, i.e., it was not a function of number of cycles or H₂ ICP exposure time. This finding suggests that etching with etch rate 2.5 Å/min in the H₂ plasma was relatively very slow. X_c , estimated by SE, showed the same trend with that found by Raman spectroscopy, using the two-peak method. However, the absolute values of X_c , estimated by SE, were substantially lower than the Raman values. This is likely due to the presence of very small grain crystallites, which do not register by SE. In addition, the peak dielectric constants determined by SE were blueshifted by about 1 eV. This shift can also be attributed to the presence of small grain crystallites, which do not register in SE.

Mass spectrometry was used to monitor etching products during nano-crystallization in D₂ plasmas. D₂ was used, instead of H₂, to separate H coming from the film from that coming from the plasma. Analysis of the mass signal of SiD₃⁺ gave an estimate of the etching rate=2.5 Å/min at 250 °C. The etched film thickness increased when a thicker film was exposed to the D₂ plasma. In fact, the etching rate was nearly independent of the thickness of the film when it entered the D₂ plasma. This trend suggested that etching did not occur exclusively on the surface or the near-surface region of the film. Finally, the etch rate increased strongly when the substrate temperature was *decreased*, suggesting that D (or H) is lost by diffusion through the film or recombination before it can react to form gaseous silane product, and that these loss processes are thermally activated

FTIR revealed that, as the H₂ plasma exposure time increased, the H content of films *decreased* by 20% while the ratio of SiH₂-to-SiH bonds increased, and this correlated with the increase of the crystalline volume fraction from 0 to 38% in the films. When D₂ was used instead of H₂ in the ICP, with enough D₂ exposure time, the available H in the film was displaced by D. However, the amount of D residing in the film at the end of D₂ plasma exposure was near to 1/3 of the H amount in the film before D₂ plasma exposure.

The dual-plasma source reactor with rotating substrates, built and studied in this work, could also benefit other layer-by-layer processes, such as atomic layer deposition (ALD) and atomic layer etching (ALET). Both of these processes are crucial as device critical dimensions approach monolayer thickness.

9.2. Recommendations for Future Work

(1) To better control the layer-by-layer process, inter-diffusion of gases between the two plasma reactors must be suppressed. The Ar curtain (flow rate 230 sccm) tested in this work reduced diffusion of SiH_4 from the CCP to the ICP plasma by 75%, compared to the case without the Ar curtain. Better separation between the two plasmas could be achieved by:

(i) Replacing the He carrier gas of the CCP feed with Ar. Because Ar is heavier than He, diffusion of the deposition precursor will be slower. Such action will also reduce the huge background signal at 4 AMU (from He diffusing from the CCP to the ICP) which obscured the HD (resulting by abstraction of H from the film by D) signal during mass spectrometric monitoring of the ICP.

(ii) Improving the design for the Ar curtain. Gas flow and mass transfer simulation could be used to improve the design of the Ar curtain, to reduce cross-talk between the gases fed to the two plasmas.

(iii) Using different gas in the ICP. A test using 10%Ar/90% H_2 mixture in the ICP, showed that diffusion of SiH_4 from the CCP to the ICP was significantly reduced, even without the Ar curtain.

(2) To further study the mechanism of nano-crystallization, the H distribution in the film may be measured by secondary ion mass spectroscopy (SIMS). By comparing the H distribution before and after H_2 exposure, H diffusion in the film can be deduced, and the relation between H_2 plasma conditions and nano-crystallization can be better understood.

(3) Substrate temperature monitoring and control can be improved. In the present work, the substrate was underneath the heaters for at least 92% of the total time. Therefore, the difference between the actual substrate temperature and that found by the calibration procedure followed in this study is expected to be small. However, under continuous rotation of the substrates, this calibration procedure is inadequate. In such case, the substrate temperature is a function of the rotation speed of the susceptor. In turn, the kinetics of deposition and nano-crystallization (as well as etching) depends sensitively on substrate temperature. Thus, a more accurate calibration procedure is needed to perform experiments with continuous rotation of the substrate. In that respect, real time monitoring of substrate temperature using a pyrometer, fluoroptic or other non-contact thermometer may prove useful.

References

- [1] L. L. Kazmerski, "Solar photovoltaics R&D at the tipping point: A 2005 technology overview," *Journal of Electron Spectroscopy and Related Phenomena*, vol. 150, pp. 105-135, 2006.
- [2] M. Z. Jacobson, "Review of solutions to global warming, air pollution, and energy security," *Energy Environ. Sci.*, vol. 2, pp. 148-173, 2009.
- [3] C. E. Fritts, "On a New Form of Selenium Cell, and some Electrical Discoveries made by its use," *Am. J. Sci.*, vol. 26, pp. 465-472.
- [4] R. S. Ohl, "Light-sensitive electric device," US Patent No. 2,402,622, May 27, 1941.
- [5] M. A. Green, "The Path to 25% Silicon Solar Cell Efficiency: History of Silicon Cell Evolution," *Prog. Photovolt: Res. Appl.*, vol. 17, pp. 183 - 189, 2009.
- [6] M. A. Green, "Photovoltaic principles," *Physica E*, vol. 14, pp. 11-17, 2002.
- [7] M. D. Chapin, C. S. Fuller, G. L. Pearson, "A New Silicon p-n Junction Photocell for Converting Solar Radiation into Electrical Power," *J. Appl. Phys.*, vol.25, pp. 676-677, 1954.
- [8] X. Deng and E. A. Schiff, "Amorphous silicon-based solar cells," in *Handbook of Photovoltaic Science and Engineering*, 1st ed. Ed., A. Luque and S. Hegedus, England: Wiley, 2003, pp. 505-559.
- [9] Solar generation 6, from European Photovoltaic Industry Association, [Online] <http://www.epia.org/index.php?id=18>.
- [10] Thin-film's Share of Solar Panel Market to Double by 2013, [Online]

<http://www.renewableenergyworld.com/rea/news/article/2009/11/thin-films-share-of-solar-panel-market-to-double-by-2013>.

[11] D. E. Carlson and C. R. Wronski, "Amorphous silicon solar cell," *Appl. Phys. Lett.*, Vol. 28, pp. 671-673, 1976.

[12] M. Vanecek, A. Poruba, Z. Remes, N. Beck and M. Nesladek, "Optical properties of microcrystalline materials," *J. Non-Cryst. Solids*, vol. 227-230, pp. 967-972, 1998.

[13] H. M. Branz, "Hydrogen diffusion and mobile hydrogen in amorphous silicon," *Phys. Rev. B*, vol. 60, pp. 7725-7727, 1999.

[14] D. E. Carlson, C. W. Magee, "A SIMS analysis of deuterium diffusion in hydrogenated amorphous silicon," *Appl. Phys. Lett.*, vol. 33, pp. 81-83, 1978.

[15] F. Meillauda, A. Feltrina, D. Domine, P. Buehlmann, M. Pythona, G. Bugnona, A. Billea, G. Parascandolo, J. Bailatb, S. Faya, N. Wyrsha, C. Ballifa and A. Shah, "Limiting factors in the fabrication of microcrystalline silicon solar cells and microcrystalline/amorphous ('micromorph') tandems," *Phil. Mag.*, vol. 89, pp. 2599-2621, 2009.

[16] M. Vanecek, A. Poruba, Z. Remes, J. Rosa, S. Kamba, V. Vorlicek, J. Meier, A. Shah, "Electron spin resonance and optical characterization of defects in microcrystalline silicon," *J. Non-Cryst. Solids*, vol. 266-269, pp. 519-523, 2000.

[17] G. Yue, B. Yan, G. Ganguly, J. Yang, and S. Guha, "Metastability in hydrogenated nanocrystalline silicon solar cells," *J. Mater. Res.*, vol. 22, pp. 1128-1137, 2007.

[18] J. R. Abelson, "Plasma deposition of hydrogenated amorphous silicon: Studies of the growth surface," *Appl. Phys. A*, vol. 56, pp. 493-512, 1993.

- [19] A. Matsuda, "Formation kinetics and control of microcrystallite in $\mu\text{-Si:H}$ from glow discharge plasma," *J. Non-Cryst. Solids*, vol. 59 & 60, pp. 767-774, 1983.
- [20] S. Sriraman, M. S. Valipa, E. S. Aydil, and D. Maroudas, "Hydrogen-induced crystallization of amorphous silicon thin films. I. Simulation and analysis of film postgrowth treatment with H_2 plasmas," *J. Appl. Phys.*, vol. 100, pp. 053514, 2006.
- [21] M. S. Valipa, S. Sriraman, E. S. Aydil, and D. Maroudas, "Hydrogen-induced crystallization of amorphous Si thin films. II. Mechanisms and energetics of hydrogen insertion into Si-Si bonds," *J. Appl. Phys.*, vol. 100, pp. 053515, 2006.
- [22] S. Agarwal, A. Takano, M. C. M. v. d. Sanden, D. Maroudas, and E. S. Aydil, "Abstraction of atomic hydrogen by atomic deuterium from an amorphous hydrogenated silicon surface," *J. Chem. Phys.*, vol. 117, pp. 10805-10816, 2002.
- [23] D. C. Marra, E. A. Edelberg, R. L. Naone and E. S. Aydil, "Silicon hydride composition of plasma-deposited hydrogenated amorphous and nanocrystalline silicon films and surfaces," *J. Vac. Sci. Technol. A*, vol. 16, pp. 3199-3210, 1998.
- [24] M. Vanecek, A. Poruba, Z. Remes, N. Beck and M. Nesladek, "Optical properties of microcrystalline materials," *J. Non-Cryst. Solids*, vol. 227-230, pp. 967-972, 1998.
- [25] E. Srinivasan and G. N. Parsons, "Hydrogen abstraction kinetics and crystallization in low temperature plasma deposition of silicon," *Appl. Phys. Lett.*, vol. 72, pp. 456-458, 1998.
- [26] H. Shirai, J. Hanna and I. Shimizu, "A novel preparation technique termed "Chemical annealing" to make a rigid and stable Si-network," *Mat. Res. Soc. Symp. Proc.*, vol. 219, pp. 643-653, 1991.

- [27] H. Shirai, B. Drevillon and I. Shimizu, "Role of hydrogen plasma during growth of hydrogenated microcrystalline silicon: In situ UV- visible and infrared ellipsometry study," *Jpn. J. Appl. Phys.*, vol. 33, pp. 5590-5598, 1994.
- [28] S. Bouladakis, S. Logothetidis, S. Ves and J. Kircher, "Optical properties of $\mu\text{c-Si:H/a-Si:H}$ layered structures: Influence of the hydrogen bonds, crystallite size, and thickness," *J. Appl. Phys.*, vol. 73, pp. 914-925, 1993.
- [29] A. Asano, "Effects of hydrogen atoms on the network structure of hydrogenated amorphous and microcrystalline silicon thin films," *Appl. Phys. Lett.*, vol. 56, pp. 533-535, 1990.
- [30] A. Asano, T. Ichimura and H. Sakai, "Preparation of highly photoconductive hydrogenated amorphous silicon carbide films with a multiplasma-zone apparatus," *J. Appl. Phys.*, vol. 65, pp. 2439-2444, 1989.
- [31] H. Dersch, J. Stuke, and J. Beichler, "Light-induced dangling bonds in hydrogenated amorphous silicon," *Appl. Phys. Lett.*, vol. 38, pp. 456-458, 1980.
- [32] H. Fritzsche, "Development in understanding and controlling the Staebler-Wronski effect in a-Si:H," *Annu. Rev. Mater. Res.*, vol. 31, pp. 47-79, 2001.
- [33] J. A. Reimer, R. W. Vaughan and J. C. Knights, "Proton Magnetic Resonance Spectra of Plasma-Deposited Amorphous Si: H Films," *Phys. Rev. Lett.*, vol. 44, pp. 193-196, 1980.
- [34] R. A. Street, "Hydrogenated amorphous silicon," Cambridge University Press, Cambridge, 1991, pp. 4-13.
- [35] W, Ke, X. Feng and Y. Huang, "The effect of Si-nanocrystal size distribution on Raman spectrum," *J. Appl. Phys.*, vol.109, pp. 083526-083531, 2011.

- [36] K. Takahashi and M. Konagai, "Amorphous silicon solar cells," John Wiley & Sons, New York, 1986, pp. 106-109.
- [37] M. A. Lieberman and A. J. Lichtenberg, "Principles of plasma discharges and materials processing," 2nd ed., John Wiley & Sons, Hoboken, New Jersey, 2005, pp. 619-630.
- [38] R. E. I. Schropp and M. Zeman, "Amorphous and microcrystalline silicon solar cell: modeling, materials and device technology," Kluwer Academic Publishers, Norwell, 1998, pp. 99-112.
- [39] M. J. Kushner, "A model for the discharge kinetics and plasma chemistry during plasma enhanced chemical vapor deposition of amorphous silicon," *J. Appl. Phys.*, vol. 63, pp. 2532-2551, 1988.
- [40] A. Gallagher, "Neutral radical deposition from silane discharge," *J. Appl. Phys.*, vol. 63, pp. 2406-2413, 1988.
- [41] M. J. McCaughey and M. J. Kushner, "Simulation of the bulk and surface properties of amorphous hydrogenated silicon deposited from silane plasmas," *J. Appl. Phys.*, vol. 65, pp. 186-195, 1989.
- [42] J. Perrin, Y. Takeda, N. Hirano, Y. Takeuchi and A. Matsuda, "Sticking and recombination of the SiH₃ radical on hydrogenated amorphous silicon: The catalytic effect of diborane," *Surf. Sci.*, vol. 210, pp. 114-128, 1989.
- [43] G. J. Nienhuis, W. J. Goedheer, E. A. G. Hamers, W. G. J. H. M. van Sark and J. Bezemer, "A self-consistent fluid model for radio-frequency discharges in SiH₄ - H₂ compared to experiments," *J. Appl. Phys.*, vol. 82, pp. 2060-2071, 1997.

- [44] H. Chatham, P. Bhat, A. Benson and C. Matovich, "High-efficiency amorphous silicon p-i-n solar cells deposited from disilane at rates up to 2 nm/s using VHF discharges," *J. Non-Cryst. Solids*, vol. 115, pp. 201-203, 1989.
- [45] S. Veprek, F. –A. Sarrott, S. Rambert and E. Taglauer, "Surface hydrogen content and passivation of silicon deposited by plasma induced chemical vapor deposition from silane and the implications for the reaction mechanism," *J. Vac. Sci. Technol. A*, vol. 7, pp. 2614-2624, 1989.
- [46] M. Otake and S. Oda, "Preparation of microcrystalline silicon films by very-high-frequency digital chemical vapor deposition," *Jpn. J. Appl. Phys.*, vol. 31, pp. 1948-1952, 1992.
- [47] J. J. Schellenberg, R. D. McLeod, S. R. Mejia, H. C. Card and K. C. Kao, "Microcrystalline to amorphous transition in silicon from microwave plasmas," *Appl. Phys. Lett.*, vol. 48, pp. 163-164, 1986.
- [48] M. Kondo, Y. Toyoshima, A. Matsuda and K. Ikuta, "Substrate dependence of initial growth of microcrystalline silicon in plasma-enhanced chemical vapor deposition," *J. Appl. Phys.*, vol. 80, pp. 6061-6063, 1996.
- [49] H. Wiesmann, A. K. Ghosh, T. McMahon and M. Strongin, "a-Si:H produced by high-temperature thermal decomposition of silane," *J. Appl. Phys.*, vol. 50, pp. 3752-3754, 1979.
- [50] A. H. Mahan, R. C. Reedy, E. Iwaniczko, Q. Wang, B. P. Nelson, Y. Xu, A. C. Gallagher, H. M. Branz, R. S. Crandall, J. Yang and S. Guha, "H out-diffusion and device performance in n-i-p solar cells utilizing high temperature hot wire a-Si:H i-layers," in *Amorphous and Microcrystalline Silicon Technology - 1998*, Ed., R. Schropp, H. Branz, S. Wagner, M. Hack and I. Shimizu, *Materials Research Society Symp. Proc.*, vol. 507, pp. 119-124, 1998.

- [51] A. H. Mahan, J. Carapella, B. P. Nelson and R. S. Crandall, "Deposition of device quality, low H content amorphous silicon," *J. Appl. Phys.*, vol. 69, pp. 6728-6730, 1991.
- [52] H. Matsumura, "Formation of Polysilicon Films by Catalytic Chemical Vapor Deposition (cat-CVD) Method," *Jpn. J. Appl. Phys.*, vol. 30, pp. L1522-L1524, 1991.
- [53] R.E.I. Schropp and J. K. Rath, "Novel profiled thin-film polycrystalline silicon solar cells on stainless steel substrates," *IEEE Transactions on Electron Devices*, vol. 46, pp. 2069-2071, 1999.
- [54] K. F. Feenstra, C. H. M. van der Werf, E. C. Molenbroek and R.E.I. Schropp, "Deposition of device quality amorphous silicon by hot-wire CVD," in *Amorphous and Microcrystalline Silicon Technology - 1997*, Ed., S. Wagner, M. Hack, E. A. Schiff, R. Schropp and I. Shimizu, *Materials Research Society Symp. Proc.*, vol. 467, pp. 645-650, 1997.
- [55] D. L. Staebler and C. R. Wronski, "Reversible conductivity changes in discharge-produced amorphous Si," *Appl. Phys. Lett.*, vol. 31, pp. 292-294, 1977.
- [56] D. L. Staebler and C. R. Wronski, "Optically induced conductivity changes in discharge-produced hydrogenated amorphous silicon," *J. Appl. Phys.*, vol. 51, pp. 3262-3268, 1980.
- [57] D. Adler, M.E. Eberhart, K.H. Johnson and S.A. Zygmunt, "Metastable defects in amorphous silicon alloys," *J. Non-Cryst. Solids*, vol. 66, pp. 273-278, 1984.
- [58] M. Stutzmann, "Weak Bond-Dangling Bond Conversion in Amorphous Silicon," *Philos. Mag. B*, vol. 56, pp. 63-70, 1987.
- [59] R. S. Crandall, D. E. Carlson, A. Catalano and H. A. Weakliem, "Role of carbon in hydrogenated amorphous silicon solar cell degradation," *Appl. Phys. Lett.*, vol. 44, pp. 200-201, 1984.

- [60] A. Yelon, H. Fritzsche and H. M. Branz, "Electron beam creation of metastable defects in hydrogenated amorphous silicon: hydrogen collision model," *J. Non-Cryst. Solids*, vol. 266-269, pp. 437-443, 2000.
- [61] C. V. Sanchez, "Thin film nanocrystalline silicon solar cells obtained by hot-wire CVD," Ph. D. Thesis, University of Barcelona, Barcelona, Gener, 2001.
- [62] K. M. A. Rahman, "Nanocrystalline silicon solar cells deposited via pulsed PECVD at 150oC substrate temperature," M. S. Thesis, University of Waterloo, Waterloo, Ontario, Canada, 2010.
- [63] J. Meier, R. Fluckiger, H. Keppner and A. Shah, "Complete microcrystalline p-i-n solar cell—Crystalline or amorphous cell behavior?" *Appl. Phys. Lett.*, vol. 65, pp. 860-862, 1994.
- [64] J. Meier, S. Dubail, R. Platz, P. Torres, U. Kroll, J. A. Anna Selvan, N. Pellaton Vaucher, Ch. Hof, D. Fischer, H. Keppner, R. Fluckiger, A. Shah, V. Shklover and K.-D. Ufert, "Towards high-efficiency thin-film silicon solar cells with the "micromorph" concept," *Sol. Energ. Mater. Sol. Cells*, vol. 49, pp. 35-44, 1997.
- [65] H. Keppner, J. Meier, P. Torres, D. Fischer and A. Shah, "Microcrystalline silicon and micromorph tandem solar cells," *Appl. Phys. A*, vol. 69, pp. 169-177, 1999.
- [66] P. St'ahel, S. Hamma, P. Sladek, P. Roca i Cabarrocas, "Metastability studies in silicon thin films: from short range ordered to medium and long range ordered materials," *J. Non-Cryst. Solids*, vol. 227-230, pp. 276-280, 1998.
- [67] B. Yan, G. Yue, J. M. Owens, J. Yang, and S. Guha, "Light-induced metastability in hydrogenated nanocrystalline silicon solar cells," *Appl. Phys. Lett.*, vol. 85, pp. 1925-1927, 2004.

- [68] G. Yue, B. Yan, G. Ganguly, J. Yang, S. Guha and C. W. Teplin, "Material structure and metastability of hydrogenated nanocrystalline silicon solar cells," *Appl. Phys. Lett.*, vol. 88, pp. 263507, 2007.
- [69] B. Yan, G. Yue, J. Yang, S. Guha, D. L. Williamson, D. Han and C. Jiang, "Hydrogen dilution profiling for hydrogenated microcrystalline silicon solar cells," *Appl. Phys. Lett.*, vol. 85, pp. 1955-1957, 2004.
- [70] L. Houben, M. Luysberg, P. Hapke, R. Carius, F. Finger and H. Wagner, "Structural properties of microcrystalline silicon in the transition from highly crystalline to amorphous growth," *Phil. Mag. A*, vol. 77, pp. 1447-1460, 1998.
- [71] S. Veprek, "Statistical Model of Chemical Reactions in Nonisothermal Low Pressure Plasma," *J. Chem. Phys.*, vol. 57, pp. 952-959, 1972.
- [72] A. Matsuda, "Amorphous and Microcrystalline Silicon," in Springer Handbook of Electronic and Photonic Materials, Ed., S. Kasap and P. Capper, Springer US, July 2007, pp. 581-595.
- [73] K. L. Chopra, *Thin Film Phenomena*, McGraw-Hill, New York, 1969, Chapter IV.
- [74] M. Nakamura, T. Ohno, K. Miyata, N. Konishi and T. Suzuki, "Hydrogenation kinetics and defect termination of postplasma-treated chemical-vapor-deposited amorphous silicon film," *J. Appl. Phys.*, vol. 65, pp. 3061-3068, 1989.
- [75] N. Layadi, P. Roca i Cabarrocas, B. Drevillon and I. Solomon, "Real-time spectroscopic ellipsometry study of the growth of amorphous and microcrystalline silicon thin films prepared by alternating silicon deposition and hydrogen plasma treatment," *Phys. Rev. B*, vol. 52, pp. 5136-5143, 1995.

- [76] M. Katiyar and J. R. Abelson, "Investigation of hydrogen induced phase transition from a-Si:H to mc-Si:H using real time infrared spectroscopy," *Mater. Sci. Eng., A*, vol. 304-306, pp. 349-352, 2001.
- [77] J. Perrin, "Plasma and surface reactions during a-Si:H film growth," *J. Non-Cryst. Solids*, vol. 137&138, pp. 639-644, 1991.
- [78] G. Cheng, H. Xia, K. Chen, W. Zhang and X. Zhang, "Raman measurement of the grain size for silicon crystallites," *Phys. Stat. Sol. A*, vol. 118, pp. K51-K54, 1990.
- [79] M. Cardona, "Folded, confined, interface, surface, and slab vibrational modes in semiconductor superlattices," *Superlattices and Microstruct.*, vol. 5, pp. 27-42, 1989.
- [80] V. Vavrunikova, G. V. Elzaker, M. Zeman and P. Sutta, "Medium-range order in a-Si:H films prepared from hydrogen diluted silane," *Phys. Status Solidi A*, vol. 207, pp. 548-551, 2010.
- [81] H. Xia, Y. L. He, L. C. Wang, W. Zhang, X. N. Liu, X. K. Zhang, D. Feng and H. E. Jackson, "Phonon mode study of Si nanocrystals using micro-Raman spectroscopy," *J. Appl. Phys.*, vol. 78, pp. 6705-6708, 1995.
- [82] Q. Cheng, S. Xu and K. Ostrikov, "Structural evolution of nanocrystalline silicon thin films synthesized in high-density, low-temperature reactive plasma," *Nanotechnology*, vol. 20, pp. 215606, 2009.
- [83] S. Veprek, F. -A. Sarott and Z. Iqbal, "Effect of grain boundaries on the Raman spectra, optical absorption, and elastic light scattering in nanometer-sized crystalline silicon," *Phys. Rev. B*, vol. 36, pp. 3344-3350, 1987.
- [84] E. Bustarret, A. Deneu'ille, R. Grosleau, L C. Brunel, and M. Brunei, "Residual disorder in low-temperature polycrystalline silicon," *J. Electron. Mater.*, vol. 13, pp. 673-687, 1984.

- [85] E. Bustarret, M. A. Hachicha and M. Brunel, "Experimental determination of the nanocrystalline volume fraction in silicon thin films from Raman spectroscopy," *Appl. Phys. Lett.*, vol. 52, pp. 1675-1677, 1988.
- [86] R. Tsu, H. Shen, and M. Dutta, "Correlation of Raman and photoluminescence spectra of porous silicon," *Appl. Phys. Lett.*, vol. 60, pp. 112-114, 1992.
- [87] S. Veprek, Z. Iqbal, H. R. Oswald, F. -A. Sarott, J. J. Wagner and A. P. Webb, "Lattice dilatation of small silicon crystallites - implications for amorphous silicon," *Solid State Commun.*, vol. 39, pp. 509-512, 1981.
- [88] Z. Iqbal, S. Veprek, A. P. Webb and P. Capezzuto, "Raman scattering from small particle size polycrystalline silicon," *Solid State Commun.*, vol. 37, pp. 993-996, 1981.
- [89] Z. Iqbal and S. Veprek, "Raman scattering from hydrogenated microcrystalline and amorphous silicon," *J. Phys. C: Solid State Phys.*, vol. 15, pp. 377-392, 1982.
- [90] C. Manfredotti, F. Fizzotti, M. Boero, P. Pastorino, P. Polesello, and E. Vittone, "Influence of hydrogen-bonding configurations on the physical properties of hydrogenated amorphous silicon," *Phys. Rev. B*, vol. 50, pp. 18046-18053, 1994.
- [91] M. H. Srodsky, Manuel Cardona and J. J. Cuomo, "Infrared and Raman spectra of the silicon-hydrogen bonds in amorphous silicon prepared by glow discharge and sputtering," *Phys. Rev. B*, vol. 16, pp.3556-3571, 1977.
- [92] E. Srinivasan, D. A. Lloyd and G. N. Parsons, "Dominant monohydride bonding in hydrogenated amorphous silicon thin films formed by plasma enhanced chemical vapor deposition at room temperature," *J. Vac. Sci. Technol. A*, vol. 15, pp. 77-84, 1997.

- [93] P. R. i Cabarrocas, S. Hamma, S. N. Sharma, G. Viera, E. Bertran and J. Costa, "Nanoparticle formation in low-pressure silane plasmas: bridging the gap between a-Si:H and μ -Si films," *J. Non-Cryst. Solids*, vol. 227-230, pp. 871-875, 1998.
- [94] S. Hamma and P. R. i Cabarrocas, "In situ correlation between the optical and electrical properties of thin intrinsic and n-type microcrystalline silicon films," *J. Appl. Phys.*, vol. 81, pp. 7282-7288, 1997.
- [95] P. G. Snyder, Y. Xiong, J. A. Woollam, E. R. Krosche and Y. Strausser, "Characterization of polycrystalline silicon thin-film multilayers by variable angle spectroscopic ellipsometry," *Surf. Interface Anal.*, vol. 18, pp. 113-118, 1992.
- [96] G. E. Jellison, Jr., M. F. Chisholm and S. M. Gorbakkin, "Optical functions of chemical vapor deposited thin-film silicon determined by spectroscopic ellipsometry," *Appl. Phys. Lett.*, vol. 62, pp. 3348-3350, 1993.
- [97] G. E. Jellison, Jr., M. Keefer and L. Thornquist, "Spectroscopic ellipsometry and interference reflectometry measurements of CVD silicon grown on oxidized silicon," *Mater. Res. Soc. Symp. Proc.*, vol. 283, pp. 561-566, 1993.
- [98] A. Daunois and D. E. Aspnes, "Electroreflectance and ellipsometry of silicon from 3 to 6 eV," *Phys. Rev. B*, vol. 18, pp. 1824-1839, 1978.
- [99] A. Hadjadj, N. Pham, P. R. i Cabarrocas, O. Jbara and G. Djellouli, "Ellipsometry investigation of the amorphous-to-microcrystalline transition in a-Si:H under hydrogen-plasma treatment," *J. Appl. Phys.*, vol. 107, pp. 083509, 2010.
- [100] P. Poodt, D. C. Cameron, E. Dickey, S. M. George, V. Kuznetsov, G. N. Parsons, F. Roozeboom, G. Sundaram and A. Vermeer, "Spatial atomic layer deposition: A route towards

further industrialization of atomic layer deposition,” *J. Vac. Sci. Technol. A*, vol. 30, pp. 010802, 2012.

[101] P. Poodt , A. Lankhorst , F. Roozeboom , K. Spee , D. Maas and A. Vermeer, “High-speed spatial atomic-layer deposition of aluminum oxide layers for solar cell passivation,” *Adv. Mater.*, vol. 22, pp. 3564-3567, 2010.

[102] J. Sun, “PECVD, spatial ALD, and PEALD zinc oxide thin film transistors,” Ph. D. Thesis, Pennsylvania state university, Ann Arbor, MI, 2008.

[103] R. Reuter, D. Ellerweg, A. von Keudell and J. Benedikt, “Surface reactions as carbon removal mechanism in deposition of silicon dioxide films at atmospheric pressure,” *Appl. Phys. Lett.*, vol. 98, pp. 111502, 2011.

[104] T. Suntola and J. Antson, “Method for producing compound thin films,” US patent 4,058,430, 1977.

[105] B. Strahm, A. A. Howling, L. Sansonnens and Ch. Hollenstein, “Plasma silane concentration as a determining factor for the transition from amorphous to microcrystalline silicon in SiH₄/H₂ discharges,” *Plasma Source Sci. Technol.*, vol. 16, pp. 80-89, 2007.

[106] V. I. Kolobov, L. D. Tsendin, “Analytic model of the hollow cathode effect,” *Plasma Source Sci. Technol.*, vol. 4, pp. 551-560, 1995.

[107] K. Bhattacharya, D. Das, “Effect of deposition temperature on the growth of nanocrystalline silicon network from helium diluted silane plasma,” *J. Phys. D: Appl. Phys.*, vol. 41, pp. 155420, 2008.

[108] G. Turban, Y. Catherine and B. Grolleau, “A study of the silane glow discharge deposition by isotopic labeling,” *Thin solid films*, vol. 77, pp.287-300, 1981.

- [109] J. A. Glass, Jr., E. A. Wovchko and J. T. Yates, "Reaction of atomic hydrogen with hydrogenated porous silicon - detection of precursor to silane formation," *Jr., Surf. Sci.*, vol. 348, pp. 325-334, 1996.
- [110] H. Qian, Q. Zhu and H. Ma, "High-resolution spectroscopy of ν_3 , and $\nu_1 + \nu_3$, bands of SiD_4 ," *Chem. Phys. Lett.*, vol. 192, pp. 338-347, 1992.
- [111] L. Halonen and M. S. Child, "A local mode model for tetrahedral molecules," *Mol. Phys.*, vol. 46, pp. 239-255, 1982.
- [112] H. W. Kattenberg and A. Oskam, "Infrared and Laser Raman Gas Spectra of SiH_4 and SiD_4 ," *J. Mol. Spectrosc.*, vol. 49, pp. 52-69, 1974.
- [113] J. Perrin and J. F. M. Aarts, "Dissociative excitation of SiH_4 , SiD_4 , Si_2H_6 and GeH_4 by 0–100 eV electron impact," *Chem. Phys.*, vol. 80, pp. 351-365, 1983.
- [114] S. Veprek, C. Wang and M. G. J. Veprek-Heijman, "Role of oxygen impurities in etching of silicon by atomic hydrogen," *J. Vac. Sci. Technol. A*, vol. 26, pp. 313-320, 2008.
- [115] S. Veprek and F. –A. Sarott, "Electron-impact-induced anisotropic etching of silicon by hydrogen," *Plasma Chem. Plasma Process*, vol. 2, pp. 233-246, 1982.
- [116] T. Yasuda and D. E. Aspnes, "Optical-standard surfaces of single-crystal silicon for calibrating ellipsometers and reflectometers," *Appl. Opt.*, vol. 33, pp. 7435-7438, 1994.
- [117] P. R. I Cabarrocas, N. Layadi, B. Drevillon and I. Solomon, "Microcrystalline silicon growth by the layer-by-layer technique: long term evolution and nucleation mechanisms," *J. Non-Cryst. Solids*, vol. 198-200, pp. 871-874, 1996.
- [118] D. E. Aspnes, "Optical properties of thin films," *Thin Solid Film*, vol. 89, pp. 249-262, 1982.

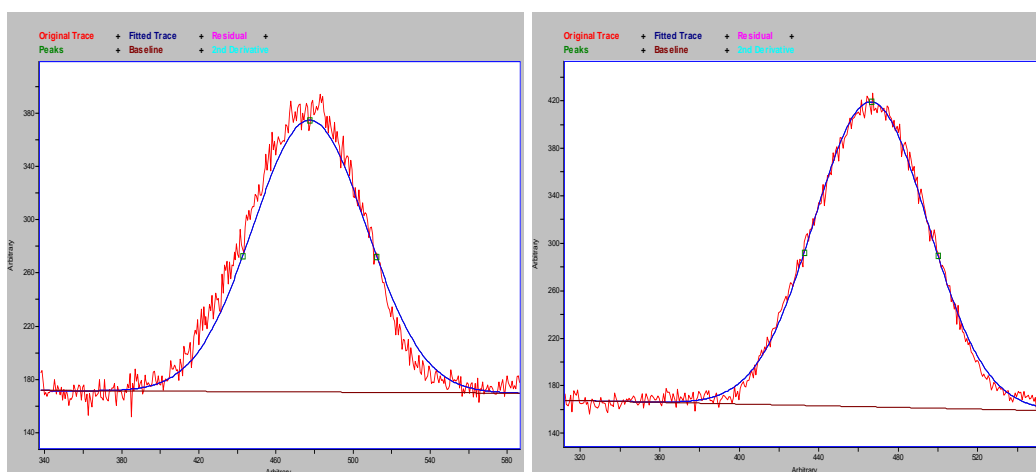
- [119] C. M. Herzinger, B. Johs, W. A. McGahan and J. A. Woollam, "Ellipsometric determination of optical constants for silicon and thermally grown silicon dioxide via a multi-sample, multi-wavelength, multi-angle investigation," *J. Appl. Phys.*, vol. 83, pp. 3323-3336, 1998.
- [120] A.S.Ferlauto, G. M. Ferreira¹, J. M. Pearce¹, C. R. Wronski¹, R. W. Collins, X. Deng and G. Ganguly, "Analytical model for the optical functions of amorphous semiconductors from the near-infrared to ultraviolet: Applications in thin film photovoltaics", *J. Appl. Phys.*, vol. 92, pp. 2424-2436, 2002.
- [121] F. Hiroyuki, *Spectroscopic ellipsometry : principles and applications*, Chichester, England, Hoboken, NJ : John Wiley & Sons, 2007.
- [122] WVASE32 manual, J. A. Woollam Co., Inc., New York, NY.
- [123] J. Leng, J. Opsal, H. Chu, M. Senko and D. E. Aspnes, "Analytic representations of the dielectric functions of crystalline and amorphous Si and crystalline Ge for very large scale integrated device and structural modeling", *J. Vac. Sci. Technol. A*, vol. 16, pp. 1654-1657, 1998.
- [124] D. E. Aspnes, A. A. Studna and E. Kinsbron, "Dielectric properties Of heavily doped crystalline and amorphous silicon from 1.5 to 6.0 eV", *Phy. Rev. B*, vol. 29, pp. 768-779, 1984.
- [125] G. E. Jellison and F. A. Modine, "Parameterization of the optical functions of amorphous materials in the interband region", *Appl. Phys. Lett.*, vol. 69, pp. 371-373, 1996.
- [126] S. Boultdakis, S. Logothetidis, S. Ves, and J. Kircher, "Optical properties of $\mu\text{c-Si:H/a-Si:H}$ layered structures: Influence of the hydrogen bonds, crystallite size, and thickness", *J. Appl. Phys.*, vol. 73, pp. 914-925, 1993.

- [127] M. Pinarbasi, N. Maley, A. Myers, J.R. Abelson, "Hydrogenated amorphous silicon films deposited by reactive sputtering: The electronic properties, hydrogen bonding and microstructure", *Thin Solid Films*, vol. 171, pp. 217-233, 1989.
- [128] B. W. Kempshall, L. A. Giannuzzi, B. I. Prenzler and F. A. Stevie and S. X. Da, "Comparative evaluation of protective coatings and focused ion beam chemical vapor deposition processes", *J. Vac. Sci. Technol. B*, vol. 20, pp. 286-290, 2002.
- [129] I. Solomon, B. Drévilion, H. Shirai and N. Layadi, "Plasma deposition of microcrystalline silicon: the selective etching model", *J. Non-Cryst. Solids*, vol. 164 & 166, pp. 989-992, 1993.
- [130] C. C. Tsai, G. B. Anderson, R. Thompson and B. Wacker, "Control of silicon network structure in plasma deposition," *J. Non-Cryst. Solids*, vol. 114, pp. 151-153, 1989.

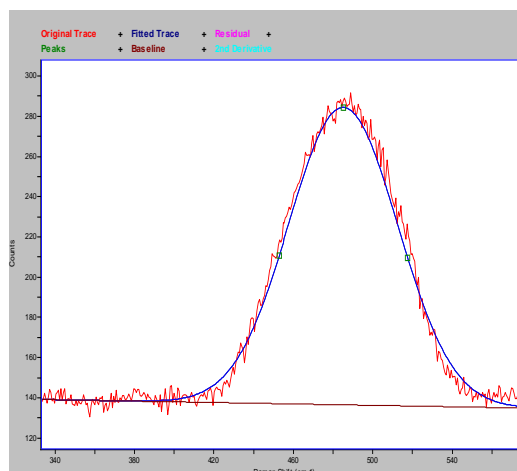
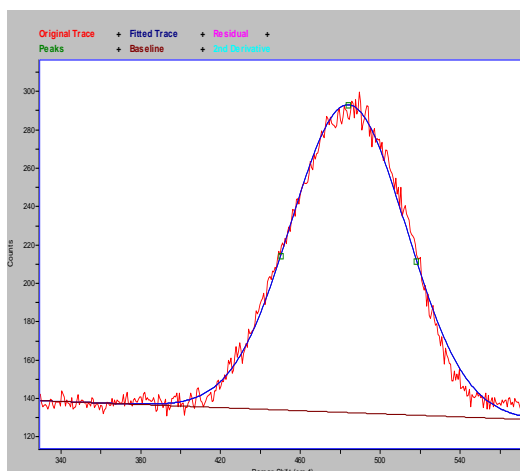
Appendices

Appendix A

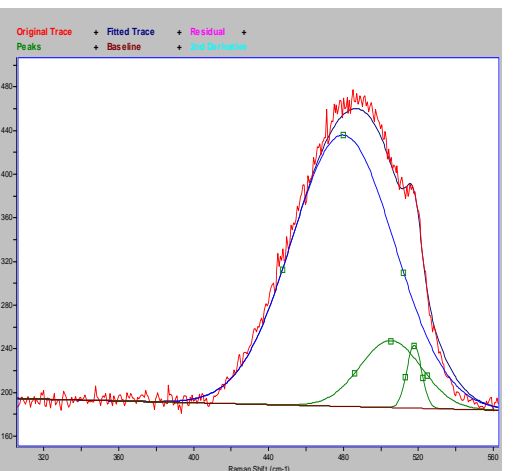
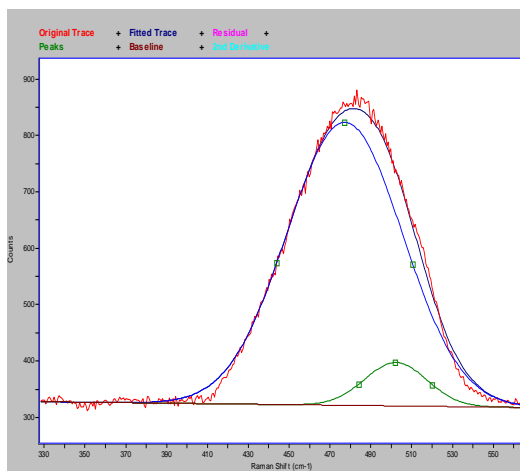
Raman spectrum peak fitting for 21 samples listed in Table. 4.2. In the plots, the x-axis represents the Raman shift (cm^{-1}) and the y-axis represents the Raman intensity (arbitrary units). The peak fitting results including the sample number, peak location, FWHM, integrated area and crystalline volume fraction are listed in the tables below each plot.



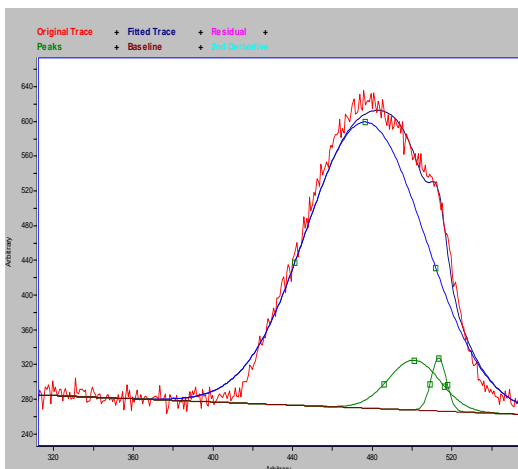
Sample #	Peak (cm^{-1})	FWHM (cm^{-1})	Area	Sample #	Peak (cm^{-1})	FWHM (cm^{-1})	Area
s55	479	69.5	15111.3	s87	478	67.4	18417.6



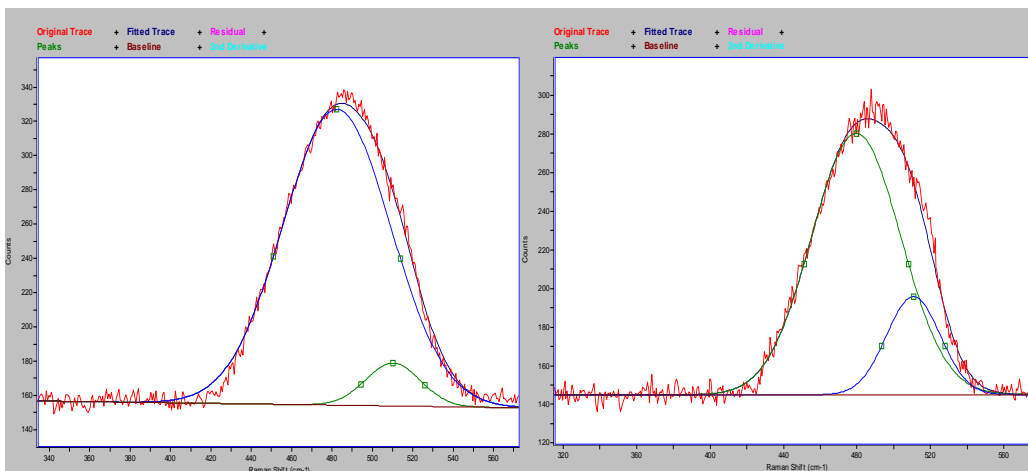
Sample #	Peak (cm ⁻¹)	FWHM (cm ⁻¹)	Area	Sample #	Peak (cm ⁻¹)	FWHM (cm ⁻¹)	Area
s65	484.1	68.1	11602.9	s66	485.2	64.2	10167.9
X_c				X_c			
0%				0%			



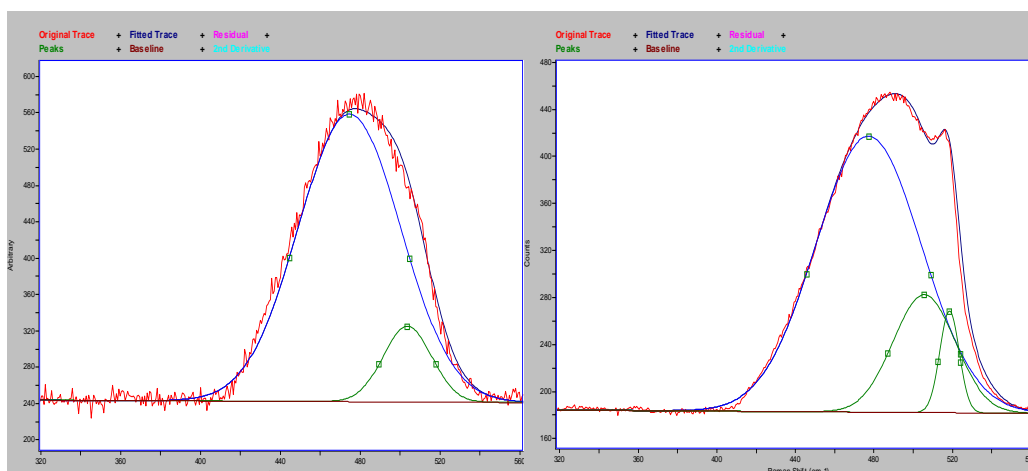
Sample #	Peak (cm ⁻¹)	FWHM (cm ⁻¹)	Area	Sample #	Peak (cm ⁻¹)	FWHM (cm ⁻¹)	Area
s70	477	66.7	35625.8	s69	479	64.5	20451.67
X_c	502	35.9	2934.1	X_c	503	42.7	2257.787
7.6%				12%	518	10.7	593.6731



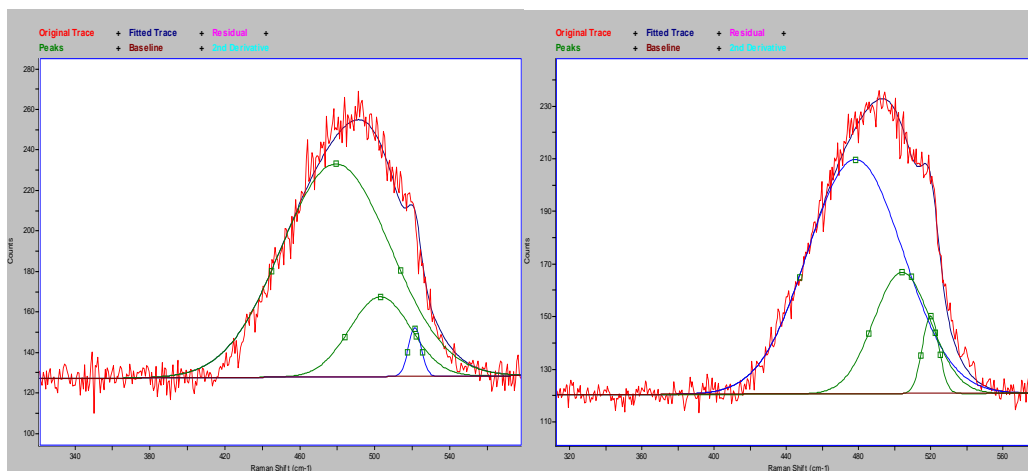
Sample #	Peak (cm ⁻¹)	FWHM (cm ⁻¹)	Area
s86	478	70.7	20115.9
X_c	502	30.3	1859.2
11%	515	8.9	584.3



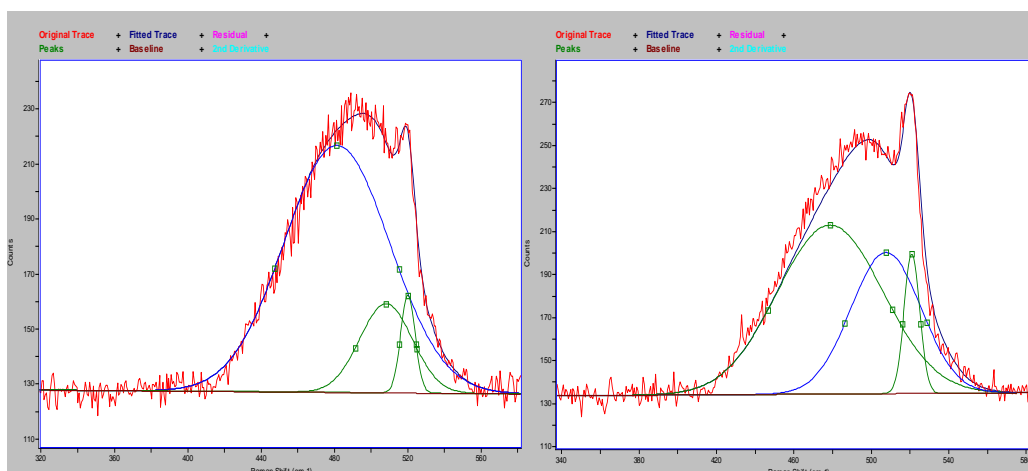
Sample #	Peak (cm ⁻¹)	FWHM (cm ⁻¹)	Area	Sample #	Peak (cm ⁻¹)	FWHM (cm ⁻¹)	Area
s68	482.3	62.7	11539.62	s67	482.3	59.4	12033.7
X_c	510.1	31.7	845.4252	X_c	510.8	30.8	1302.9
6.8%				9%			



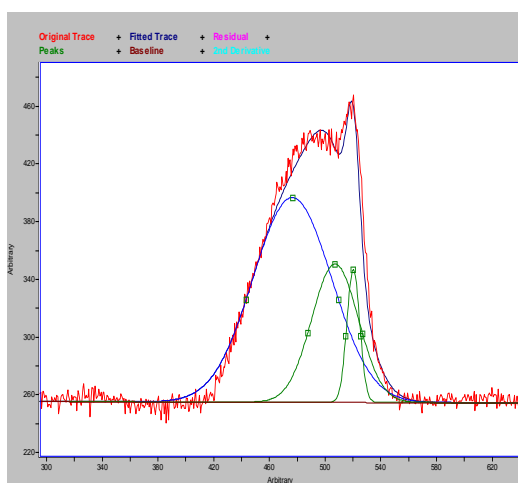
Sample #	Peak (cm ⁻¹)	FWHM (cm ⁻¹)	Area	Sample #	Peak (cm ⁻¹)	FWHM (cm ⁻¹)	Area
s56	479.6	60.1	18262.7	s58	479.2	63.2	15786.1
X _c	509.6	28.4	2513.5	X _c	509.5	36.8	3932.5
12%				24%	518.3	11.5	1063.5



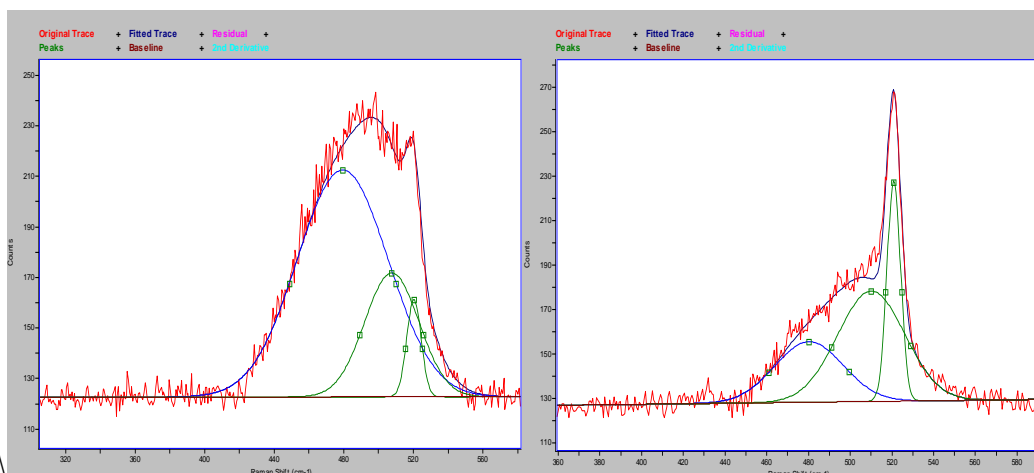
Sample #	Peak (cm ⁻¹)	FWHM (cm ⁻¹)	Area	Sample #	Peak (cm ⁻¹)	FWHM (cm ⁻¹)	Area
s74	480.1	68.4	8658.8	s75	479.1	62.1	7894.6
X _c	505.1	36.3	1476.9	X _c	505.1	36.9	1817.9
16%	519.2	11.1	236.6	21%	519.8	10.8	340.6



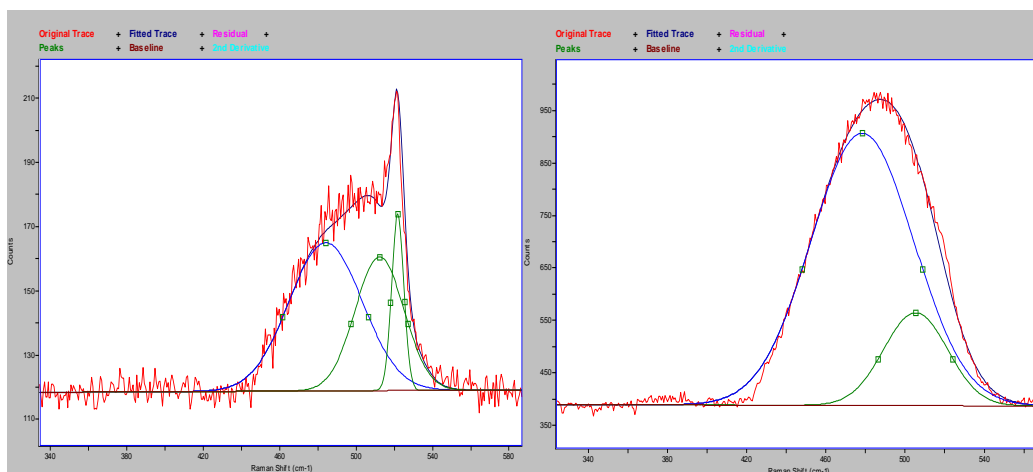
Sample #	Peak (cm ⁻¹)	FWHM (cm ⁻¹)	Area	Sample #	Peak (cm ⁻¹)	FWHM (cm ⁻¹)	Area
s73	481.4	67.8	6474.4	s76	480	64.3	6247.8
X _c	508.2	33.7	2161.5	X _c	507	42.6	3125.2
28%	520.1	9.1	349.1	38%	520	9.4	689.6



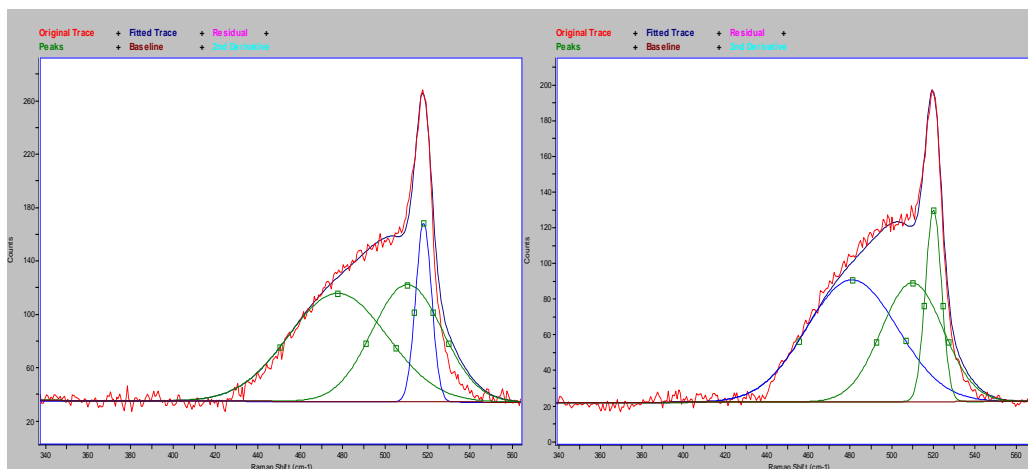
Sample #	Peak (cm ⁻¹)	FWHM (cm ⁻¹)	Area
s97	479	66.4	10048.4
X _c	507	39.2	4010.2
35%	520	10.8	1060.6



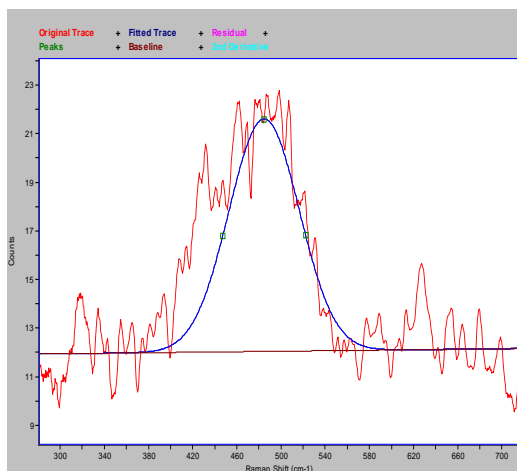
Sample #	Peak (cm ⁻¹)	FWHM (cm ⁻¹)	Area	Sample #	Peak (cm ⁻¹)	FWHM (cm ⁻¹)	Area
s73_2	479.4	61.5	5886.2	s74_2	480	38.5	1112.788
X _c	507.6	36.7	1923.1	X _c	510	37.9	2002.777
28%	520.3	9.7	399.6	72%	520	7.7	809.7356



Sample #	Peak (cm ⁻¹)	FWHM (cm ⁻¹)	Area	Sample #	Peak (cm ⁻¹)	FWHM (cm ⁻¹)	Area
s75_2	484.1	44.9	2205.9	s76_2	479.4	60.9	33627.5
X _c	512.2	29.9	1329.9	X _c	505.2	37.7	7094.5
45%	521.7	7.4	438.9	17%			



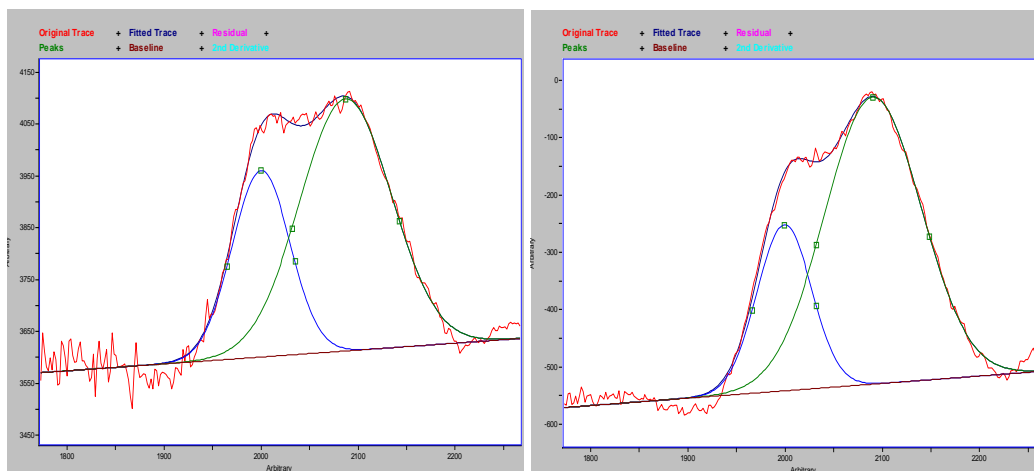
Sample #	Peak (cm ⁻¹)	FWHM (cm ⁻¹)	Area	Sample #	Peak (cm ⁻¹)	FWHM (cm ⁻¹)	Area
s93	479.7	54.9	4728.3	s95	481	51.3	3738.8
X _c	510.4	39.1	3641.5	X _c	510	34.9	2480.3
51%	519.1	8.7	1252.7	49%	520	9.1	1041.3



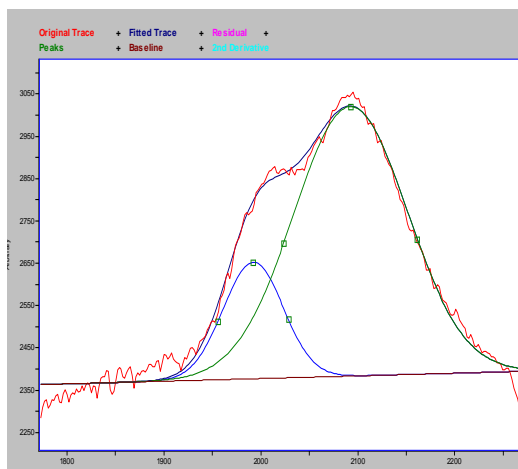
Sample #	Peak (cm ⁻¹)	FWHM (cm ⁻¹)	Area
s96	482	74.8	761.9

Appendix B

Peak fitting of the infrared spectra of the three samples in Figure 5.2. In the plots, the x-axis is the wavenumber (cm^{-1}) and the y-axis is the absorption coefficient (cm^{-1}).



Sample #	Peak (cm^{-1})	Area	$\frac{I_{2090}}{I_{2090} + I_{2000}}$	Sample #	Peak (cm^{-1})	Area	$\frac{I_{2090}}{I_{2090} + I_{2000}}$
s81	1999.9	26916.4	67%	s82_2	1998.5	19932.9	76%
	2087.2	57101.9			2090.1	64382.8	



Sample #	Peak (cm ⁻¹)	Area	$\frac{I_{2090}}{I_{2090} + I_{2000}}$
s82	1992.1	21409.9	81%
	2092.5	93379.0	

Appendix C

1. Table of the experimental conditions

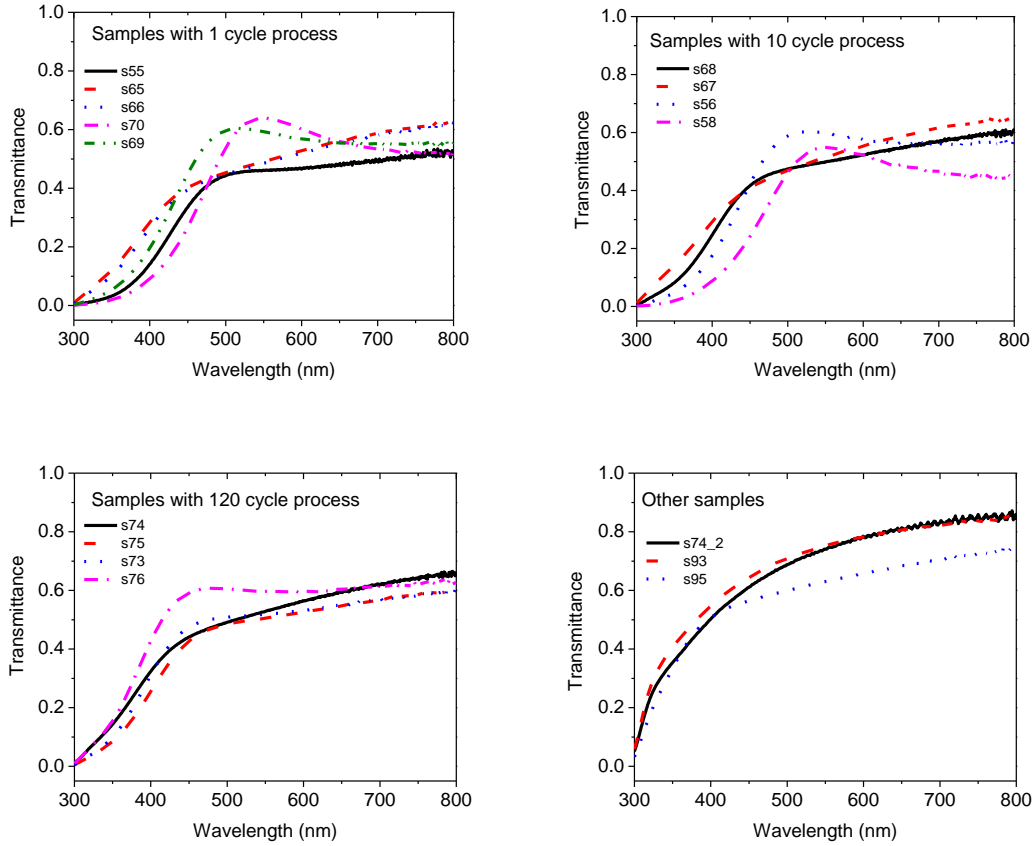
Sample	T	P	CCP SiH4	CCP He	CCP H2	CCP Pwr	CCP Time	ICP H2	ICP Pwr	ICP Time	# Cycles	ICP/CCP Time	Total Dep time	Total Etch Time
1 95	250	710	1	99	40	27	0.08333	80	170	0.08333	480	1	40	40
2 95	250	710	1	99	40	27	0.08333	80	170	0.08333	480	1	40	40
3 93	250	710	1	99	40	27	24.4	80	170	24.4	4500	1	24.4	24.4
4 93	250	710	1	99	40	27	24.4	80	170	24.4	4500	1	24.4	24.4
5 55	250	720	1	99	40	27	40	80	0	0	0	0	40	0
6 65	250	710	1	99	40	27	40	80	170	10	1	0.25	40	10
7 65	250	710	1	99	40	27	40	80	170	10	1	0.25	40	10
8 68	250	730	1	99	40	27	40	80	170	10	10	0.25	40	10
9 74	250	713	1	99	40	27	40	80	170	10	120	0.25	40	10
10 74	250	713	1	99	40	27	40	80	170	10	120	0.25	40	10
11 74-2	250	713	1	99	40	27	10	80	170	40	120	4	10	40
12 66	250	712	1	99	40	27	40	80	170	20	1	0.5	40	20
13 67	250	720	1	99	40	27	40	80	170	20	10	0.5	40	20
14 67	250	720	1	99	40	27	40	80	170	20	10	0.5	40	20
15 75	250	700	1	99	40	27	40	80	170	20	120	0.5	40	20
16 75	250	700	1	99	40	27	40	80	170	20	120	0.5	40	20
17 70	250	727	1	99	40	27	40	80	170	30	1	0.75	40	40
18 70	250	727	1	99	40	27	40	80	170	30	1	0.75	40	40
19 56	250	716	1	99	40	27	40	80	170	30	10	0.75	40	40
20 73	250	710	1	99	40	27	40	80	170	30	120	0.75	40	40
21 73	250	710	1	99	40	27	40	80	170	30	120	0.75	40	40
22 69	250	712	1	99	40	27	40	80	170	60	1	1.5	40	60
23 58	250	725	1	99	40	27	40	80	170	60	10	1.5	40	60
24 76	250	716	1	99	40	27	40	80	170	60	120	1.5	40	60
25 76	250	716	1	99	40	27	40	80	170	60	120	1.5	40	60

2. Table of the parameters in SE analysis for the samples

Sample	SE Run	AOI	MSE	Surface Thk	Thickness	%-void	%_c-Si	Amp	En	Br	Eg	Ep
1 95	7-1-12	55	1.626	20.31	560.36	55.2	1.2418	316.19	4.6148	4.652	1.835	3.9617
2 95	7-17-12	55	2.386	20.12	549.89	55.252	1.1537	319.84	4.615	4.6676	1.8033	4.0764
3 93	6-19-12	55	6.907	36.31	541.07	57.15	0	119.47	6.0014	4.6494	2.373	0.54
4 93	6-19-12	55	4.919	32	360.09	56	0.565	126.22	6.0527	4.0353	2.3435	1.4728
5 55	1-27-12	55	3.027	36.93	561.75	39.248	-1.6447	547.4	3.4754	2.5674	1.4974	6.1622
6 65	1-27-12	55	2.154	100.61	474.21	44.358	-1.0513	980.6	3.5749	2.3473	1.5871	8.9863
7 65	5-22-12	55	2.7	103.22	472.64	43.953	-1.1833	1041.5	3.5727	2.315	1.5624	9.4599
8 68	1-27-12	55	3.71	41.76	573.42	45.114	0.53002	450.29	3.5134	3.5604	1.9486	4.0735
9 74	1-27-12	55	1.996	29.7	542.71	47.599	0.686	573.62	3.7414	3.1696	1.8239	5.7125
10 74	5-22-12	55	5.389	32.6	548.54	48.088	2.9304	467.39	3.9277	3.1474	1.6065	5.78
11 74-2	6-20-12	55	5.98	0	286.32	45.669	3.4405	241.56	4.5858	3.3601	1.8716	4.7049
12 66	1-27-12	55	2.554	105.91	482.25	43.008	-1.4704	907.26	3.568	2.4067	1.6535	8.3689
13 67	1-27-12	55	7.419	52.96	569.14	51.028	-0.96885	167.01	5.2565	6.1687	2.1409	1.3619
14 67	5-22-12	55	9.59	57.14	566.17	50.996	-0.99155	157.63	5.3505	5.9063	2.1455	1.2866
15 75	1-27-12	55	11.26	0	560.35	43.343	3.9031	144.64	3.9657	2.8651	1.3266	2.6523
16 75	5-22-12	55	15.07	0	561.67	44.456	4.5758	133.88	3.9991	2.7002	1.0838	2.7927
17 70	1-27-12	55	15.26	95.09	746.03	41.024	-1.0513	181.55	4.9409	7.1441	2.0448	1.1604
18 70	5-22-12	55	16.84	91.67	735.09	41.966	-1.0612	187.61	4.4338	6.5414	2.0422	1.3039
19 56	1-27-12	55	2.062	27.96	728.47	46.061	0.88587	584.07	3.6039	2.7691	1.6912	5.8322
20 73	1-27-12	55	2.436	33.83	612.52	45.907	1.304	441.29	3.8586	3.1615	1.743	5.0371
21 73	5-22-12	55	2.664	41.4	609.84	46.245	1.3641	452.06	3.8829	3.2629	1.7797	5.0469
22 69	1-27-12	55	20.1	209.3	645.37	43.714	0	160.46	7.2011	10.183	2.2533	0.59009
23 58	1-27-12	55	9.599	57.03	822.13	44.907	-0.94061	237.97	4.6054	6.5051	2.123	1.8337
24 76	1-27-12	55	8.672	50.23	720.9	52.268	2.6971	160.95	5.7161	4.655	2.1899	1.4155
25 76	1-31-12	55	8.277	52.266	721.12	52.266	2.5885	148.44	5.6746	4.0204	2.1784	1.3054

Appendix D

1. Transmission spectrum of all the samples.



2. Optical constants of all the samples

